PROCEEDINGS OF THE KECK GEOLOGY CONSORTIUM

Volume 33
2020
2019-2020 Projects

Dr. Cameron Davidson and Dr. Karl Wirth, Editors
Co-Directors, Keck Geology Consortium

Marga Miller
Keck Geology Consortium Administrative Assistant
Macalester College

Keck Geology Consortium
Macalester College
1600 Grand Ave, St. Paul, MN 55105
(651) 696-6108, Info@KeckGeology.org

ISSN# 1528-7491
doi: 10.18277/AKRSG.2020.33

Funding Provided by:
Keck Geology Consortium Member Institutions
The National Science Foundation Grant NSF-REU 1659322

PROCEEDINGS OF THE KECK GEOLOGY CONSORTIUM

2019-2020 Projects

Cameron Davidson Editor and Co-Director Carleton College	Keck Geology Consortium Macalester College 1600 Grand Ave. St Paul, MN 55105	Karl Wirth Editor and Co-Director Macalester College

Keck Geology Consortium Member Institutions:

Amherst College, Beloit College, Carleton College, Colgate University, The College of Wooster, The Colorado College, Franklin & Marshall College, Macalester College, Oberlin College, Pomona College, Smith College, Trinity University, Union College, Washington & Lee University, Wesleyan University, Whitman College

---

2019-2020 GATEWAY PROJECTS

RESILIENCE AND DECLINE: ARE WE AT A TIPPING POINT FOR ENDANGERED *ACROPORA* SP. CORALS IN BELIZE?
Faculty: LISA GREER, Washington and Lee University and KARL WIRTH, Macalester College
Students: NICK AN, Oxford College of Emory; CATHERINE CATERHAM, Franklin and Marshall College; MATTEA HORNE, Pomona College; ARTHUR MABAKA, Washington and Lee University ; WILLIAM RILEY, Vassar College; JOLIE VILLEGAS, Wesleyan University; SYDNEY WALTERS, Colgate University; RILEY WATERS, Macalester College; PETRA ZUNIGA, Amherst College

EXPLORING LATE CRETACEOUS WETLAND ECOSYSTEMS: DINOSAURS AND VERTEBRATE MICROFOSSILS IN MONTANA
Faculty: RAYMOND ROGERS and KRISTI CURRY ROGERS, Macalester College
Students: NOLAN CLARK, Pomona College; SEDALIA GOMEZ, Amherst College; KATHERINE IRVING, Macalester College; ASHA LANG, Smith College; GABRIELA ROAT, Colorado College; SUN TUN, Macalester College; KAYLEE VELASQUEZ, Union College; PETER ZIMMERMANN, Oberlin College

---

2019-2020 ADVANCED PROJECTS

BODY SIZE EVOLUTION OF THE FIRST MAMMALIAN MEGAHERBIVORE DURING PALEOGENE HYPERTHERMAL EVENTS, WYOMING
Faculty: MICHAEL D'EMIC, Adelphi University and SIMONE HOFFMANN, New York Institute of Technology
Students: GRANT BOWERS, University of Maryland; MICHAEL FORD, Missouri University of Science and Technology; RICHARD GONZALEZ, University of Texas at San Antonio; DANIKA MAYBACK, Illinois State University; EMILY RANDALL, The College of Wooster; ISAAC SAGEMAN, Northwestern University

USING 3D PETROGRAPHY OF MICROLITES AND BUBBLES IN OBSIDIAN TO ASSESS FACTORS GOVERNING ERUPTIVE STYLE FOR RHYOLITIC MAGMAS
Faculty: KURT KNESEL, Trinity University
Students: CHLOE CAMPO, Trinity University; BROOKE DYKSTRA, University of Illinois at Urbana-Champaign; JULIANA FLINT, SUNY Plattsburgh; ZENJA SEITZINGER, SUNY Geneseo

2019-2020 ADVANCED PROJECTS – Continued

UNRAVELING THE CONTROLS ON CHANNEL FORM AND GEOMORPHIC HISTORY IN NORTHERN YELLOWSTONE NATIONAL PARK, WYOMING
Faculty: LYMAN PERSICO, Whitman College
Students: MARK FOKY, Whitman College; ALICE HINZMANN, Carleton College; CHANTAL IOSSO, Washington and Lee University; APRIL PHINNEY, Wheaton College (IL); ELIZA VAN WETTER, Whitman College

Short Contributions and Poster Presentations – Belize Gateway Project

Short Contributions and Poster Presentations – Montana Gateway Project

Short Contributions – Wyoming Advanced Project

Short Contributions – Rhyolitic Magmas Advanced Project

Short Contributions – Yellowstone Advanced Project

KECK Geology Consortium
Learning Science Through Research
Published by the Keck Geology Consortium

Short Contributions
Keck Geology Consortium
Volume 33
May 2020
doi: 10.18277/AKRSG.2020.33.01

RESILIANCE AND DECLINE: ARE WE AT A TIPPING POINT FOR ENDANGERED ACROPORA SP. CORALS IN BELIZE?

LISA GREER, Washington and Lee University
KARL WIRTH, Macalester College
GINNY JOHNSON, Washington and Lee University, Peer Mentor

INTRODUCTION

Coral Gardens, Belize has been a home for thriving *Acropora* spp coral communities even at a time of Caribbean-wide collapse of these threatened species. Up to 98% of acroporids are thought to have perished in the wider Caribbean-Atlantic since the 1980's or before due to synergistic factors including warming temperatures, White Band Disease, collapse of herbivore species, overfishing, and eutrophication (Gladfelter, 1982; Lessios, 1988; Aronson and Precht, 2001; Pandolfi and Jackson, 2006; Randall and Van Woesik, 2015; Cramer et al., in press). While *Acropora palmata* and *Acropora cervicornis* have been declining, there is some evidence that their F1 hybrid *Acropora prolifera* may be increasing in their stead, giving rise to hopes that this species may help provide a similar habitat for the reef ecosystem (Vollmer and Palumbi, 2002; Fogarty et al, 2012; Nylander-Asplin et al., in review).

Since 2011, live *A. cervicornis* coral tissue has been monitored annually along 5 established transects at Coral Gardens using m^2 scaled quadrat photographs. In 2014-2015, a team of eleven students and three faculty members completed an Advanced Keck project at Coral Gardens that included assessments of additional environmental and conditional parameters at Coral Gardens (Greer et al, 2015), including coral genetics, geochemical records of environmental change, herbivore dynamics, and ages of fossil coral material. This set the stage for the current project, providing a robust comparative dataset.

The current project also expanded the scope of study at Coral Gardens by including three-dimensional modeling of coral morphology using photogrammetry techniques and opportunistic assessment of massive *Sargassum* spp. seaweed blooms landing on Ambergris Caye beaches.

Although live coral cover has been declining at Coral Gardens since the 2014-2015 Keck project, the site still remains one of the better sites for extant *Acropora* spp. in the Caribbean. One aim of this project was to assess how resilient *A. cervicornis* has remained in the face of massive Caribbean-wide decline and to explore the connections between living coral, algae, and herbivore dynamics at this site. The project took place inshore of the MesoAmerican Barrier reef off Ambergris Caye in June and July 2019 (Figure 1).

METHODS

This study utilized multiple methods to investigate three separate projects off Ambergris Caye, Belize. We used high resolution photo-documentation and field measurements at Coral Gardens to examine relationships between live coral cover and herbivore abundance. We collected pH, Dissolved Oxygen, and temperature data to investigate the impacts of incoming Sargassum blooms on the near shore environments off Ambergris Caye. We also collected detailed overlapping photographic data from individual *Acropora cervicornis*, *Acropora palmata*, and *Acropora prolifera* colonies to create three-dimensional models of each species to assess the degree to which *A. prolifera* morphology provides a similar habitat to that of its parent species. We used multiple computer software programs in each facet of this work.

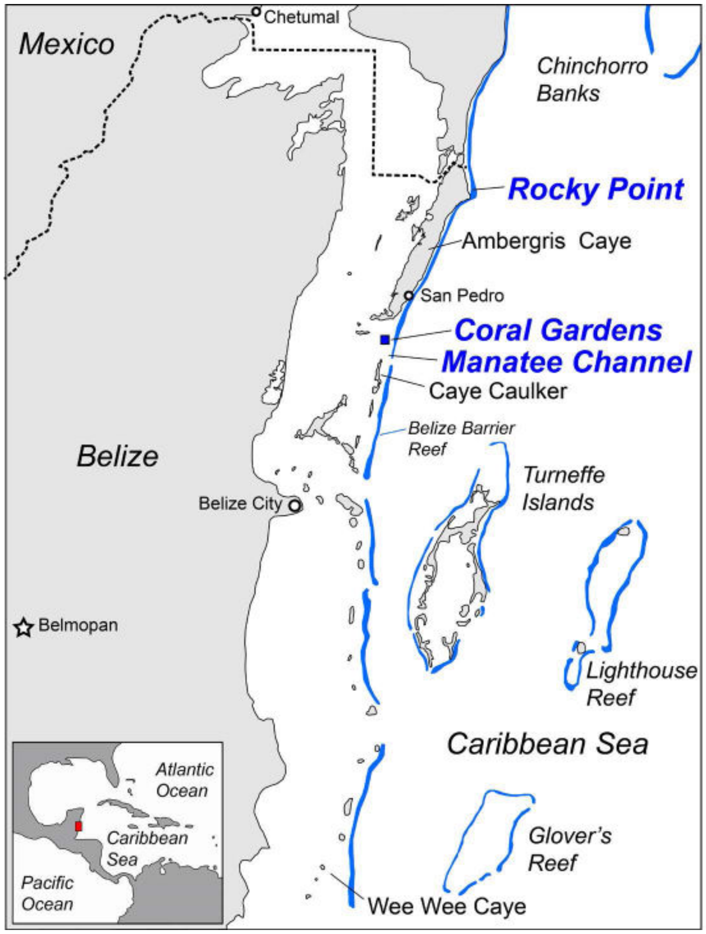

Figure 1. Location map of field sites in Belize.

RESEARCH

This research involved nine rising sophomore students, a rising senior peer mentor, and two faculty from ten different institutions. Together, we quantified 2-dimensional live coral cover from 141 individual quadrat photos. Unfortunately, our work documented a decrease in live A. cervicornis coral cover per m^2 at all 5 transect locations from 2013 to 2019 (Figure 3). While T5 still has the highest percentage of live coral, it showed the greatest decrease in percent over the study period. The remainder of our work was divided into three different areas of inquiry, described below.

The response of algae and herbivores to *Acropora cervicornis* decline

Catherine Rachel Caterham (Franklin and Marshall College), **Nick An** (Oxford College of Emory University), **Sydney Walters** (Colgate University), **Arthur Mabaka** (Washington and Lee University), **Ginny Johnson** (Washington and Lee University)

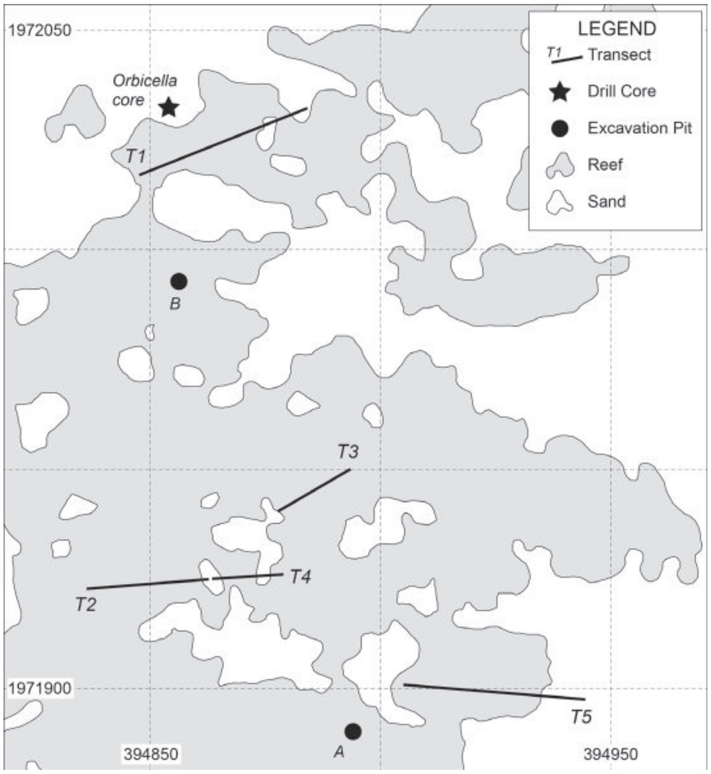

Figure 2. Map of Coral Gardens showing all 5 semi-permanent transect locations (T1-T5).

A decline in live *A. cervicornis* coral cover has been documented at Coral Gardens over the past few years and in particular since the 2014-2015 Keck Advanced project took place. Elsewhere in the Caribbean, *A. cervicornis* has been replaced by macroalgae that has often outcompeted new coral recruits for space on the reef. At some Caribbean locations, it is the suite of coral species that has changed, from the fast-growing and branching acroporids to 'weedier' species like *Agaricia* and *Porites* spp. It has been

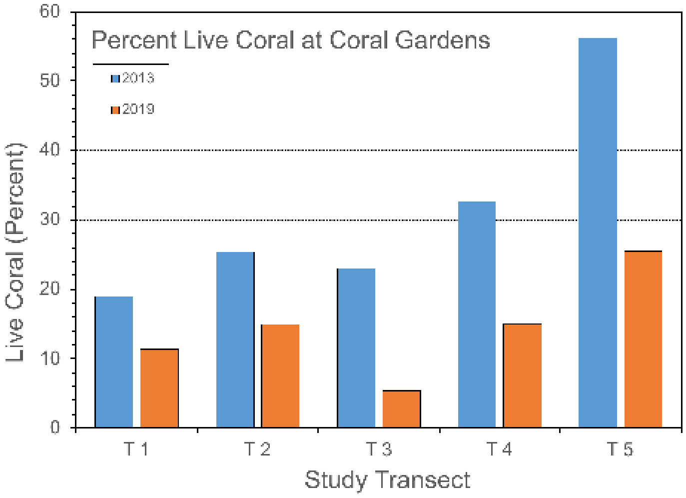

Figure 3. Comparison of mean live coral cover per m2 at transects 1-5 from 2013 to 2019.

well documented that algal cover is often tightly tied to herbivore abundance. This team explored whether the declining coral cover has been accompanied by an increase in macroalgae on the reef, a phase shift in dominant coral species, and/or a change in the abundance of key herbivores at Coral Gardens (Caterham et al., 2019). The team documented the abundance of *Echinometra viridis* urchins, and Damselfish (*Stegastes adustus, Stegastes planifrons, and Microspathodon chrysurus*) within m^2 quadrats across all 5 transects and designated *A. prolifera* patches. They also quantified coral species, live coral, non-living reef framework, sediment, and algae every 0.5 m along each transect with a point-count method. Between 2014 and 2019, they measured a 10.6% absolute increase in non-living framework and a 5.8% increase in algae, noting that the increase in algae was less than non-living rubble surfaces. This could be due in part to the average increase in urchins from 17.4 per m^2 in 2014 to 21.4 per m^2 in 2019. In that time *Agaricia agaricites* increased by 6.3% and damselfish abundance increased by 15%. from 2.0 to 2.3 per m^2. This suggests that damselfish may have some impact on the growth of algae in a declining coral scenario and emphasizes the complexity and importance of ecosystem interactions on coral, algae, and herbivores on the reef.

Browning of the Golden Tide: Impacts of accumulated Sargassum on sea water quality in Ambergris Caye, Belize

Petra Zuñiga (Amherst College), **Will Riley** (Vassar College), **Riley Waters** (Macalester College), **Ginny Johnson** (Washington and Lee University)

We arrived in Belize amidst a massive influx of pelagic *Sargassum* spp., a phenomenon that has only recently occurred in the equatorial Atlantic. Since about 2011, this seaweed has accumulated along Caribbean shorelines, converting from a free-floating 'Golden Tide' offshore to plumes of brown water emanating from the shoreline as the Sargassum rots and decomposes. In addition to aesthetic concerns (sight and smell) for local businesses and residents, the brown water has a measurable impact on water quality nearshore. This team assessed the extent and properties of the browning water offshore of the eastern shore of Ambergris Caye (Zuñiga et al., 2019). They measured dissolved oxygen (DO), pH, temperature, specific conductivity, water color and clarity at 21 locations and along 4 transects perpendicular to the shoreline. They found DO as low as 0.03 mg/L inshore, a 99.5% decrease in DO compared to typical seawater, while DO in free-floating 'Golden' patches averaged 6.0 mg/L. The pH beneath free-floating Sargassum averaged 8.07 but was as low as 6.44 nearshore. Both DO and pH generally increased with distance from shore. The largest brown patch we measured was greater than 265,000 m^2 and extended 200 m from shore, about a quarter of the distance to the reef crest. At another location the brown water extended greater than 800 m from shore. Interviews with local residents suggest these plumes were small in comparison to peak values in recent years. Fish kills, seagrass die-offs near shore, and negative health impacts for humans were all reported by local residents associated with these events. The team noted the importance of continued monitoring and further studies focused on potential remediation efforts for the personal, health, and economic benefits of Belizeans.

Living spaces: Quantifying morphological differences in *Acropora* spp. Corals using 3D Photogrammetry

Mattea Horne (Pomona College), **Jolie Villegas** (Wesleyan University), **Sydney Walters** (Colgate University), **Ginny Johnson** (Washington and Lee University), and in collaboration with **David Pfaff** (Washington and Lee University)

This team investigated the degree to which the morphology of the hybrid *A. prolifera* might produce a similar habitat for herbivores as the parent species *A. palmata* and *A. cervicornis* (Horne et al., 2019). They collected detailed overlapping photographs of coral colonies underwater with a variety of photographic parameters to test which techniques might best facilitate high resolution 3D modeling. They also measured the abundance of *Echinometra viridis* urchins in m^2 quadrats on *A. cervicornis* and *A. prolifera* colonies. They used Agisoft Metashape Professional photogrammetry software to stitch the photos together and measure coral branch height and width. They then used Cinema 4D software to measure the total surface area of live and dead coral substrate, volume of coral skeleton, and available pore space between branches in each model. They found that *A. prolifera* had 43-49% greater total surface area than *A. cervicornis* with 3.3-3.4 m^2 per square meter (live *A. prolifera*) based on the footprint of the coral colonies. *A. prolifera* had 9-13% higher surface area than *A. palmata*. The available space (accessible habitat) for urchins was measured by subtracting the volume of coral from the volume of the smallest possible polygon constructed to contain the coral colony. *A. cervicornis* had the greatest available space (0.96 m^2 per cubic meter) followed by *A. prolifera* (0.91-0.95 m^2 per cubic meter) and *A. palmata* (0.89 m^2 per cubic meter). Yet total volume does not capture the size distribution of spaces, which is key to determining utility for an urchin. *A. prolifera* exhibits a scrubbier 'bushy' and more compact morphology that is generally distinct from the more open lattice of *A. cervicornis* and the very open canopy of *A. palmata*. Therefore, the available space in an *A. prolifera* colony is distributed more widely but manifest in smaller spaces. Field data showed denser urchin populations in *A. prolifera* patches (31.7 urchins per m^2) than *A. cervicornis* (21.4 urchins per m^2) but the urchins associated with *A. prolifera* appeared smaller on average. The results suggest that the distinct morphologies of these coral species might provide some influence on the size, movement, and available shelter of those that seek food and/or refuge within reef framework.

IMPLICATIONS OF THIS WORK

Is Coral Gardens a refugia?

Although live *Acropora cervicornis* has declined over the last several years at Coral Gardens, it remains one of the largest documented accumulations of extant *A. cervicornis* reported in the literature (Busch et al., 2016). For how long this will continue cannot be resolved at this time. Genetic aging of Coral Gardens acroporids suggests a long-lived and persistent population (Irwin et al., 2017) and age data from the 2014-2015 Keck project confirms persistence over the last 100 years (Greer et al., in prep). This study shows continued growth of *Acropora* spp. at Coral Gardens. At the same time, it seems that declining coral has not resulted in the kind of massive phase shift from coral to algae that other sites in the Caribbean have seen. It is possible that Coral Gardens herbivores are key to keeping the algae at bay.

Are the recent Sargassum blooms detrimental to nearshore Ambergris Caye?

Our data suggest that the browning of the golden tide is potentially a very dangerous phenomenon for humans and nearshore marine communities. While a great deal more work should be done, and our evidence for negative health impacts is anecdotal, it is clear that the decomposing *Sargassum* spp leads to DO far below sustainable levels for marine communities in the shallowest nearshore environments. The decrease in pH levels nearshore is worrisome for carbonate producers (coral and calcareous algae) in those areas closest to shore. Mitigation, while keeping the health of humans interacting with the decaying Sargassum spp. in mind, should be an important consideration moving forward.

Will *Acropora prolifera* provide a similar habitat to its parent species for other reef dwellers?

While *A. prolifera* does seem to provide a framework somewhat similar to *A. cervicornis*, it is not a perfect substitute. It seems to provide more space but for smaller *Echinometra viridis* urchins. More work needs to be done to better assess the degree to which *A. prolifera* provides space and habitat to other reef dwellers.

Should Coral Gardens be protected?

Our data suggest that Coral Gardens remains an exceptional location for extant *Acropora* spp. corals. We continue to suggest that Coral Gardens may benefit from increased conservation efforts and we hope that Marine Protected Area (MPA) designation will be considered for this site. We understand that MPA status does not always result in better coral health against a formidable backdrop of global and regional climate and environmental change. But our data show that Coral Gardens remains a refuge, at least for now, for *Acropora* spp. corals.

ACKNOWLEDGEMENTS

This material is based upon work supported by the Keck Geology Consortium and the National Science Foundation under Grant No. 1659322. Additional funding for this project was generously provided by the Washington and Lee Office of the Provost and Geology Department. In addition to home advisors, we wish to thank Sarah Wilson and Emily Falls (W&L Geology) and David Pfaff (W&L IQ Center.) We gratefully acknowledge Ken Mattes, Maureen Gannon, and Maggie at the TREC Marine Lab for their support of this project. We thank Al Curran (Smith College) for providing the inspiration, collaboration, guidance, and vast expertise that formed the basis of this project. We are very grateful for the continued support of the Belize Fisheries Department and Hol Chan Marine Reserve for this work, and in particular, Kirah Forman.

REFERENCES

Aronson, R.B. and Precht, W.F. (2001), White-band disease and the changing face of Caribbean coral reefs. Hydrobiologia, 460:25-38.

Busch, J., Greer, L., Harbor, D., Wirth, K., Lescinsky, H., and Curran, H.A. (2016) Quantifying exceptionally large populations of *Acropora* spp. corals in Belize using sub-meter satellite imagery classification. Bulletin of Marine Science, v.92, pp. 265-283. http://dx.doi.org/10.5343/bms.2015.1038

Caterham, C.R., An, N., Walters, S., Mabaka, A., Johnson, G., Wirth, K.R., Greer, L., 2019, The Response of Algae and Herbivores to *Acropora cervicornis* Coral Decline: A Case Study in Coral Gardens, Belize: American Geophysical Union Fall Meeting, Abstracts with Programs, San Francisco, CA, 9-13 December 2019.

Cramer KL, Jackson JBC, Donovan MK, Greenstein BJ, Korpanty CA, Cook GM, Pandolfi JM. Widespread loss of Caribbean acroporid corals was underway before coral bleaching and disease outbreaks. (in press) Science Advances.

Fogarty, N.D., Vollmer, S.V., & Levitan, D.R. (2012) Weak prezygotic isolating mechanisms in threatened Caribbean *Acropora* corals. PlosOne,7(2), e30486.

Gladfelter, W. B., (1982) White-band disease in *Acropora palmata* – Implications for the structure and growth of shallow reefs: Bulletin of Marine Science, v. 32, no. 2, p. 639-643

Greer, L., Lescinsky, H., and Wirth, K., 2015, Multi-level characterization of acroporid coral populations at Coral Gardens, Belize: A refugia identified. Proceedings of the 28th Annual Keck Research Symposium. Schenectady, New York, USA. http://www.keckgeology.org/publications, 6 p.

Greer, L., Waggoner, T., Clark, T., Guilderson, T., Busch, J., Curran, H.A., Zhao, J.X., Wirth, K, (in prep) Coral Gardens Reef, Belize: A refuge from Caribbean *Acropora* spp. decline. To be submitted to Plos One.

Greer, L., Lescinsky, H., and Wirth, K., 2015, Multi-level characterization of acroporid coral populations at Coral Gardens, Belize: A refugia identified. Proceedings of the 28th Annual Keck Research Symposium. Schenectady, New York, USA. http://www.keckgeology.org/publications, 6 p.

Horne, M., Villegas, J., Walters, S., Pfaff, D., Johnson, G., Wirth, K.R., Greer, L., 2019, Living Spaces: Quantifying Morphological Differences in *Acropora* spp. Corals Using 3D Photogrammetry: American Geophysical Union Fall Meeting, Abstracts with Programs, San Francisco, CA, 9-13 December 2019.

Irwin, A., Greer, L., Humston, R., Devlin-Durante, M., Cabe, P., Lescinsky, H., Wirth, K., Curran, H.A., and Baums, I. (2017), Age and intraspecific diversity of resilient *Acropora* communities in Belize. Coral Reefs, 36(4), 1111-1120, doi:10.1007/s00338-017-1602-9.

Lessios H.A. Mass mortality of Diadema antillarum in the Caribbean: what have we learned? (1988) Ann. Rev. Ecol. Syst. 19:371–93.

Nylander- Asplin, H.F., Hill, R.L., Doerr, J.C., Greer, L., and Fogarty, N.D., (in review), Population dynamics and genotypic richness of the threatened *Acropora* spp. and their hybrid in the U.S. Virgin Islands. Submitted to Coral Reefs in March 2020.

Pandolfi J.M., Jackson J.B.C. (2006) Ecological persistence interrupted in Caribbean coral reefs. Ecology Letters. 7:818-826. doi:10.1111/j.1461-0248.2006.00933.x.

Randal C.J., van Woesik R. (2015) Contemporary white-band disease in Caribbean corals driven by climate change. Nature Climate Change 5:375-379.

Vollmer, S.V., Palumbi, S.R. (2002). Hybridization and the evolution of reef coral diversity. Science, 296 (5575), 2023-2025.

Zuñiga, P., Riley, W., Waters, R., Johnson, G., Greer, L., and Wirth, K.R., 2019, Browning of the Golden Tide: Impacts of Accumulated Sargassum on Sea Water Quality in Ambergris Caye, Belize: American Geophysical Union Fall Meeting, Abstracts with Programs, San Francisco, CA, 9-13 December 2019.

KECK Geology Consortium
Learning Science Through Research
Published by the Keck Geology Consortium
Short Contributions
Keck Geology Consortium
Volume 33
May 2020
doi: 10.18277/AKRSG.2020.33.06

BODY SIZE EVOLUTION OF THE LARGE PANTODONT MAMMAL *CORYPHODON* DURING PALEOGENE HYPERTHERMAL EVENTS

MICHAEL D. D'EMIC, Adelphi University
SIMONE HOFFMANN, New York Institute of Technology
BRADY Z. FOREMAN, Western Washington University

INTRODUCTION

Climate change affects the resources available to animals, impacting factors such as their geographic ranges, growth rates, and reproductive behaviors. These effects can be measured in in the fossil record and used to predict ecosystem change in the future (Barnosky et al., 2017). One of the best-studied examples of past climate change and its effects is the Paleocene-Eocene Thermal Maximum (PETM) at about 56 Ma, which caused massive perturbations in floras (Wing et al., 2005), fluvial landscapes (Foreman et al., 2012), and mammalian evolution (Gingerich, 2003). The PETM was followed by a long-term warming trend during the early Eocene that culminated with the Early Eocene Climatic Optimum (Zachos et al., 2008). This long-term warming trend was punctuated by 'hyperthermal' events similar to the PETM during the early Eocene (Abels et al., 2015). In response to the PETM and other hyperthermals, rapid and extreme mammalian dwarfing occurred (Gingerich, 2003; Secord et al., 2012, d'Ambrosia et al., 2017). It is unclear how mammals evolved their smaller body size in terms of growth pattern and duration. During our Keck project, our team studied the evolution of body size, growth, and paleoenvironment of the first mammalian megaherbivore, *Coryphodon*.

Coryphodon is known from hundreds of localities in precisely dated paleosols of the Bighorn Basin, and its bones and teeth preserve annual growth rings that allow individual specimens to be aged (Figures 1, 2). Unprecedented for a mammal at the time, *Coryphodon* reached the size of a small rhinoceros during the mid-Paleocene (Uhen and Gingerich, 1995). Shortly after the PETM, it underwent a dwarfing event to half its body mass, only to return to its original size later in the Eocene (Figure 2A; Uhen and Gingerich, 1995; unpublished data). *Coryphodon* is severely understudied—though thousands of specimens exist in museum collections, only a handful of biogeographic, isotopic, and taphonomic studies have been conducted (e.g., Simons, 1960; Fricke et al., 1998; McGee, 2001; McGee and Turnbull, 2010; Dawson, 2010). We have gathered bone and tooth measurements from over 1,000 individuals from museums. Many of these specimens were collected during the "fossil gold rush" of the 1880s-1910s and lack precise provenance data. Therefore, we have begun targeted fieldwork to fill in spatiotemporal gaps in the *Coryphodon* fossil record, which our Keck students assisted us with to great success.

PROJECT GOALS

The overall goal of our Keck project was to understand the evolution of body size, growth, and paleoecology in *Coryphodon* in relation to environmental change. We did this by making thin sections of bones and teeth from museums and newly collected field specimens. Bones and a tooth-anchoring tissue known as cementum record annual bands, akin to tree rings, that allow age and growth rates to be estimated in extinct mammals (Kolb et al., 2015; Figure 2). With the students in our Keck group, we undertook four objectives: (1) collect *Coryphodon* specimens via quarrying and prospecting, (2) place our finds in spatiotemporal, paleoenvironmental, and taphonomic contexts, and (3) assess the age of each *Coryphodon* specimen with incremental growth line counts in

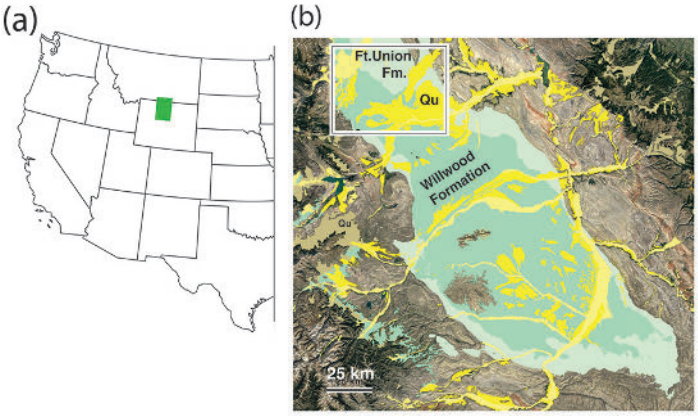

Figure 1. Study area. (a) Map of western United States highlighting area shown in detail in (b), which shows the studied locations within the Bighorn Basin.

bones and tooth cementum. With our students, we began to densely sample *Coryphodon* to assess growth patterns before, during, and after dramatic climate change events (i.e., hyperthermals).

Fieldwork took place in the Fort Union and Willwood formations (Figure 3) of the northern Bighorn Basin, which are composed of a more than 2,000 m thick sequence of fluvial, floodplain, and minor palustrine deposits (Bown and Kraus, 1981). These extensive strata have been the target of over a century of detailed paleontological fieldwork, resulting in the recovery of tens of thousands of vertebrate fossil specimens (Gingerich, 2003). Fossil-hosting ancient soil horizons can be resolved temporally to ca. 100,000-year time intervals (Gingerich, 2003; Secord et al., 2012). *Coryphodon* has been reconstructed with a semiaquatic lifestyle, inferred from anatomy and oxygen isotope data (Simons, 1960; Fricke et al., 1998), yet is found in a variety of facies (Uhen and Gingerich, 1995). By collecting detailed paleoenvironmental and taphonomic data with our Keck students, we are addressing the habitat of *Coryphodon* in more detail, with an integrative approach.

RESEARCH PROJECTS

The five research projects conducted in this study integrated data from stratigraphy, taphonomy, paleohistology, and anatomy with intensive fieldwork aimed at understanding the evolution of body size in *Coryphodon*, the first mammalian megaherbivore, on fine spatial scales. In the field, we prospected for and excavated fossils and created high-resolution stratigraphic columns. In the lab, students were trained in photogrammetry, molding and casting, fossil preparation, and bone and tooth histology.

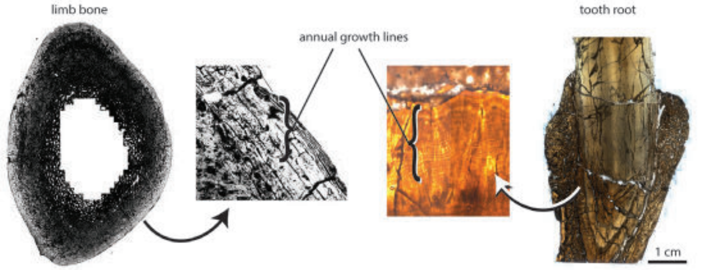

Figure 2. Femur and canine of Coryphodon showing annual growth lines.

Emily Randall (Wooster College) recorded geologic data from several mammalian biozones across the northern Bighorn Basin in order to infer the paleoenvironments in which *Coryphodon* lived. She included data from paleosols and nodules to infer the moisture content of soils, capturing changes to the ecosystems that *Coryphodon* inhabited through the Paleogene.

Grant Bowers (University of Maryland) studied the bone histology of *Coryphodon* in order to determine its growth rates and longevity. Grant analyzed the microstructure of some of the bones the Keck team discovered and thin sectioned, after their morphology had been properly preserved through molding, casting, and photogrammetry. Grant compared his thin sections with those from extant animals to give us a better understanding of *Coryphodon* habitats and life

Figure 3. Keck Coryphodon field team at the site of a newly discovered specimen.

history.

Richard Gonzalez (University of Texas at San Antonio) analyzed scaling among *Coryphodon* bones in order to predict body mass from isolated elements, which are commonly recovered in the fossil record. Richard found that some isolated elements can be used to predict body mass more reliably than it had been predicted in the past, which will allow characterization of its body mass evolution through time.

Danika Mayback (Illinois State University) studied the histology of cementum, the tissue in *Coryphodon* that helps to anchor the teeth to the jaws (also found in our jaws). There has been a recent appreciation for how cementum can be used to estimate age in extinct animals; it has commonly been used as a technique in forensic anthropology and wildlife management. Danika found that some *Coryphodon* individuals lived long lives, upwards of 30 years. Her work forms a baseline for how to assess age and data quality from cementum in *Coryphodon*.

Isaac Sageman (Northwestern University) took nearly 100 samples from over a dozen *Coryphodon* sites in the basin and measured inorganic and organic carbon percentages and bulk carbon isotope values in order to better characterize the depositional environments of *Coryphodon* throughout its evolution and constrain our sampling temporally.

ACKNOWLEDGMENTS

This material is based upon work supported by the Keck Geology Consortium and the National Science Foundation under Grant No. 1659322. We thank all the student participants—Danika, Emily, Richard, Isaac, and Grant—for their hard work on the project, as well as Cameron Davidson, Karl Wirth, and Marga Miller (Macalester College) for their support. We also gratefully acknowledge the support staff at the Yellowstone-Bighorn Research Association. We thank A. Chew (Brown University), P.D. Gingerich, and K. Rose for advice and assistance; C. Anco (Draper Museum of Natural History), I. Lundeen, and B. Rodwell (UT Austin), M. Wood (UM), and T. Churchill for field support. Thanks to A. Rountrey and J.A. Wilson (UM) and M. Fox and D. Brinkman (YPM) for assistance with collections, sampling, and loans.

REFERENCES

Abels, H.A., Clyde, W.C., Gingerich, P.D., Hilgen, F.J., Fricke, H.C., Bowen, G.J., and Lourens, L.J. 2012. Terrestrial carbon isotope excursions and biotic change during Palaeogene hyperthermals. Nature Geoscience 5: 326–329.

Barnosky, A.D., Hadly, E.A., Gonzalez, P., Head, J., Polly, P.D., Lawing, A.M. et al. 2017 Merging paleobiology with conservation biology to guide the future of terrestrial ecosystems. Science 355: eaah4787.

Bown, T.M., and Kraus, M.J. 1981. Lower Eocene alluvial paleosols Willwood Formation, northwest Wyoming, USA and their significance for paleoecology paleoclimatology, and basin analysis. Palaeogeography, Palaeoclimatology, Palaeoecology 34: 1–30.

D'Ambrosia, A.R., Clyde, W.C., Fricke, P.D. Gingerich, and Abels, H.A. 2017. Repetitive mammalian dwarfing during ancient greenhouse warming events. Science Advances 3: e1601430.

Dawson, M.R. 2010. *Coryphodon*, the northernmost Holarctic Paleogene pantodont (Mammalia), and its global wanderings. Swiss Journal of Geoscience 131: 11–22.

Foreman, B.Z., Heller, P.L. and Clementz, M.T. 2012. Fluvial response to abrupt global warming at the Palaeocene/Eocene boundary. Nature 491: 92–95.

Fricke, H.C., Clyde, W.C., O'Neil, J.R., and Gingerich, P.D. 1998. Evidence for rapid climate change in North America during the latest Paleocene thermal maximum: oxygen isotope compositions of biogenic phosphate from the Bighorn Basin (Wyoming). Earth and Planetary Science Letters 160: 193–208

Gingerich, P.D. 2003. Mammalian responses to climate change at the Paleocene-Eocene boundary: Polecat Bench record in the northern Bighorn Basin, Wyoming. In S.L. Wing, P.D. Gingerich, B. Schmitz, and E. Thomas (eds.), Causes and consequences of globally warm climates in the early Paleogene, Geological Society of America, Special Paper 369: 463–478.

Kolb C., Scheyer, T., Veitschegger, K., Forasiepi, A.M., Amson, E., Van der Geer, A.A.E., van den Hoek Ostende, L.W., Hayashi, S., and Sánchez-Villagra, M.R. 2015. Mammalian bone palaeohistology: a survey and new data with emphasis on island forms. PeerJ 3:e1358.

McGee, E.M. 2001. A mass death accumulation of *Coryphodon* anthracoideus (Pantodonta: Mammalia) from Roehler's *Coryphodon* Catastrophe Quarry (Lower Eocene, Wasatch Formation, Washakie Basin, Wyoming), pp. 317–333. In Gunnell, G. G., ed., Eocene Biodiversity: Unusual Occurrences and Rarely Sampled Habitats. Kluwer Academic/Plenum Publishers, New York.

McGee E.M., and Turnbull, W.D. 2010. A paleopopulation of *Coryphodon* lobatus (Mammalia: Pantodonta) from Deardorff hill *Coryphodon* quarry, Piceance Creek Basin, Colorado. Fieldiana Geology 52: 1–12.

Secord, R., Bloch, J.I., Chester, S.G.B., Boyer, D.M., Wood, A.R., Wing, S.L., Kraus, M.J., McInerney, F.A., and Krigbaum, J. 2012. Evolution of the earliest horses driven by climate change in the Paleocene-Eocene Thermal Maximum. Science 335: 959–962.

Simons, E.L. 1960. The Paleocene Pantodonta. Transactions of the American Philosophical Society 50: 1–81.

Uhen, M.D., and Gingerich, P.D. 1995. Evolution of *Coryphodon* (Mammalia, Pantodonta) in the late Paleocene and early Eocene of northwestern Wyoming. Contributions from the Museum of Paleontology, University of Michigan 29: 259–289.

Wing, S.L., Harrington, G.J., Smith, F.A., Bloch, J.I., Boyer, D.M., and Freeman, K.H. 2005. Transient floral change and rapid global warming at the Paleocene-Eocene boundary. Science 310: 993–996.

Zachos, J.C., Dickens, G.R., and Zeebe, R.E. 2008. An early Cenozoic perspective on greenhouse warming and carbon-cycle dynamics. Nature 451: 279–283.

Learning Science Through Research
Published by the Keck Geology Consortium

Short Contributions
Keck Geology Consortium
Volume 33
May 2020
doi: 10.18277/AKRSG.2020.33.08

LONG BONE HISTOLOGY OF THE LARGE PALEOGENE MAMMAL *CORYPHODON*

GRANT BOWERS, University of Maryland
Research Advisor: John Merck

INTRODUCTION

Fifty-six million years ago, at the boundary between the Paleocene and Eocene epochs, the Earth's climate increased by around five to eight degrees Celsius for over a hundred thousand years (McInerney & Wing, 2011). This event, known as the Paleocene-Eocene Thermal Maximum (PETM), had a major impact on the biota, and understanding these impacts is of considerable interest due to the parallels between this event and modern anthropogenic climate change. One of these impacts is a dwarfing event that can be seen in several genera that existed during this event (Gingerich, 2003). One animal that dwarfed (albeit after the PETM) is *Coryphodon*, a genus thought to be the earliest mammal to evolve a large body size, at over 500 kg (Uhen and Gingerich, 2003). Its large baseline size and extreme abundance in the fossil record make it a promising case study to examine many body-size-related questions. Previous work on *Coryphodon* body size has been based on estimates of tooth size, and appears to indicate a dwarfing event in the Wasatchian-3 biochron, several hundred meters above the PETM rocks (Fig. 1; Uhen & Gingerich 1995). Before using bone histology to gain a deeper insight into the evolution of body size in *Coryphodon*, the microanatomy of their bones needs to be investigated and described.

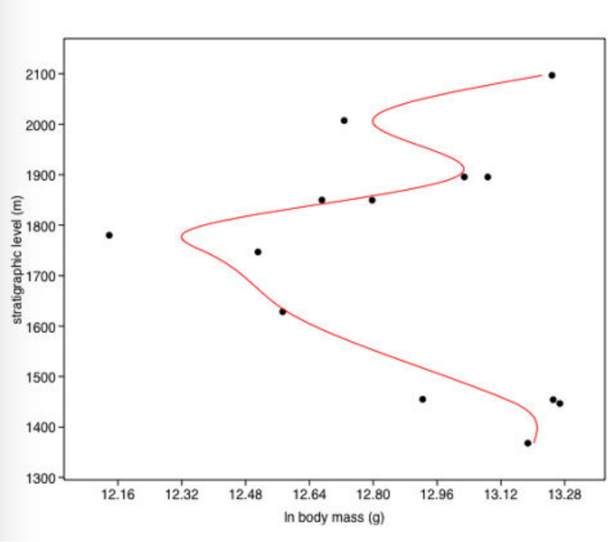

Figure 1. Body mass of Coryphodon (as estimated by molar size) versus the stratigraphic height for specimens in the northern Bighorn Basin (based on data given in Uhen and Gingerich, 1995). Red line is a smoothed average of the values. The PETM occurs around 1500 m.

There are many aspects of bone histology that are useful in learning more about an animal. Bones are often filled with canals that house nerves and blood vessels. These canals are oriented in different ways in different bones, and the organization of these canals can give insight into the rate of bone growth. Another indicator of bone growth rates is the appearance of the bone tissue itself. Bone tissue ranges from slow-growing parallel fibered bone, to lamellar bone, to fast-growing woven bone. Another feature that many vertebrates exhibit is an inborn tendency to briefly slow the addition of new bone to the outer surface once a year, creating a thin dark ring of dense bone for each year that the animal has been alive, called a line of arrested growth (LAG). Alternatively, growth continues without halting as drastically, creating an annulus. Often times, bone is remodeled (usually starting from the center of the bone), absorbing and re-depositing bone tissue. If and when an animal reaches its full size, bone growth will slow, but LAGs will still be laid down, creating an outer ring of tightly packed LAGs called an external fundamental system (EFS) (Padian & Lamm 2013). In addition to its usefulness in analysis of an animal's lifestyle, bone histology can be used in determining the minimum ages of specimens, the relative rate at which they grew, and whether or not they had reached adulthood prior to death. The purpose of this publication is to explore all of these potential applications of *Coryphodon* bone histology.

METHODS

Here I investigate the bone histology of three *Coryphodon* specimens from the University of Michigan (UM), Yale Peabody Museum (YPM) and one collected during the Keck Wyoming field 2019 field season (CORY). These specimens consist of a femur (UM 110898) and two tibiae (CORY 19-22; YPM 35317). The morphology of these bones was preserved through molds, casts, and photogrammetry, prior to preparing thin sections. 3D models of the bone were created through photogrammetry. Thin sections were made on a low-speed diamond saw by making two closely spaced cuts across the bone at a position as close to the midshaft as possible. This wafer was sanded briefly at 600 grit, affixed to a plexiglass slide with cyanoacrylate, and ground to a thickness of about 100 microns. Thin sections were photographed using a Zeiss Axioimager microscope using Zen2 software, producing high-resolution montaged images.

The bone histology is described using terminology established by Padian and Lamm (2013). Patterns of vascularization (reticular, plexiform, laminar, radial, and longitudinal), when not obscured by decomposition or diagenesis, were identified by the directions of the neurovascular canals, which appeared as dark grooves crisscrossing the section (or as holes in the bone in the case of longitudinal canals). LAGs were identified as dark lines that represent a break in tissue around osteons. An EFS, if present, appears as many LAGs packed together near the outer surface of the bone. Annuli were identified as regions of slow growth that stretched around the entire bone.

RESULTS

UM 110898 (femur)

This specimen's histology is well preserved, with decomposition limited to the areas surrounding neurovascular canals (Fig. 2A). The transition from porous inner bone to dense cortical bone is somewhat abrupt, with the cortex occupying the outer third of the bone thickness. The middle of the bone was not microscopically photographed due to file size restrictions of the microscope. The outer cortex of bone contains varying degrees of neurovascular canal infiltration, with some regions having low porosity and others displaying extensive plexiform or reticular vascularization patterns, suggesting somewhat variable rates of bone growth depending on the region of the bone. The overall bone vascularization pattern is reticular in organization, except for the outermost cortex, which is more laminar in nature. A thin layer of many tightly packed dark rings is present around most of the bone's outer edge, likely representing an incipient EFS. However, some neurovascular canals occasionally pierce the outer bone surface all the way around the bone, suggesting that growth had not fully stopped.

CORY 19-22 (tibia)

This specimen's histology is also well preserved, save for a few major cracks and missing parts of the cortex (Figs. 2B, 3). The bone has been crushed taphonomically such that the cortex has been partially pushed into the medullary cavity, and some of the cortex has been lost (Figure 2). The cortex of the bone is relatively thick and dense. The larger cavities in the center are relatively small, and they quickly

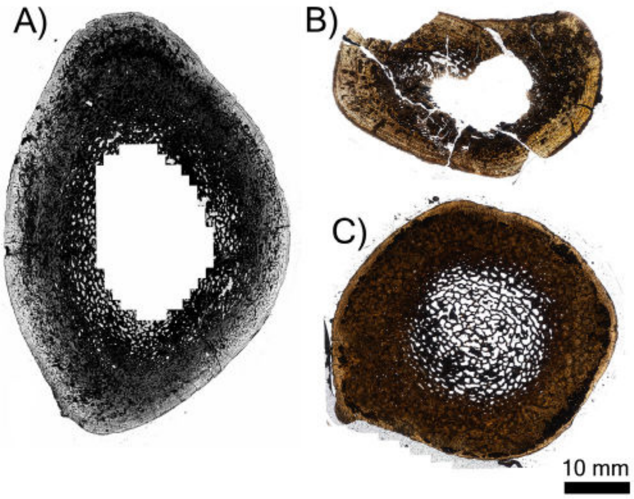

Figure 2. Thin sections examined in this publication: (A) UM 110898 femur (B) CORY19-22 tibia, and (C) YPM 35317 tibia.

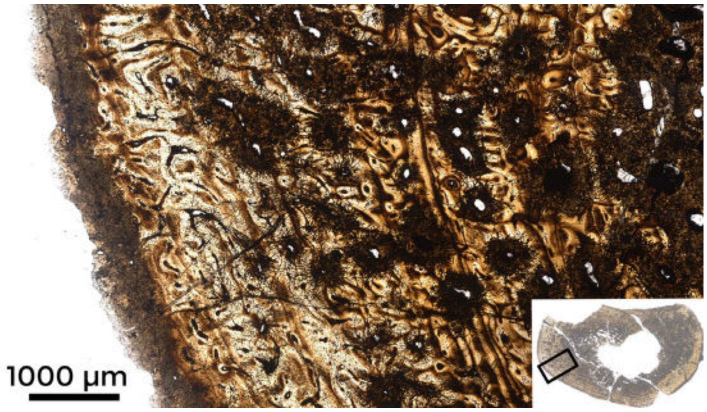

Figure 3. A closeup of the microanatomy of the CORY19-22 tibia section.

transition into small, circular osteons. Most of the osteon edges are obscured by decomposition, making it unclear whether they are primary or secondary. However, sparse remodeling can be observed through the inner half of the cortex. A minimum of four LAGs and/or annuli can be seen, with a possible fifth LAG intersecting the bone surface. This suggests an animal of at least four to five years old, although decomposition and Haversian remodeling have likely obscured more LAGs from earlier in development. The gap between the third and fourth LAG from the center is much larger and filled with much more reticular bone, suggesting a period of rapid growth relative to the slower growth in other stages in life, when LAGs are more closely appressed. No clear EFS can be seen.

YPM 35317 (tibia)

This bone is uncrushed, although most of the inner bone structure has been decomposed, save for the margin near where the periosteum would be in life (Fig. 2C). The bone is overall dense, with the porous inner region being composed of small canals all the way through. At around halfway to the bone surface, there is an abrupt transition from porous bone to dense cortical bone with few canals. The overall vascularization pattern is longitudinal with some circumferential and radial anastomoses. Within the outermost millimeter or so of the cortex, a single inner LAG is present, followed externally by a series of at least eight dark lines packed against the outer surface, representing an EFS.

DISCUSSION

Even with the varying quality of preservation, most major elements of bone histology were identified in the sections, including the presence of LAGs, external fundamental systems, secondary remodeling, variable vascular patterns, and porous medullary cavities. Beyond comparison with other genera, it is clear that *Coryphodon* bones contain the necessary histological data needed to compare bone growth between *Coryphodon* specimens of different sizes, time periods, and localities.

This study demonstrates that secondary remodeling obscures about the first half of the growth record in *Coryphodon* thin sections. This makes it difficult to determine the absolute age of an individual, but a minimum age can be obtained. However, there are many techniques that can calculate the number of LAGs lost during ontogeny, ranging from simple estimations to complex modeling approaches (e.g., Lee & O'Connor 2013).

In sum, there are many future applications of the study of *Coryphodon*'s bone histology, from learning more about the animal's life to answering broader questions about how body size changed over time, and what developmental mechanisms caused this change.

ACKNOWLEDGMENTS

This research is supported by the Keck Geology Consortium and the National Science Foundation under Grant No.1659322. Thanks to D. Brinkman and M. Fox (YPM) and P.D. Gingerich, J. A. Wilson, and A. Rountrey (UM) for collections access and to my research advisors (Michael D'Emic, Simone Hoffmann, John Merck) and fellow Keck researchers: Emily Randall, Danika Mayback, Richard Gonzalez, Isaac Sageman, and Michael Ford.

REFERENCES

Gingerich, P.D. (2003). Mammalian responses to climate change at the Paleocene-Eocene boundary: Polecat Bench record in the northern Bighorn Basin, Wyoming. Geological Society of America Special Paper 369.

Lee, A. & O'Connor, P. (2013). Bone histology confirms determinate growth and small body size in the noasaurid theropod Masiakasaurus knopfleri. Journal of Vertebrate Paleontology. 33. 10.1080/02724634.2013.743898.

McInerney, F. A., & Wing, S. L. (2011). The Paleocene-Eocene Thermal Maximum: a perturbation of carbon cycle, climate, and biosphere with implications for the future. Annual Review of Earth and Planetary Sciences, 39:489-516. doi:10.1146/annurev-earth-040610-133431

Padian, K. & Lamm, E-T. (2013). Bone histology of fossil tetrapods: Advancing methods, analysis, and interpretation.

Uhen, M. & Gingerich, P. (1995). Evolution of *Coryphodon* (Mammalia, Pantodonta) in the Late Paleocene and Early Eocene of Northwestern Wyoming. Contributions from the Museum of Paleontology, the University of Michigan. 29.

KECK Geology Consortium

Learning Science Through Research

Published by the Keck Geology Consortium

Short Contributions
Keck Geology Consortium
Volume 33
May 2020
doi: 10.18277/AKRSG.2020.33.09

ESTIMATING THE BODY MASS OF THE LARGE PALEOGENE MAMMAL *CORYPHODON*

RICHARD GONZALEZ, University of Texas at San Antonio
Research Advisor: Thomas Adams

INTRODUCTION

Coryphodon is an abundant large-bodied Paleogene mammal with a Holarctic distribution. It was among the first mammalian megaherbivores to evolve. Using body estimates based on tooth area, it has been inferred that *Coryphodon* underwent dwarfing during the Eocene (Uhen and Gingerich, 1995), similar to many other mammalian lineages (Gingerich 2003; Secord et al., 2012; D'Ambrosia et al., 2017). However, the original inference of dwarfing in *Coryphodon* was based on a small fraction of its available fossil record, prompting reanalysis herein with a larger dataset. Most *Coryphodon* specimens in museums are fragmentary, consisting of one or more partial limb elements and/or teeth that were opportunistically surface collected (Fig. 1). The first major goal of this research is to test whether various skeletal elements tightly scale with one another, such that missing skeletal data can be predicted, and more of the *Coryphodon* record be incorporated into study of its body mass evolution.

The second major goal of this research is to apply the robust universal scaling relationship between stylopodial diaphyseal circumference and body mass to *Coryphodon* data. This relationship was established much more recently than the 1995 study of tooth area (Campione and Evans, 2012) and has yet to be applied to *Coryphodon*. We aim to compare the stylopodial-derived and tooth-area-derived masses of *Coryphodon* to better characterize its body mass evolution.

Figure 1. Typical preservation of Coryphodon fossils as they are found in museum collections (YPM 16131). Most specimens in museums were not quarried but were opportunistically surface collected over the past century and a half in various basins across the western United States. Note that despite the fragmentary nature of the collected material, several osteological measures that could scale tightly with body mass are preserved, such as limb bone circumferences and tooth areas.

METHODS

Limb bone diaphyseal least circumferences and lower first molar lengths and widths of *Coryphodon* specimens were measured in the collections of the American Museum of Natural History (AMNH), University of Michigan Museum of Paleontology (UM), specimens collected by Ken Rose from the southern Bighorn Basin (KR), and the Yale Peabody Museum (YPM), with digital calipers for smaller specimens, and flexible measuring tape for larger specimens. For this study, 11 specimens that preserve both a humerus and femur, ten specimens that preserve both a tibia and femur, nine specimens that preserve both a radius and femur, and seven specimens that preserve both a lower first molar and femur were measured. Three linear regressions were created in PAST3 (Hammer et al., 2001) to predict femoral circumference from humeral, radial, and tibial circumference. To assess the strength of the linear relationships between variables, we examined R2, p-value, and percent prediction error (i.e., ((observed value – predicted value)/ predicted value) * 100; Van Valkenburgh, 1990). We also compared *Coryphodon* body mass estimates based on lower first molar area (following Uhen and Gingerich, 1995 and Legendre, 1989) using the following equation:

$$\ln(\text{body mass}) = 1.5133 * (\ln(\text{length} * \text{width of lower first molar})) + 3.6515$$

versus stylopodial limb bone diaphyseal circumferences (following Campione and Evans, 2012) using the following equation:

$$\log(\text{body mass}) = 2.754 * (\log(\text{combined stylopodial circumferences})) - 1.097$$

RESULTS

The circumference of the femur is readily predicted by the circumference of the humerus, the radius, and the tibia (Fig. 2, Table 1), with regressions yielding low percent prediction errors and p-values and high R2 values. These tight relationships were recovered despite the slight-to-severe diaphyseal crushing common to *Coryphodon* specimens, suggesting that perhaps absent this crushing, these relationships could be even stronger.

Body mass estimates based on tooth area in seven *Coryphodon* specimens of various size ranged from 344–772 kg; body mass estimates based on combined stylopodial least diaphyseal circumferences in these same 7 specimens ranged from 358–1172 kg (Table 2). Tooth area-derived body mass estimates are on average only 80% body mass estimates from limb bone circumferences (Table 2), with smaller specimens showing closer correspondence in estimates (~90%) than larger specimens (~70%).

Table 1. Summary statistics for relationships among *Coryphodon* long bones.

independent variable (x)	**dependent variable (y)**	**R^2**	***p***	**% prediction error**
tibia circumference	femur circumference	0.98	5×10^{-8}	4
radius circumference	femur circumference	0.88	0.0002	5
humerus circumference	femur circumference	0.88	2×10^{-5}	9

Note: The circumference of the humerus, radius, and tibia can each predict femoral circumference with a great deal of confidence.

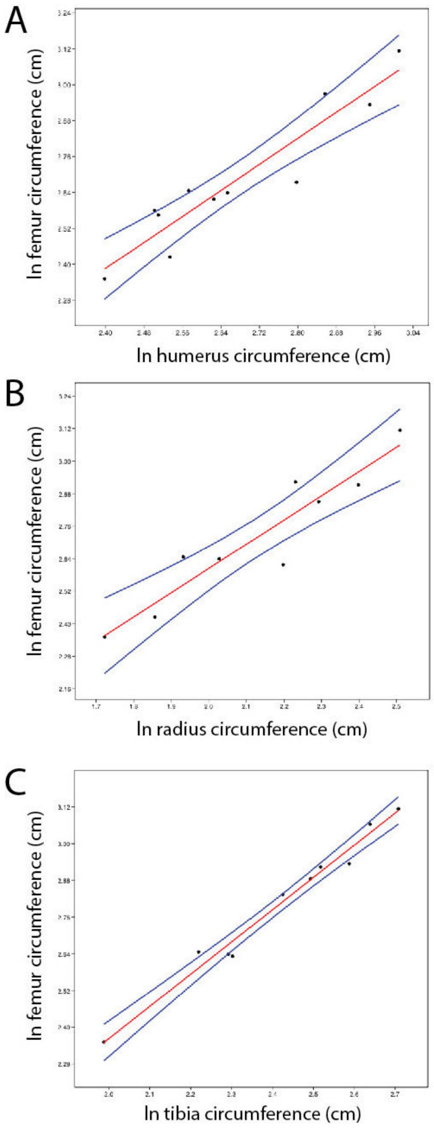

Figure 2. Linear regressions of skeletal dimensions of Coryphodon long bones. The circumference of the humerus, radius, and tibia can each predict femoral circumference with a great deal of confidence. See Table 1 for statistical values associated with each regression.

DISCUSSION

This study examined two sets of relationships: first, the tightness of relationships among limb bone circumferences in *Coryphodon*, and second, the difference in body mass estimates using tooth area versus stylopodial limb circumferences. For the first aim, discovery of three tight scaling relationships means that isolated tibial, radial, and humeral limb

Table 2. Difference in body mass estimates based on tooth area versus those based on stylopodial limb circumference in *Coryphodon*.

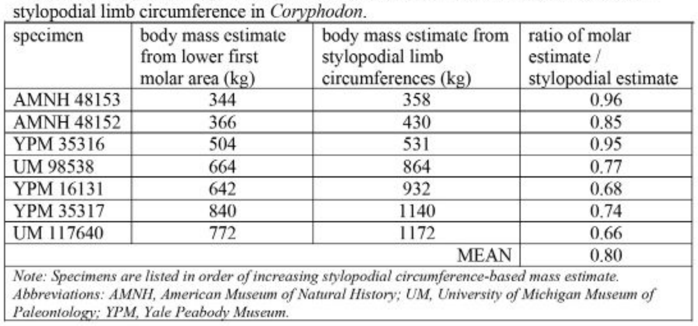

specimen	body mass estimate from lower first molar area (kg)	body mass estimate from stylopodial limb circumferences (kg)	ratio of molar estimate / stylopodial estimate
AMNH 48153	344	358	0.96
AMNH 48152	366	430	0.85
YPM 35316	504	531	0.95
UM 98538	664	864	0.77
YPM 16131	642	932	0.68
YPM 35317	840	1140	0.74
UM 117640	772	1172	0.66
		MEAN	0.80

Note: Specimens are listed in order of increasing stylopodial circumference-based mass estimate. Abbreviations: AMNH, American Museum of Natural History; UM, University of Michigan Museum of Paleontology; YPM, Yale Peabody Museum.

shafts can be used to estimate femoral circumference in *Coryphodon*. Humeral and femoral circumference is nearly equal in *Coryphodon*, indicating that body mass was roughly evenly distributed to the forelimbs and hindlimbs. Concerning the second part of the analysis, we found that tooth area substantially underestimates *Coryphodon* body mass, a problem already noted for several Paleogene taxa (Damuth, 1990), and that generally the larger the *Coryphodon* specimen, the worse tooth area is for predicting body mass. Future work will be able to utilize the scaling relationships discovered herein to estimate body mass in *Coryphodon* through time using both more accurate estimators and a much larger proportion of its considerable fossil record.

ACKNOWLEDGMENTS

Funding for this study was provided by the Keck Geology Consortium and the National Science Foundation (NSF REU-1659322). Thanks to D. Brinkman (YPM), J. Galkin (AMNH), and A. Rountrey, J.A. Wilson, and P.D. Gingerich (UM) for collections access. Thanks to my research advisors Michael D'Emic, Simone Hoffmann, Brady Foreman, and Thomas Adams, and our Keck team: Danika, Emily, Grant, Isaac, and Michael.

REFERENCES

D'Ambrosia, A.R., Clyde, W.C., Fricke, Gingerich, P.D., Abels, H.A. 2017. Repetitive mammalian dwarfing during ancient greenhouse warming events. Science Advances 3: e1601430.

Damuth, J. 1990. Problems in estimating body masses of archaic ungulates using dental measurements. pp. 229–253 in: Body size in mammalian paleobiology: Estimation and biological implications (Damuth, J. and MacFadden, B.J., eds.). Cambridge University Press, New York.

Gingerich, P.D. 2003. Mammalian responses to climate change at the Paleocene-Eocene boundary: Polecat Bench record in the northern Bighorn Basin, Wyoming. In S.L. Wing, P.D. Gingerich, B. Schmitz, and E. Thomas (eds.), Causes and consequences of globally warm climates in the early Paleogene, Geological Society of America, Special Paper 369: 463–478.

Legendre, S. 1989. Les communautés de mammifères du Paléogène (Éocène supérieur et Oligocène) d'Europe occidentale : structures, milieux et evolution. Münchner Geowissenschaftliche Abhandlugen, Reihe A, Geologie und Paläontologie. 16:1–110.

Hammer, Ø., Harper, D.A.T., Ryan, P.D. 2001. PAST: Paleontological statistics software package for education and data analysis. Palaeontologia Electronica 4: 9pp. http://palaeo-electronica.org/2001_1/past/issue1_01.htm

Secord, R., Bloch, J.I., Chester, S.B., Boyer, D.M., Wood, A.R., Wing, S.L., Kraus, M.J., McInerney, F.A., Krigbaum, J. 2012. Evolution of the earliest horses driven by climate change in the Paleocene-Eocene thermal maximum. Science 335: 959–962.

Uhen, M., and Gingrich, P.D. 1995. Evolution of *Coryphodon* (Mammalia, Pantodonta) in the Late Paleocene and Early Eocene of Northwestern Wyoming. Contributions From The Museum of Paleontology, University Of Michigan. 29:259–289.

Van Valkenburgh, B. 1990. Skeletal and dental predictors of body mass in carnivores. pp. 181–206 in: Body size in mammalian paleobiology: Estimation and biological implications (Damuth, J. and MacFadden, B.J., eds.). Cambridge University Press, New York.

KECK Geology Consortium
Learning Science Through Research
Published by the Keck Geology Consortium
Short Contributions
Keck Geology Consortium
Volume 33
May 2020
doi: 10.18277/AKRSG.2020.33.10

USING CEMENTUM HISTOLOGY TO ESTIMATE AGE IN THE PALEOGENE MAMMAL *CORYPHODON*

DANIKA MAYBACK, Illinois State University
Research Advisor: David Malone

INTRODUCTION

Acellular extrinsic cementum is a continuously growing tissue that anchors the tooth root to the alveolar bone and has the potential to record life history traits such as age of an individual (Klevezal, 1996). Cementochronology offers an alternative to bone histology in determining the age of fossil individuals (Newham et al., 2019). In contrast to bone, cementum growth layers do not remodel nor get resorbed. In this study, we aim to use cementochronology to age the fossil mammal Coryphodon. The Paleocene to Eocene Coryphodon is one of the first placental mammals to reach large body size (over 500 kg) after the K-Pg extinction event and is hypothesized to have undergone dwarfing in the Eocene as a response to increased temperature and a drier, more seasonal climate (Uhen & Gingerich, 1995). Whether Coryphodon extended or accelerated its development to achieve larger body sizes and/or if the rapid climatic shifts impacted growth rate and longevity are unknown. The Bighorn Basin in Wyoming is an ideal area to study changes of life history traits in fossil communities. The Fort Union and Willwood Formation strata are extensive in the Bighorn Basin. These strata preserve a dense fossil record and high-resolution carbon and oxygen record at the Paleocene-Eocene boundary, which is known for sudden faunal turnover and climate change (Gingerich, 2003).

The Paleocene-Eocene Thermal Maximum (PETM) is an abrupt global warming event ~56 Mya caused by the release of thousands of petagrams of carbon most likely released from thermogenic methane from organic materials and accumulated carbon stock in Antarctic permafrost (McInerney & Wing, 2011). The most notable consequences of the PETM on mammals are speciation, diversification, and body-size evolution (Clyde & Gingerich, 1998; Gingerich, 2003). At Wasatchian-0, several species dwarf and later rebound concurrently with the duration of the PETM (Secord et al., 2012). Bergmann's Rule states that body-size decreases with warming temperatures and increases with cooling temperatures by the optimization of body size through thermoregulation and availability of food sources. This could explain dwarfing in Coryphodon, but more sampling and testing are needed. No previous research exists to explain how growth rates and lifespan may have changed to cause dwarfing. Cementochronology will be used to estimate ages for collected Coryphodon specimens and evaluate usefulness in comparison to bone histology. To do so, we sampled Coryphodon specimens from several Wasatchian and Clarkforkian biozones in the Bighorn Basin of Wyoming.

BACKGROUND

Cementum is a dental tissue that surrounds the tooth root and attaches it through the periodontal ligament to the alveolar bone. Gonçalves et al. (2004) describes three principal types: acellular afibrillar cementum, cellular intrinsic fiber cementum, and acellular extrinsic fiber cementum. Acellular afibrillar cementum forms in minor amounts along the cementoenamel junction with little known significance. Cellular intrinsic cementum mineralizes collagen fibers parallel to the root surface containing cementocytes on the apical portion. This type grows faster and aids in repairing resorption lacunae and fractures. Acellular extrinsic fiber cementum is found on the cervical, middle, and some of the apical portion of the root. This type serves the purpose of anchoring the root through the peridontal ligament to the alveolar bone. The part of the peridontal ligament that connects to the cement is called Sharpey's fibers—short, connective collagen bundles oriented perpendicular to the root surface. Both cellular and acellular cementum grow continuously in concentric layers around the root. Light and dark bands are caused by a variation in relative mineralization and collagen orientation from seasonal variations in nutrition, biomechanics, and cyclic hormone factors. (Lieberman, 1994).

The seasonal banding pattern of cementum is useful for estimating age. Cementochronology has been used to estimate age in humans in forensic and archeological investigations (Foster, 2017). One of the first comprehensive reviews of cementochronology in extant mammals can be found in Klevezal (1996). Since then, cementochronology has also been applied to estimate ages of fossil mammals and for determining mortality and seasonality information in the fossil record (Stutz, 2002). In one study, the lifespans of Jurassic stem-mammals were determined using incremental tooth histology to calculate basal metabolic rates (Newham et al., 2019).

METHODOLOGY

Coryphodon specimens were collected from the Clarkforkian to Wasatchian biozones of the Fort Union and Willwood Formations in the Bighorn Basin of Wyoming. Of these, six teeth were sampled for histology, including four canines, two premolars, and one incisor. In addition, four teeth were sampled from the Yale Peabody Museum (YPM). These consist of two canines (YPM 14723, 16131), and two premolars (YPM 14723, 17800).

Specimens were photographed for photogrammetric reconstruction before sampling. Each specimen was placed in a lightbox and photos of each sample were taken at low, moderate, and high angles by rotating a stage, from which photogrammetric models can be created. In addition to photogrammetry, the external morphology of the specimens was preserved through molding and casting before cutting the teeth to make ground thin sections. The roots were sampled near the apical one third because the most acellular extrinsic cementum mineralizes there (Newham et al., 2019). Several samples were also cut longitudinally, but cross sections were found to better depict the layers of cementum. Next, samples were smoothed and polished using sandpaper and mounted to slides with epoxy. The samples were again cut and ground to a thickness of 100 μm or less until optimal viewing conditions were realized Thin sections were photographed using an Axiocam 503 camera under magnification on a Zeiss Axioimager Z2, and montaged with Zen2 software.

The montages were imported into Adobe Illustrator CS6 for analysis. The cementum could be identified starting at the cemento-dentin junction as visible growth layer groups with countable annulation lines. The preservation quality assessed for each photo was determined based on the presence of Sharpey's fibers and lacunae from cementocytes formed during cementogenesis. Excellently preserved specimens include both preservation features with countable cementum lines. Moderately well preserved specimens lack the detail in preservation but have visible lines. Poorly preserved specimens are unusable with no preservation of lines, lacunae, or Sharpey's fibers. In Illustrator, each image was locked in the first layer and an additional layer was used for tracing the lines of growth. For CORY 19-29, an additional layer was added for uncertain lines as the cementum lines for this sample are irregular and more difficult to follow. Lines were traced using the pencil tool and various colors were used to correlate the same lines across long layers. The lines were counted to find an estimated age for each Coryphodon individual.

RESULTS

Below we describe each specimen, from best to worst preserved.

Excellently preserved Specimens

CORY 19-29 (Fig. 1A) is a canine. The central region consists of the dentin of the canine. The cementum is preserved between the dentin and alveolar bone. Both the dentin and cementum preserve clear growth layers. The concentric rings of the dentine are cross-

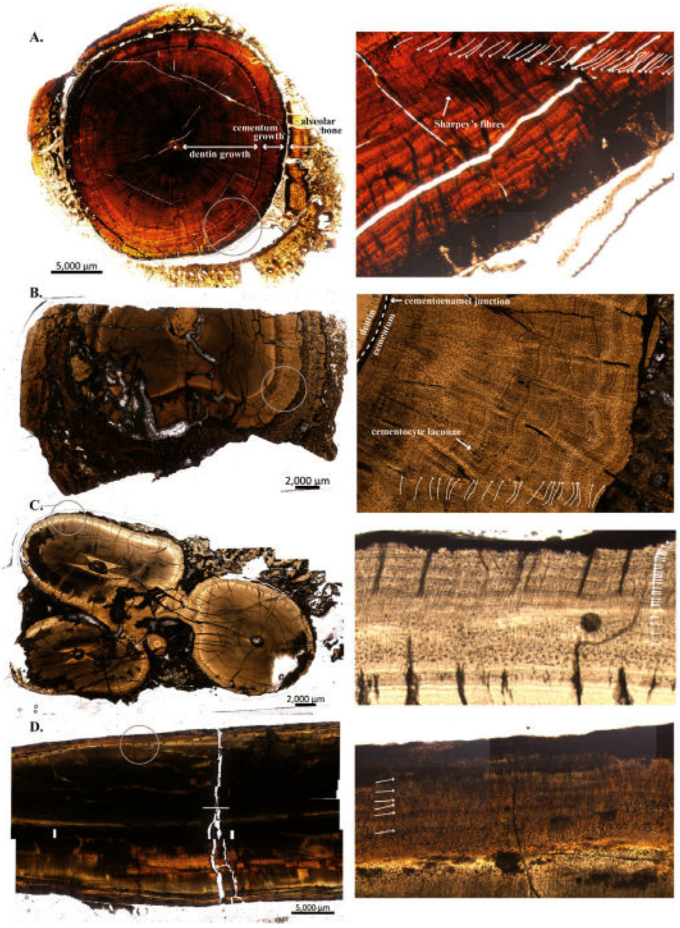

Figure 1. Tooth histology of excellent specimens A) canine (CORY 19-29), B) canine (YPM 14723), C) premolar (YPM 14723), and D) canine (YPM 16131). Individual growth layers indicated by arrows. Enlarged area to the right of each image. Examples of dentin, cementum, cementoenamel junction, cementocyte lacunae, Sharpey's fibres, and alveolar bone are indicated.

cut perpendicularly by lines extending from the center. The cementum is identified in this sample by its wavy pattern of lines caused by uneven growth and spotted texture from the presence of cementocyte lacunae. Evidence of Sharpey's Fibres is left behind by the long dark lines cross cutting growth layers. This specimen has a line count of 33 demonstrating that Coryphodon had a lifespan extending past three decades.

YPM 14723 (Fig. 1B) is another canine. Similar to CORY19-29, the cementum is identified surrounding the inner dentin and shows preservation of cementocytes and Sharpey's fibres. The outer half of the growth layers are well preserved and have an estimated count of 22 lines. Unfortunately, the innermost layers are not well preserved enough to be countable. At a minimum, this individual exceeded two decades in age, but may have lived much longer as suggested by the overall thickness of the cementum layer.

YPM 14723 (Fig. 1C) is a premolar of the same specimen as the canine above. The cementum is clearly distinguishable between the dentine and bone. Both the cementum and dentine preserve incremental growth layers. The cementum is identified surrounding the dentin and shows preservation of cementocytes and Sharpey's fibres. Similar to the canine the outer part of cementum is much better preserved than the inner part (with each part being about equal in thickness). The outer part preserves up to 28 layers.

YPM 16131 (Fig. 1D) is a canine and was cut in a longitudinal section. The dentin is similar to the previous two samples, but the cementum noticeably changes character around the sides of the tooth. Some areas had flat, even lines while others were too dark, too close together, or not well preserved. The dentin is preserved well and lacunae and Sharpey's fibres are present. A minimum of six lines are present.

Moderately well preserved Specimens

Intermediate specimens are categorized by having some visible lines but are not as well preserved. The two canines (CORY 19-17, CORY 19-32) assigned to this category are shown in Figure 2. Both specimens show some lines in the cementum and dentine, but the lines cannot be consistently traced. CORY 19-32 preserves at least four cementum lines but the junction between the dentin and cementum is not visible. CORY 19-17 is even more poorly preserved. Although some lines are visible in the dentin the cementum-dentin junction is not recognizable and the cementum can only be identified by its generally wavy nature.

Poorly preserved Specimens

Poor specimens are completely diagenetically altered and are unusable (Fig. 3). No biological structures are visible in the tooth including the cementum in CORY 19-35 (canine), CORY 19-53 (incisor and premolar), and YPM 17800 (premolar).

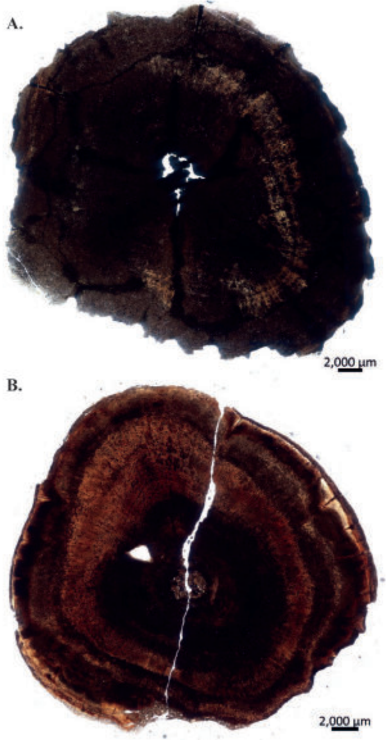

Figure 2. Tooth histology of intermediate specimens A) canine (CORY 19-17) and B) canine (CORY 19-32). Individual growth layers indicated by arrows.

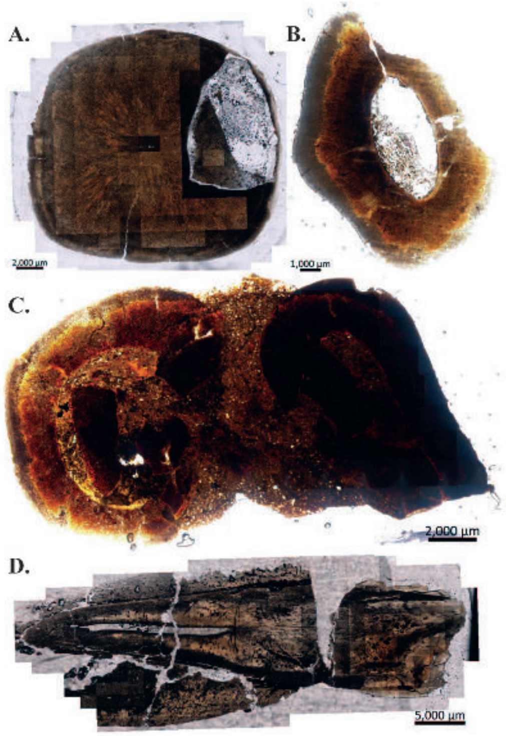

Figure 3. Tooth histology of poor specimens A) canine (CORY 19-35), B) incisor (CORY 19-53), C) premolar (CORY 19-53), D) premolar (YPM 17800).

CONCLUSION

This study demonstrates that cementochronology is a useful tool in vertebrate paleontology to determine ages for individuals. Cementum histology is an alternative to bone histology when bones are incomplete, decomposed, or not present. Cementum also offers several advantages as it is not usually subject to resorption, is not vascularized, and has a very regular, incremental pattern (Stutz, 2002). Three of the specimens sampled herein were deemed sufficiently preserved to give reliable age estimates based on preservation of Sharpey's fibres and lacunae. Specimens studied had just a few to almost 30 growth layer groups. This is the first study to demonstrate that Coryphodon reached several decades in age. Based on these data, we can start to understand how changes in lifespan might have influenced changes in body size of Coryphodon during the Paleogene. Overall, cementochronology has great potential to be a useful method for studying body size evolution in the fossil record.

ACKNOWLEDGEMENTS

Funding for this study was provided by the Keck Geology Consortium and the National Science Foundation (NSF-REU1659322). I would like to thank my advisors Simone Hoffmann and Michael D'Emic for their mentorship throughout the project. Additionally, I would like to thank the Keck Wyoming team: Emily, Isaac, Richard, Michael, and Grant. I would also like to thank everyone at The Yellowstone Bighorn Research Association for their support during our fieldwork. Finally, I would like to thank Illinois State University Department of Geography and Geology for all of their support throughout this project.

REFERENCES

Clyde, W.C., and Gingerich, P.D. 1998. Mammalian community response to the latest Paleocene thermal maximum: An isotaphonomic study in the northern Bighorn Basin, Wyoming. Geology 26:1011–1014.

Foster, B. 2017. On the discovery of cementum. Journal of Periodontal Research 52:666–685.

Gonçalves, P.F., Sallum, E.A., Sallum, A.W., Casati, M.Z., Toledo, S., and Nociti, F., 2005, Dental cementum reviewed: Development, structure, composition, regeneration and potential functions: Braz J Oral Sci, v. 4, p. 651–658.

Gingerich, P. 2003. Mammalian responses to climate change at the Paleocene-Eocene boundary: Polecat Bench record in the northern Bighorn Basin, Wyoming. Geological Society of America Special Paper 369:463–478.

Klevezal, G. 1996. Recording Structures of Mammals: Determination of Age and Reconstruction of Life History. Balkema, pp. 274.

Lieberman, D.E. 1994. The Biological basis for seasonal increments in dental cementum and their application to archaeological research. Journal of Archaeological Science 21:525–539.

McInerney, F.A., and Wing, S.L. 2011. The Paleocene-Eocene Thermal Maximum: perturbation of carbon cycle, climate, and biosphere with implications for the future. Annual Review of Earth and Planetary Sciences 39:489–516.

Newham, E., Gill, P.G., Brewer, P., Benton, M.J., Fernandez, V., Gostling, N.J., Haberthür, D., Jernvall, J., Kankanpää, T., Kallonen, A., Navarro, C., Pacureanu, A., Zeller-Plumhoff, B., Richards, K., Robson-Brown, K., Schneider, P., Suhonen, H., Tafforeau, P., Williams, K., and Corfe, I.J. 2019. Reptile-like physiology in Early Jurassic stem-mammals: bioRxiv 785360, doi:10.1101/785360.

Secord, R., Bloch, J.I., Chester, S.G.B., Boyer, D.M., Wood, A.R., Wing, S.L., Kraus, M.J., McInerney, F.A., and Krigbaum, J. 2012. Evolution of the earliest horses driven by climate change in the Paleocene-Eocene Thermal Maximum. Science 33:959–956.

Stutz, A.J. 2002. Polarizing microscopy identification of chemical diagenesis in archaeological cementum. Journal of Archaeological Science 2:1327–1347.

Uhen, M.D., and Gingerich, P.D. 1995. Evolution of Coryphodon (Mammalia, Pantodonta) in the late Paleocene and early Eocene of northwestern Wyoming. Contributions from the Museum of Paleontology, University of Michigan 29: 259–289.

KECK Geology Consortium
Learning Science Through Research
Published by the Keck Geology Consortium
Short Contributions
Keck Geology Consortium
Volume 33
May 2020
doi: 10.18277/AKRSG.2020.33.11

PALEOENVIRONMENTS CONTAINING *CORYPHODON* IN THE FORT UNION AND WILLWOOD FORMATIONS SPANNING THE PALEOCENE-EOCENE THERMAL MAXIMUM (PETM), BIGHORN BASIN, WYOMING

EMILY RANDALL, The College of Wooster
Research Advisor: Mark Wilson

INTRODUCTION

The burning of fossil fuels supports many modern conveniences, but their emissions are also raising greenhouse gas concentrations in the atmosphere, which are increasing global temperature and therefore leading to global climate changes. The Paleocene-Eocene Thermal Maximum (PETM), a rapid (~150,000 years) global warming event (5-8°C over less than 20,000 years) about 55.5 million years ago that was due to a massive release of carbon into the atmosphere (McInerney and Wing, 2011; Gingerich, 2019). Therefore, the PETM can act as an analogy for future global warming if fossil fuel emissions continue their upward trend (Gingerich, 2019).

The Bighorn Basin in Wyoming is one locality where PETM-aged rock units are exposed, which makes it an excellent location to study the environmental, floral, and faunal responses to the PETM (Wing et al., 2005; Kraus et al., 2015). Studying these responses can offer insights into how modern-day flora and fauna might respond to modern climate change. Previous research has concluded that some key adaptations, such as dwarfing, helped certain fauna survive the PETM (Secord et al., 2012). However, it is unclear why some of these mammals survived this much drier climate (Clementz et al., 2008; Secord et al., 2012).

The hippopotamus-like Coryphodon (Mammalia, Pantodonta) was the first mammalian megaherbivore (body mass > 1000 kg) (Uhen and Gingerich, 1995). Previous studies have hypothesized that Coryphodon was semi-aquatic based on morphological features of their skeleton and enamel $\delta^{18}O$ values (Clementz et al., 2008). This study tests the hypothesis that Coryphodon will mainly be found in aquatic or semi-aquatic facies throughout the PETM by inferring its depositional environments through sedimentary analysis.

STUDY AREA

The Bighorn Basin is located in northern Wyoming and southernmost Montana. Its well-exposed Fort Union and Willwood Formations in the Sand Coulee area of the northern part of the basin are the focus of this study. This intermontane basin was formed during the Laramide Orogeny within the foreland basin of the earlier Sevier Orogeny (Mackin, 1937; DeCelles, 2004). Its surrounding mountain ranges provided most of the sediment to the basin (Kraus et al., 2015).

The Sand Coulee area has been previously subdivided into a multitude of fossil localities by Gingerich (2001). Specimens observed during our fieldwork were assigned to these localities based on GPS coordinates and elevation data.

METHODS

Field Methods

Data for this study were collected in the Sand Coulee area of the northern Bighorn Basin. We prospected for Coryphodon in a range of biozones surrounding the PETM. The data consist of 14 stratigraphic sections in total, each with a Coryphodon bearing unit. Of these, 11 contained fossils in situ; for the other three, the bone-bearing layer was estimated based on the highest layer where fossils could be surface collected and similarities between bone color and matrix and mottling colors. Sections were measured on freshly exposed bedrock in narrow trenches. Thickness, grain size, matrix type and color, mottling percent and colors (using a Munsell Color Chart), abundance and type of nodules, shrink-swell features such as slickensides and clay cutans, sharpness of contacts, presence of organic matter, vertebrate and invertebrate fossils, and presence or absence of laminations were recorded for each unit.

Soil Morphology Index (SMI) Calculation

Using the methods described in Adams et al. (2011) a soil morphology index (SMI) number was calculated for each paleosol unit, which serves as a proxy for soil moisture at the time of deposition. This index can be used to determine changes in drainage between the units where Coryphodon was found. SMI is based on matrix chroma and the characteristics of nodules. Matrix chroma ranged from 1 to 3 in the study area and is scored accordingly. The presence, size, and abundance of carbonate nodules and yellow-brown siderite nodules are scored with either 0, 3, or 6 points for each of the two types of nodules. The sum of these scores in the SMI number of that unit.

R was used to run a range of statistical tests using the SMI numbers. A chi-square test was run to determine if there is a relationship between the SMI numbers of Coryphodon units and the biozones these units are from. The average SMI of the Coryphodon units in each biozone is normally distributed. Therefore, an ANOVA was run since it is parametric and assumes a normal distribution of the data. A Tukey test was then run to determine which pairing of biozones contained statistically different means of SMI values. Z-score tests were also run between the SMIs of the biozones that the Tukey test found to be significantly different to verify these results. A Z-score above 1.96, which represents the 95th percentile value, means that the sample is statistically different from the population it is being compared to. Finally, a Mann-Whitney U test was run to compare the SMI numbers of pre- and post-PETM stratigraphic units containing Coryphodon. This test was selected because the pre-PETM SMI numbers are not normally distributed (W = 0.55, p-value = 1.4e-05).

Stratigraphic Column Creation

Stratigraphic columns were created for each section in Adobe Illustrator and grouped by North American mammalian biozone. U.S. Geological Survey lithology patterns (Illustrator swatches) were used to indicate rock types. The percentage of mottling was roughly portrayed by the number of mottling shapes present in the unit. Matrix and mottling colors were derived from a Munsell Color Chart.

RGB values were determined using the Virtual Online Color Wheel, which is a visual representation of RGB values calculated by The Munsell Color Science Laboratory (http://www.andrewwerth.com/color/). Since exact RGB equivalents only exist for Munsell colors with even chroma, the other representative colors were estimated. To do this, Munsell colors with exact RGB equivalents were blended in Illustrator using the blending tool to generate RGB representative colors for the Munsell colors with no exact RGB equivalent (i.e. a chroma of 2 and a chroma of 4 to create a color for a chroma of 3).

RESULTS

Stratigraphic Columns

Clarkforkian 2 is represented by 4 columns, Clarkforkian 3 by 6 columns, Wasatchian 1 by 1 column, Wasatchian 2 by 1 column, and Wasatchian 4 by 2 columns. A selection of stratigraphic columns for these biozones is shown in Figures 1-3, the full list of sections containing Coryphodon and their paleoenvironmental interpretations is given in Table 1.

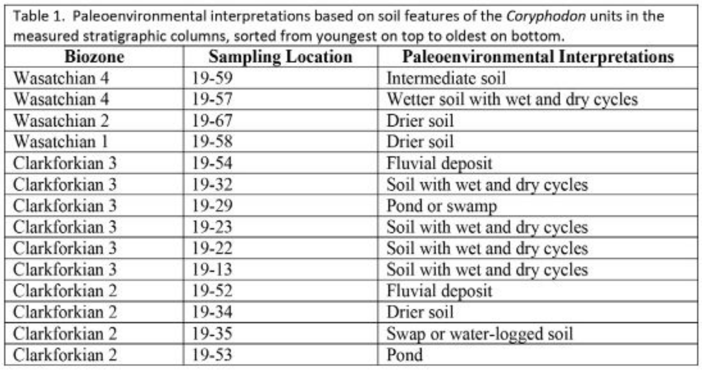

Table 1. Paleoenvironmental interpretations based on soil features of the *Coryphodon* units in the measured stratigraphic columns, sorted from youngest on top to oldest on bottom.

Biozone	Sampling Location	Paleoenvironmental Interpretations
Wasatchian 4	19-59	Intermediate soil
Wasatchian 4	19-57	Wetter soil with wet and dry cycles
Wasatchian 2	19-67	Drier soil
Wasatchian 1	19-58	Drier soil
Clarkforkian 3	19-54	Fluvial deposit
Clarkforkian 3	19-32	Soil with wet and dry cycles
Clarkforkian 3	19-29	Pond or swamp
Clarkforkian 3	19-23	Soil with wet and dry cycles
Clarkforkian 3	19-22	Soil with wet and dry cycles
Clarkforkian 3	19-13	Soil with wet and dry cycles
Clarkforkian 2	19-52	Fluvial deposit
Clarkforkian 2	19-34	Drier soil
Clarkforkian 2	19-35	Swap or water-logged soil
Clarkforkian 2	19-53	Pond

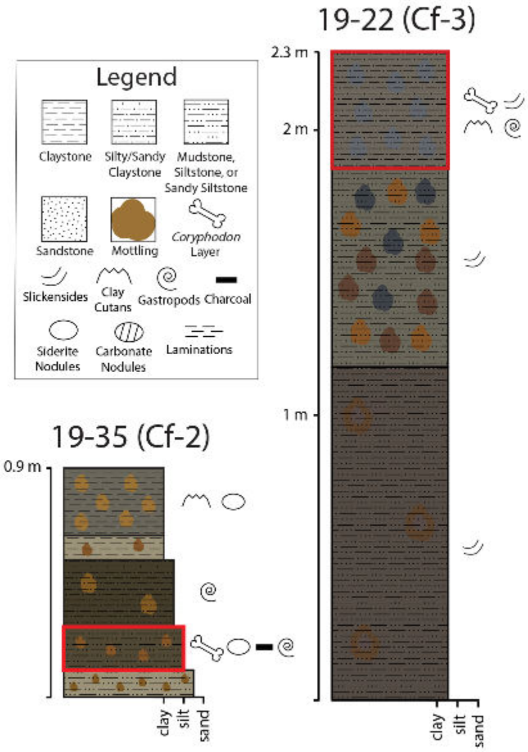

Figure 1. Stratigraphic columns from Clarkforkian (Cf) 2 and 3 mammalian biozones (Pre-PETM). Coryphodon bearing layer outlined in red. Matrix and mottling colors derived from Munsell Color Chart.

Soil Morphology Index (SMI) Numbers

SMI numbers were used to determine if there are statistically significant differences in the wetness of Coryphodon bearing layers among mammalian biozones (Fig. 4). Higher numbers indicate drier conditions whereas lower numbers indicate wetter conditions.

Chi-Square Test

The chi-square test was significant (p-value = 0.014). Therefore, the distribution of counts across categories is not random, so SMI numbers of Coryphodon units are dependent on mammalian biozone. The residuals for a chi-square are the difference between the observed and expected counts by table cell. The greater that residual the more it affects the significance of the chi-square test. The residuals with the greatest contribution to the significant result are a SMI of 15 for Wasatchian 1 (residual contribution of 39.05%), a SMI of 13 for Wasatchian 2 (16.63%), a SMI of 4 for Wasatchian 4 (6.63%), a SMI of 5 for Clarkforkian 2 (5.78%), and a SMI of 7 for Clarkforkian 3 (3.85%).

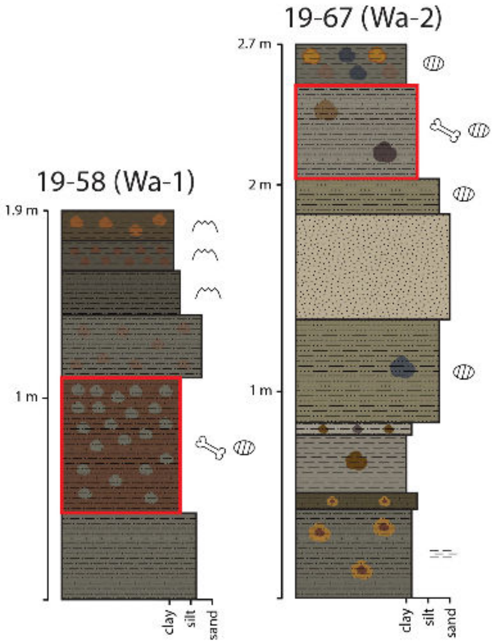

Figure 2. Stratigraphic columns from Wasatchian (Wa) 1 and 2 mammalian biozones (Post-PETM). Coryphodon bearing layer outlined in red. Matrix and mottling colors derived from Munsell Color Chart. Legend in Figure 1.

ANOVA & Z-scores

The ANOVA was significant (p-value = 0.020), which means that the null hypothesis can be rejected and the means of SMI values from at least one pairing of biozones from which these samples were drawn are significantly different. A Tukey test showed that there is a significant difference between the SMI means of Clarkforkian 3 and Wasatchian 1 (p-value = 0.041) as well as Wasatchian 1 and Wasatchian 4 (p-value = 0.03).

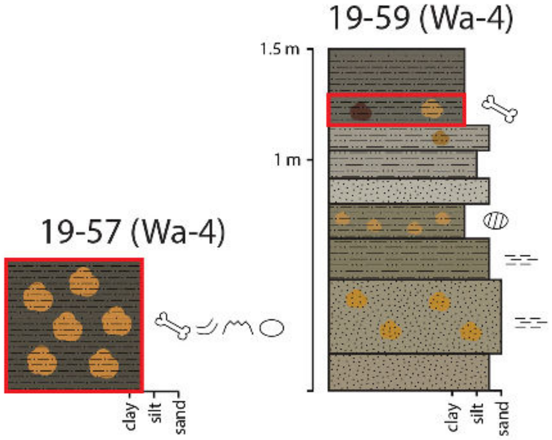

Figure 3. Stratigraphic columns from Wasatchian (Wa) 1 and 2 mammaliaStratigraphic columns from Wasatchian 4 mammalian biozone (Post-PETM). Coryphodon bearing layer outlined in red. Matrix and mottling colors derived from Munsell Color Chart. Legend in Figure 1.

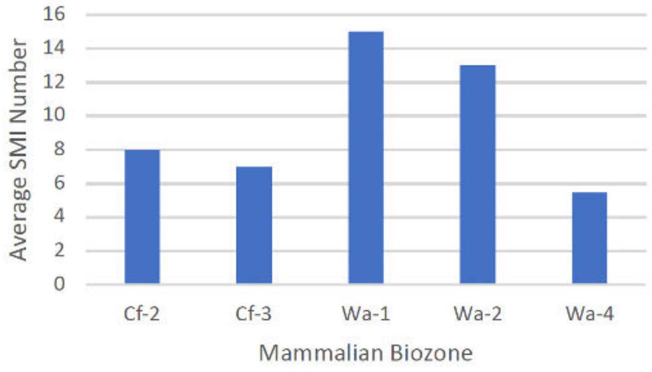

Figure 4. Average SMI number for units containing Coryphodon in each mammalian biozone (except for Wasatchian 0 or 3). Higher number represents a drier stratigraphic unit. Drying of the PETM interval can be observed between Clarkforkian 3 and Wasatchian 1.

Z-score tests supported the results of the Tukey test and showed that the SMI of the Wasatchian 1 sample is an outlier of the SMIs of the Wasatchian 4 "population" and Clarkforkian 3 "population" with respective Z-scores of 4.48 and 0 (standard deviation is 0).

Mann-Whitney U Test

A Mann-Whitney U test yielded a non-significant p-value of 0.5. Therefore, the null hypothesis that the difference in the medians of SMI numbers of the pre- and post-PETM stratigraphic units containing Coryphodon is zero cannot be rejected. This means that these two samples are not statistically significant from one another.

DISCUSSION & CONCLUSIONS

My hypothesis, that the proposed semi-aquatic mammal Coryphodon would mainly be found in aquatic or semi-aquatic facies, is partly supported by the data. In the Clarkforkian 2 and 3, Coryphodon was found mainly in aquatic and semi-aquatic facies as well as in soils with evidence of wet and dry cycles, supporting my hypothesis. However, following the PETM, in Wasatchian 1, 2, and 4, there is only one instance of Coryphodon being found in a wetter soil, and no instances of them in a pond, swamp, or fluvial deposit (Table 1). This preliminary data suggest that Coryphodon was preserved, and might have lived, in wetter habitats before the PETM, but was possibly able to adapt to drier habitats post-PETM.

This potential shift in Coryphodon habitat preference, from aquatic and semi-aquatic to drier paleoenvironments, may be evidence that the changing paleoenvironments that Coryphodon lived in were in large part due to the PETM. However, this result might be influenced by the smaller sample size of specimens post PETM. Additionally, it may be possible that Coryphodon did live in these types of facies but were for some reason fossilized in or at least preserved better in soils as opposed to in swamps, ponds, and rivers in later biozones.

As the sample size of this study is relatively small, especially within biozone groupings, error is an important consideration. Wasatchian 0 and 3 were not represented and only one sample was collected for Wasatchian 1 and 2. Therefore, while the preliminary data does show trends, more fieldwork is crucial to increase the sample size and see if the observed differences of Coryphodon units between biozones still hold.

Additionally, the SMI system, created by Adams et al. (2011), may not be the best way to numerically analyze the data from this area, as many of the layers do not contain any nodules, and the chroma only spanned 1 through 3 (as opposed to 2-6 for Adams et al. (2011)). This means that a large number of the Coryphodon bearing units have an SMI number between 6 and 8, which statistically skews the data towards these central SMI numbers even though there were paleoenvironmental changes between units with the same or very similar SMI numbers. This was particularly evident between soils that contained slickensides or clay cutans, and therefore indicated the presence of wet and dry cycles, and those that did not. Therefore, I propose that the presence or absence of additional sedimentary features should be included in calculating SMI numbers in this study area to have them better represent changing paleoenvironments, as well as make it easier to statistically analyze the differences between these paleoenvironments. Finally, the problem with the current SMI system was evident statistically when running a Mann-Whitney U test to comparing the SMI numbers of the pre- and post-PETM stratigraphic units containing Coryphodon, as this test did not yield a significant result. However, when considering all of the observations, there is a likely shift in the paleoenvironments of Coryphodon that should be studied further through continued fieldwork.

ACKNOWLEDGMENTS

Funding for this study was provided by the Keck Geology Consortium and the National Science Foundation (NSF-REU1659322). I would like to thank my research advisors, Michael D'Emic, Simone Hoffmann, Brady Foreman, and Mark Wilson, as well as the Keck Wyoming team: Danika, Isaac, Richard, Michael, and Grant. I also thank The College of Wooster Earth Sciences Department and The Yellowstone Bighorn Research Association for their support during this project.

REFERENCES

Adams, J.S., Kraus, M.J., and Wing, S.L., 2011, Evaluating the use of weathering indices for determining mean annual precipitation in the ancient stratigraphic record: Palaeogeography, Palaeoclimatology, Palaeoecology, v. 309, p. 358–366.

Clementz, M.T., Holroyd, P.A., and Koch, P.L., 2008, Identifying aquatic habits of herbivorous mammals through stable isotope analysis: Palaios, v. 23, p. 574–585.

DeCelles, P.G., 2004, Late Jurassic to Eocene evolution of the Cordilleran thrust belt and foreland basin system, western U.S.A.: American Journal of Science, v. 304, p. 105–168.

Gingerich, P.D., 2001, Paleocene-Eocene stratigraphy and biotic change in the Bighorn and Clarks Fork Basins, Wyoming: University of Michigan, v. 33, 198 p.

Gingerich, P.D., 2019, Temporal scaling of carbon emission and accumulation rates: modern anthropogenic emissions compared to estimates of PETM-onset accumulation: Paleoceanography and Paleoclimatology, v. 34, p. 329–335.

Kraus, M.J., Woody, D.T., Smith, J.J., and Dukic, V., 2015, Alluvial response to the Paleocene–Eocene Thermal Maximum climatic event, Polecat Bench, Wyoming (U.S.A.): Palaeogeography, Palaeoclimatology, Palaeoecology, v. 435, p. 177–192.

Mackin, J.H., 1937, Erosional history of the Big Horn Basin, Wyoming: GSA Bulletin, v. 48, p. 813–894.

McInerney, F.A., and Wing, S.L., 2011, The Paleocene-Eocene Thermal Maximum: A perturbation of carbon cycle, climate, and biosphere with implications for the future: Annual Review of Earth and Planetary Sciences, v. 39, p. 489–516.

Secord, R., Bloch, J.I., Chester, S.G.B., Boyer, D.M., Wood, A.R., Wing, S.L., Kraus, M.J., McInerney, F.A., and Krigbaum, J., 2012, Evolution of the earliest horses driven by climate change in the Paleocene-Eocene Thermal Maximum: Science, v. 335, p. 959–962.

Uhen, M.D., and Gingerich, P.D., 1995, Evolution of Coryphodon (Mammalia, Pantodonta) in the late Paleocene and early Eocene of northwestern Wyoming: Contributions from the Museum of Paleontology, University of Michigan, v. 29, p. 259–289.

Wing, S.L., Harrington, G.J., Smith, F.A., Bloch, J.I., Boyer, D.M., and Freeman, K.H., 2005, Transient floral change and rapid global warming at the Paleocene-Eocene boundary: Science, v. 310, p. 993–996.

KECK Geology Consortium
Learning Science Through Research
Published by the Keck Geology Consortium

Short Contributions
Keck Geology Consortium
Volume 33
May 2020
doi: 10.18277/AKRSG.2020.33.12

CLIMATIC AND PALEOENVIRONMENTAL CHANGES ASSOCIATED WITH THE EVOLUTION OF *CORYPHODON* THROUGH PALEOGENE HYPERTHERMAL EVENTS, BIGHORN BASIN, WYOMING

ISAAC SAGEMAN, Northwestern University
Research Advisor: Matthew Hurtgen

INTRODUCTION

About 56 million years ago, during the Paleogene period, there was a massive global warming event termed the Paleocene-Eocene Thermal Maximum (PETM). This event featured a worldwide temperature increase of 5–8°C, followed by a long-term warming trend that culminated with the Early Eocene Climatic Optimum (Zachos et al., 2008). This trend was emphasized by hyperthermal events similar, but smaller, to the PETM during the early Eocene (Abels et al., 2015). Climate changes drastically affect the resources available to animals, impacting their geographic ranges, growth rates, and reproductive behaviors (Barnosky et al., 2017). Some mammals experienced rapid dwarfing in response to the PETM and other hyperthermals (Gingerich, 2003; Secord et al., 2012; D'Ambrosia et al., 2017). This dwarfism is hypothesized to result from slower growth rates stemming from lower nutrition levels in plant resources (Gingerich, 2003); change in growth duration could also be a factor (Palkovacs, 2003).

To evaluate changes in body size in the Paleogene mammal *Coryphodon* during Paleogene climate change events, a precise chronostratigraphic framework of each site is necessary. This study seeks to provide such a framework by developing a bulk organic carbon isotope record for more than 20 *Coryphodon* localities from Late Paleocene strata in the Bighorn Basin of Northern Wyoming (Fig. 1A and B). Whereas the lithostratigraphic context of each site is described elsewhere, here I present geochemical analysis of each site in order to test for evidence of the PETM carbon isotope signature.

GEOLOGIC BACKGROUND

This study focuses on a bulk organic carbon isotope record from the Fort Union and Willwood Formations in the Bighorn Basin, Wyoming. The goal of this project is to provide a chronostratigraphic framework

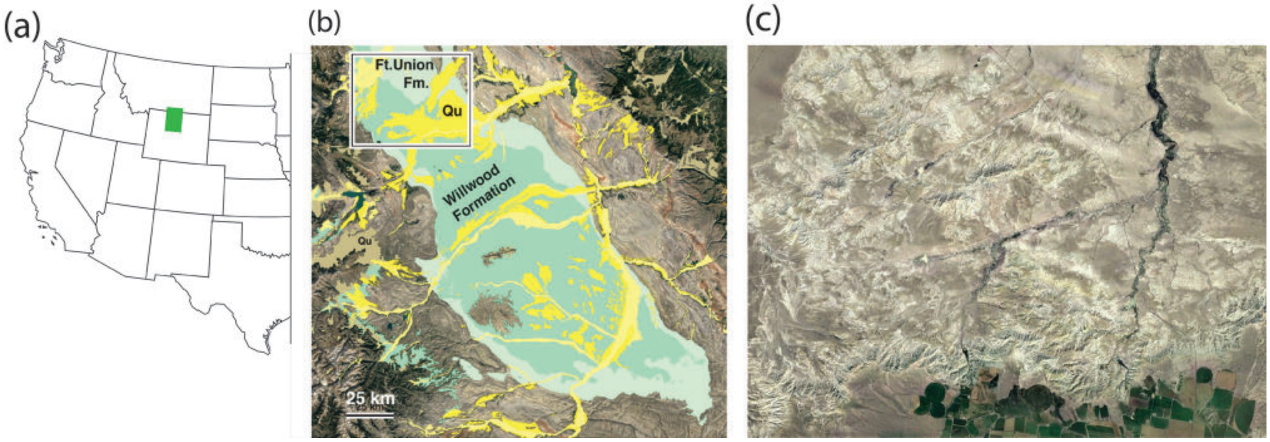

Figure 1. Overview of A) field area within the U.S., B) detail view of formations present in the broader study area, and C) the field area where samples were collected.

for *Coryphodon* samples collected from the Fort Union and Willwood Formations. The PETM is characterized by a prominent negative excursion in the $\delta^{13}C$ of organic matter and carbonate within the Willwood Formation of the Bighorn Basin (Baczynski et al., 2013). Analysis of $\delta^{13}C_{carb}$ in bulk samples of the Fort Union and Willwood Formations captures the isotopic mass balance of all carbonate contributions to the sample, which, based on the studies of Baczynski et al. (2013), could include pedogenic, biogenic, authigenic, and diagenetic carbonate.

METHODS

Fifteen stratigraphic sections containing a *Coryphodon*-bearing layer were measured in the northern Bighorn Basin (Fig. 1C; Fig. 2). Each section was trenched with hand tools and measured using a Jacob's staff while details of the lithofacies were recorded (grain size, soil color, bed contacts/thickness, sedimentary structures, soil mottling, presence of carbonate nodules, bioturbation, shells, fossil layers). Stratigraphic columns were created using Adobe Illustrator. Format and lithology can be seen in the right-hand column of Figure 3. The estimated stratigraphic order of these sections was determined using elevation and location coordinates measured with handheld GPS.

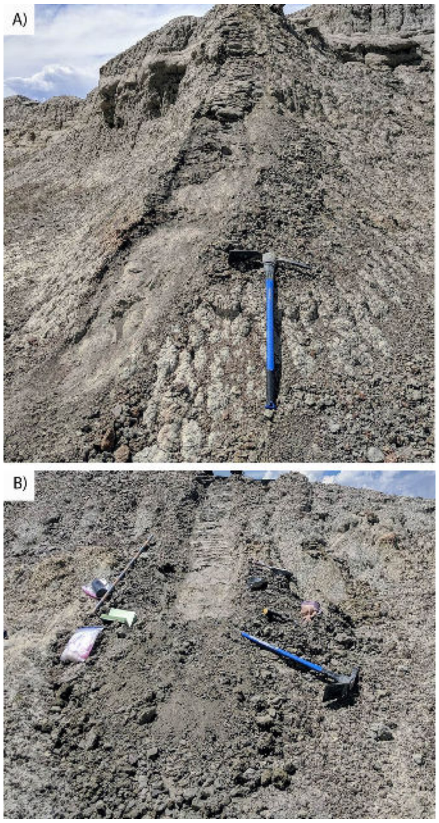

Figure 2. Field photographs of two stratigraphic sections, A) example in Fort Union Formation, and B) example in Willwood Formation.

A total of 93 fist-sized samples were taken at the base of each bed characterized by a different lithology. The samples were prepared for isotopic analysis by using an 8530 Shatterbox for rock crushing. Samples of 2–150 grams were placed into tungsten carbide cylinders with a puck. Three cylinders at a time were placed into the Shatterbox and run for 3 minutes until the sediment was reduced to a fine powder. After the tungsten carbide containers were clear of sample, they were thoroughly washed with DI water and dried using a compressed air stream before being placed into a desiccator for further drying.

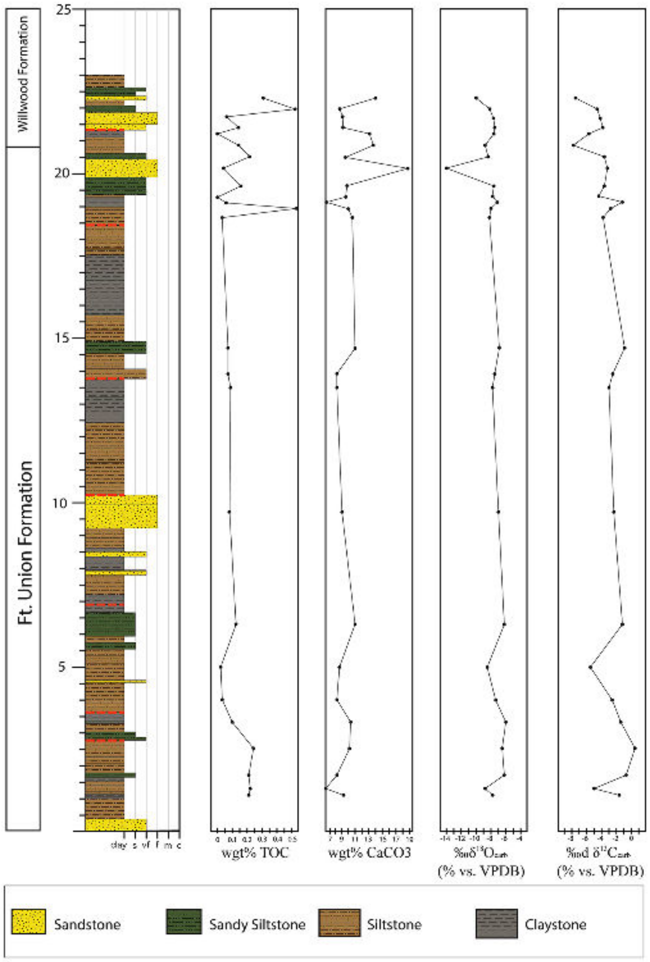

Figure 3. Change in wgt. % Total Organic Carbon (TOC), wgt. % Calcium Carbonate (CaCO3), wgt. ‰ δ13Ccarb, and wgt. ‰ δ18Ocarb up-section. Isotope data is correlated with specific samples from sections TC-01, MD-02, SH-07, KS-04, KS-01, ER-04, MD-19, and IS-07. Red dashed lines signify breaks between each individual stratigraphic column.

Coulometric analysis on a UIC Carbon Coulometer was performed in two steps 1) inorganic carbon assessment using acidification and 2) a total carbon assessment using combustion. The respective inorganic carbon and total carbon phases were converted to CO_2, and the amount of CO_2 evolved was measured coulometrically to yield wgt.% Total Inorganic Carbon (TIC) and wgt. % Total Carbon (TC) values; total organic carbon was determined by difference (TC-TIC), and wgt. % $CaCO_3$ was calculated from stoichiometry (TIC x 8.333). This procedure was done with an automated carbon dioxide coulometric titrator model 5030 following Engleman et al. (1985) for both oven and acid components.

Before weighing out samples for acid or oven analysis, all sample-carrying boats were either acidified or ignited to deplete any leftover material to avoid contamination. Blanks, carrying no sample, were run 3 times for later calculation purposes. Standards of 5.0 mg, 10 mg, 15 mg, 20 mg, and 25 mg ± 1.0 were weighed out using a Sartorius CPA2P Microbalance and ran before any samples in order to make sure the machines were performing correctly. The standards contain 12% $CaCO_3$ and generally the coulometer yields results for standards within 1%, indicating analytical uncertainty. Acid coulometry serves to determine inorganic carbon content of samples through the submersion of samples into 2 N perchloric acid for 5 minutes at a time. Oven coulometry yields the total carbon content of a sample through ignition of sample powders at 720˚C for 7 minutes inside the oven unit. The detection range for the instrument ranges from 0.01µg to 100 mg carbon. Both oven and acid results were recorded for each sample, along with their weights. I employed an external flow rate meter to correct for an inconsistency in flow rate within the oven's gas outlet.

I was able to perform measurements of $\delta^{13}C_{carb}$ by selecting samples with sufficient $CaCO_3$ based on carbon coulometry result;, 25 samples with $CaCO_3$ values of at least 8 wgt.% were selected for analysis. 400 ± 10 µg of each viable sample were weighed out using a Sartorius CPA2P Microbalance, transferred to Gasbench vials with pressure-sealed caps and measured on a Thermo Delta V plus.

RESULTS

Field Observations

The measured stratigraphic sections consisted of interbedded thin, diagenetically altered mud and claystone units as well as thin-bedded, light colored fluvial sandstones and conglomerates. The sandstone beds tended to be more massive and ranged from silty, very fine, to fine-grained. The diagenetically altered strata were mainly paleosol starting in the Fort Union Formation and continuing up through the Willwood Formation. These rhythmically alternating units are clearly visible in outcrop, as well as in the coulometry data described below.

Coulometry

Carbon coulometry resulted in $CaCO_3$ and TOC data that were useful for interpretation of facies changes, and guided the selection of samples for isotopic analysis. The data are illustrated in Figure 4 Values of wgt. % TC vary in a cyclic pattern going up-section, having an average value of 0.58% until the MD-19 section (Fig. 3 and 4) is reached, at which point the average increases to 1.48%. This change is additionally indicated in the other datasets, as the average wgt. % $CaCO_3$ raises from 3.82 up to 11.37%. The wgt. % TOC data shows an average value of 0.12% across all sections, but has 5 data points significantly higher than the others.

Gas Bench

The 25 samples with $CaCO_3$ values between 0 and 20% (± 2%) were measured on the Gasbench, producing $\delta^{13}C_{carb}$ and $\delta^{18}O_{carb}$ data. The samples ran well within precision on standards of s-$\delta^{13}C$ = 0.1 ‰ and s-δ18O = 0.15‰; average values for the data set were -3.3% for $\delta^{13}C_{carb}$ and -7.9% for $\delta^{18}O_{carb}$. The distribution of the $\delta^{13}C$ values over the stratigraphic series can be seen in Figure 3, plotted with the corresponding stratigraphic sections linked to each sample run for $\delta^{13}C$. The overall average trend of $\delta^{13}C$ values is -0.1525x – 1.2448, showing that as the samples get younger, the values become lower on average. There are four major negative excursions with samples TC-07-05, SH-07-04, IS-07-04, and MD-19-08, with MD-19-08 being the lowest, at a

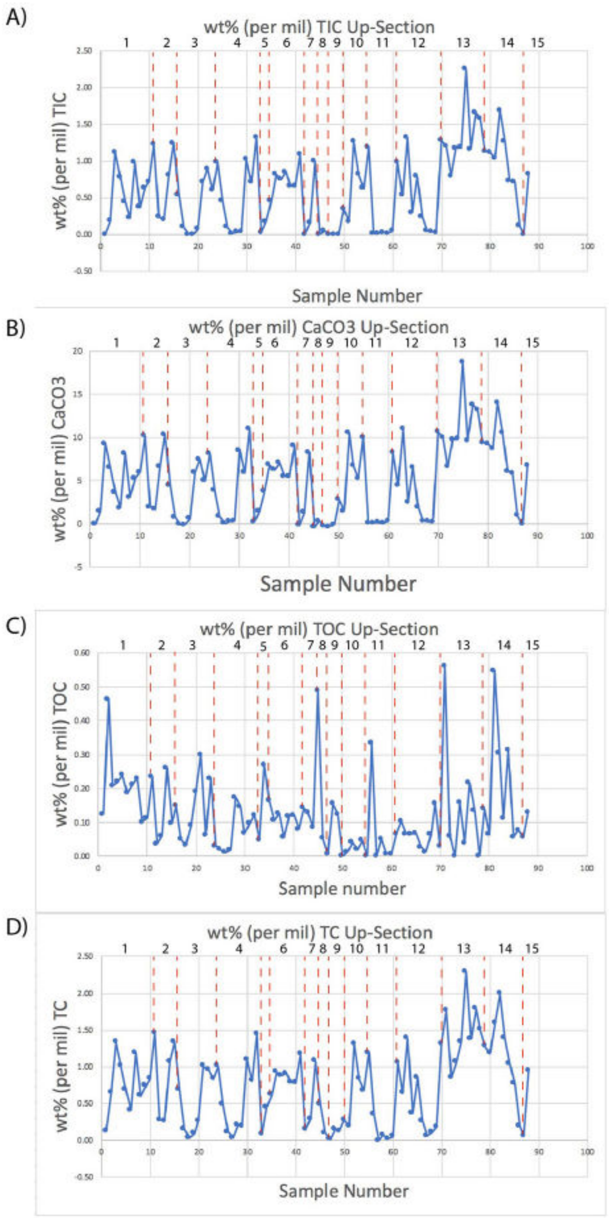

Figure 4. Total Inorganic Carbon (TIC), Calcium Carbonate (CaCO3), and Total Organic Carbon (TOC) and Total Carbon (TC) for each site with A) wgt. % TIC; B) wgt. % CaCO3; C) wgt. % TOC, and D) wgt. % TC. Numbers at top of each plot correspond to a stratigraphic section from the field, defined by the red-dashed margin: 1 = TC-01, 2 = MD-02, 3 = MD-09, 4) = SH-07, 5 = MF-08, 6 = KS-04, 7 = KS-01, 8 = MD-04, 9 = RG-03, 10 = SH-01, 11 = MF-07, 12 = ER-04, 13 = MD-19, 14 = IS-07, 15 = MF-05.

δ^{13}C value of -7.9‰. As all the samples from the whole dataset could not be run due to their low CaCO$_3$ content, the only complete stratigraphic section that could be analyzed was the MD-19 section. This interval shows a high degree of variability in terms δ^{13}C values, and the trend is negative up-section. The highest value in the section is -1.1‰ δ^{13}C and the lowest value is -7.9‰ δ^{13}C.

DISCUSSION

The goal of this project is to provide a chronostratigraphic framework for the fossil samples collected from the Fort Union and Willwood Formations. As seen in Figure 3, the trend in δ^{13}C becomes lower further up-section, suggesting a significant negative excursion part-way through the MD-19 section. This shift towards lower values is similar to that shown by δ^{13}C$_{carb}$ analysis done by Baczynski et al. (2013) and Koch et al. (2003), coinciding with the overall transition between the Fort Union Formation and the Willwood Formation. Since sampled sections begin in the Fort Union Fm., down-section of where the PETM δ^{13}C excursion and Fort Union-Willwood contact occurs, I interpret the negative shift to mark the transition between the two formations, agreeing with the studies of Baczynski et al. (2013) and Koch et al. (2003). The PETM appears to occur in section MD-19 when the isotopic record trends to the most negative values among the collected samples.

There is a marked difference between the δ^{13}C values presented by Baczynski et al. (2013) and those measured in this study. Their values average between -14 to -16‰ δ^{13}C$_{carb}$ whereas the most negative value for the bulk δ^{13}C$_{carb}$ recorded here is -7.9‰, indicating that there may have been multiple sources of carbonate present in the bulk samples. Baczynski et al. (2013) drilled samples from carbonate nodules using a Dremel tool on a polished section face in order to avoid secondary diagenetic spar. Thus, the very light δ^{13}C values measured in their study reflect authigenic carbonate. Since there were not enough carbonate nodules distributed through the sampled section used in this study to allow a continuous series for isotopic analysis, bulk sample was the only option. The bulk samples likely include carbonate phases with more isotopically enriched carbon. Further analysis of this difference and subsequent interpretations can be pursued after collection of δ^{13}Corg data.

CONCLUSION

Upon examination of the stable isotope data, the δ^{13}C values presented through the geochemical analysis of Paleogene-age sediments for the Bighorn Basin show the negative $\delta^{13}C$ excursion near the PETM and Fort Union-Willwood Formational contact. These results suggest that the PETM occurs within section MD-19. This suggests that if dwarfism occurs in *Coryphodon* in association with PETM climate changes, it should manifest in specimens from sections MD-19 and IS-07. The geochemical data described herein help constrain the chronology of the collected *Coryphodon* samples, thus contributing to the study of effects of Paleogene hyperthermals on dwarfism within mammalian fauna. This work will provide further evidence on the physical and morphological effects that a warming climate may have on mammals. Analogous to the PETM, anthropogenic activities over the past century are driving a rapid increase in of atmospheric CO_2 levels and a significant rise in global temperature. Continued study of the PETM will surely contribute to growing understanding of the effects of rapid warming on mammalian taxa.

ACKNOWLEDGMENTS

This research is financially supported by the Keck Geology Consortium and the National Science Foundation under Grant No.1659322, as well as Northwestern Weinberg College of Arts and Sciences Summer Research Grant. Thanks to my research advisors, Michael D'Emic, Simone Hoffmann, Brady Foreman, and Matthew Hurtgen, as well as fellow Keck researchers, Emily Randall, Danika Mayback, Grant Bowers, Richard Gonzalez, and Michael Ford, and my lab managers Grace Schellinger and Andrew Masterson.

REFERENCES

Abels, H.A., Clyde, W.C., Gingerich, P.D., Hilgen, F.J., Fricke, H.C., Bowen, G.J., and Lourens, L.J. (2012) Terrestrial carbon isotope excursions and biotic change during Palaeogene hyperthermals. Nature Geoscience, 5, 326–329.

Baczynski, A. A., Mcinerney, F. A., Wing, S. L., Kraus, M. J. (2013) Chemostratigraphic Implications of spatial variation in the Paleocene-Eocene Thermal Maximum carbon isotope excursion, SE Bighorn Basin, Wyoming. Geochemistry. Geophysics. Geosystems, 14, 4133–4152.

Barnosky, A.D., Hadly, E.A., Gonzalez, P., Head, J., Polly, P.D., Lawing, A.M. et al. (2017) Merging paleobiology with conservation biology to guide the future of terrestrial ecosystems. Science, 355, eaah4787.

D'Ambrosia, A.R., Clyde, W.C., Fricke, P.D. Gingerich, and Abels, H.A. (2017) Repetitive mammalian dwarfing during ancient greenhouse warming events. Science Advances, 3, e1601430.

Engleman, E. E., Jackson, L. L., and Norton, D. R. (1985) Determination of carbonate carbon in geological materials by coulometric titration. Chemical Geology, 53, 125–128.

Gingerich, P.D. (2003) Mammalian responses to climate change at the Paleocene-Eocene boundary: Polecat Bench record in the northern Bighorn Basin, Wyoming. Geological Society of America Special Paper, 369, 463–478.

Koch, P. L., Clyde, W. C., Hepple, R. P., Fogel, M. L., Wing, S. L., Zachos, J. C. (2003) Carbon and oxygen isotope records from Paleosols spanning the Paleocene-Eocene boundary, Bighorn Basin, Wyoming. Geological Society of America Special Papers, 369, 49–64.

Palkovacs, E.P. (2003) Explaining adaptive shifts in body size on islands: A life history approach. Oikos, 103, 37–44.

Secord, R., Bloch, J.I., Chester, S.G.B., Boyer, D.M., Wood, A.R., Wing, S.L., Kraus, M.J.,McInerney, F.A., and Krigbaum, J. (2012) Evolution of the earliest horses driven by climate change in the Paleocene-Eocene Thermal Maximum. Science, 335, 959–962.

Zachos, J.C., Dickens, G.R., and Zeebe, R.E. (2008) An early Cenozoic perspective on greenhouse warming and carbon-cycle dynamics. Nature, 451, 279–283.

KECK Geology Consortium
Learning Science Through Research
Published by the Keck Geology Consortium

Short Contributions
Keck Geology Consortium
Volume 33
May 2020
doi: 10.18277/AKRSG.2020.33.13

USING MICROLITES AND BUBBLES IN OBSIDIAN TO ASSESS FACTORS GOVERNING ERUPTION OF RHYOLITIC MAGMA

KURT KNESEL, Trinity University

INTRODUCTION

Deciphering the factors governing eruption of silicic magma is a fundamental problem in volcanology. A general model has emerged relating eruptive style to the interplay between ascent rate and the efficiency and extent of volatile loss during magma transport from subvolcanic chambers (e.g., Gonnermann and Manga, 2007). Fast ascent is believed to inhibit volatile loss, leading to bubble crowding, volatile overpressure and ultimately explosive fragmentation; in contrast, slow magma ascent favors gas escape and lava extrusion. Rise-rate estimates for magmas of andesitic and dacitic compositions are broadly consistent with this model (Rutherford and Gardner, 2000). However, comparable data for rhyolite eruptions has until recently been sparse (Castro and Gardner, 2008; Castro and Dingwell, 2009; Pallister et al., 2013; Tuffen et al., 2013; Myers et al., 2018), and the complex feedback between magma properties and processes during ascent that dictates degassing and eruptive behavior is only beginning to be understood (Cassidy et al., 2018).

This project aims to build a microtextural and chemical foundation from which to investigate conditions and processes governing eruption of rhyolitic magma. As a start, we focus on the effusive endmember, though we also consider explosively erupted products. Our textural analysis involves quantification of the size, shape, and orientation of microlites and bubbles in obsidian. In addition to providing insight into decompression-induced volatile loss and crystallization during magma ascent (e.g., Hammer and Rutherford, 2002; Toramaru, 2006; Cichy et al., 2011), microlite and bubble textures can be used to determine shear stresses and the type, magnitude, and rate of shear strain accumulated during magmatic flow (Manga, 1998; Castro et al., 2002; Rust et al., 2003; Rust and Cashman, 2007; Befus et al., 2014; 2015). We compliment these textural constraints by measuring the composition of phenocrysts and micro-phenocrysts to evaluate pre-eruptive conditions that influence magma ascent and emplacement.

The project kicked off with a visit to the spectacular Long Valley caldera in California to examine macro-scale flow structures on the well-preserved surfaces of young lava domes of the Inyo and Mono craters volcanic chains. Relocating to Trinity University in San Antonio, we then embarked on a 3D micro-textural and analytical study of flow-banded obsidian samples from heavily dissected and deeply exposed rhyolite lavas, pyroclastic deposits, and associated vent structures from the largest volcano in eastern Australia.

GEOLOGICAL BACKGROUND

Cenozoic volcanic rocks in Australia are almost entirely confined to the eastern edge of the continent (Fig. 1). This vast intraplate volcanic belt stretches some 3000 km from northern Queensland to Tasmania, and is mainly comprised of lava-field and central-volcano provinces (Wellman and McDougall, 1974). Although distinctions between the two province types are not always straightforward, the lava fields are commonly comprised of strongly undersaturated mafic lavas and show little to no age progression. In contrast, the central volcanoes consist mainly of mildly undersaturated to saturated mafic lavas with associated

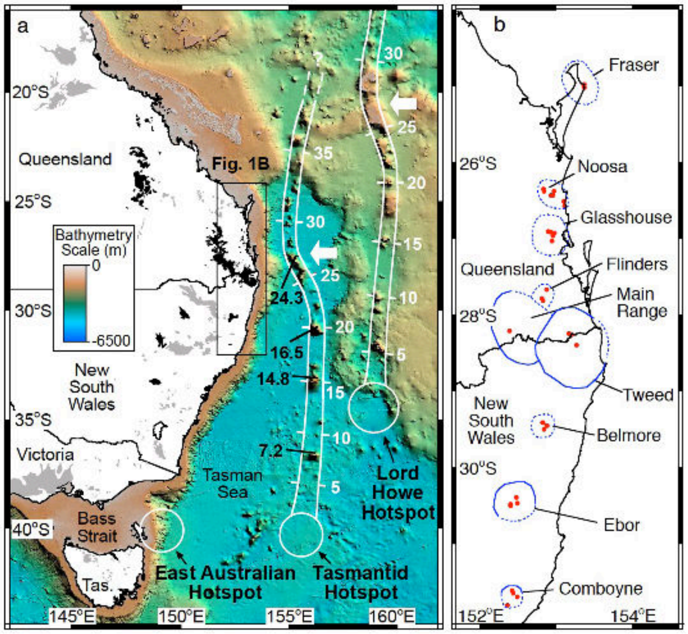

Figure 1. Distribution of Cenozoic volcanism on the Australian Plate, after Knesel et al. (2008). a, Central volcanoes are shaded black; mafic lava fields are grey; seamount tracks are outlined in white. White circles show predicted present-day hotspot locations. 40Ar/39Ar ages for Tasmantid seamounts from McDougall and Duncan (1988) are shown in black to the left of the chain; calculated ages are shown in white to the right of the two tracks at 5 Ma intervals. b, Locations of silicic rocks dated by 40Ar/39Ar geochronology (shown in red) from the central volcanoes (outlined in blue and dashed where approximate), including the Binna Burra Rhyolite, Tweed volcano).

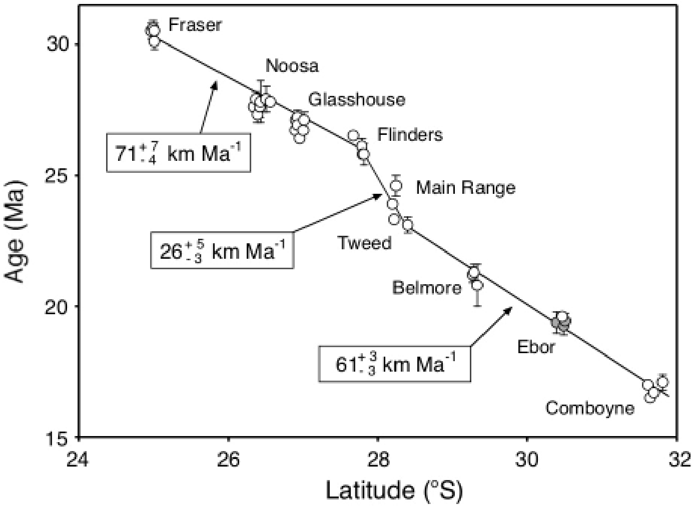

Figure 2. 40Ar/39Ar ages for silicic volcanic rocks from east Australian central volcanoes versus latitude, showing abrupt change in volcanic migration rate between 26-23 Ma, after Knesel et al. (2008). Ages for the Fraser, Noosa, Glasshouse, and Flinders areas are from Cohen et al. (2007); three (grey-filled symbols) of the four ages from Ebor volcano are from Ashley et al. (1995); all other ages for the Main Range, Tweed, Belmore, Ebor, and Comboyne volcanoes are from Knesel et al. (2008). Regressions of the 31-26 Ma, 26-23Ma, and 23-16 Ma time windows yield estimates for the northward component of Australian plate motion, relative to a fixed hotspot reference frame, shown with 1σ uncertainties..

felsic lava flows and intrusions that young southward. The age-progressive central volcanoes, along with the seamount tracks to the east (Fig. 1), are interpreted to track the northward movement of the Australian plate (Fig. 2) over several mantle hotspots over the past 35 Ma (Wellman and McDougall, 1974; McDougall and Duncan, 1988; Johnson, 1989; Sutherland, 2003; Vasconcelos et al., 2008).

The largest of the central volcanoes, the Tweed (or Mount Warning) volcano, straddles the border between the states of Queensland and New South Wales (Fig. 1). The Tweed volcano constitutes the eroded remnants of a former volcanic shield some 100 km in diameter (Fig. 3). River and stream incision has removed much of the northeastern flank and central region of the volcano, forming an erosional caldera some 30 km in diameter (Solomon, 1964). The volcano grew during a brief period of slow northward motion of the Australian Plate between ~26-23 Ma (Fig. 2) that has been linked to the onset of collision with the largest of the world's oceanic plateaus, the Ontong Java Plateau (Knesel et al., 2008). In addition to fueling the voluminous mafic volcanism, the longer time spent over the hotspot during the period of slow plate motion appears to have facilitated greater interaction between mafic magma and continental crust. The occurrence of silicic volcanism during this time window is anomalously high (Ewart et al., 1985), and includes rhyolite formations with isotopic signatures indicative of a predominantly crustal origin (Ewart, 1982).

An overview of the Tweed shield volcano (Fig. 3) is given in Ewart et al. (1987). The petrology and geochemistry of the volcanic succession comprising the northern flank of the volcano was examined by Ewart et al. (1977) and Ewart (1982). The stratigraphy of the southern flank of the volcano is presented in Duggan and Mason (1978) and a detailed evaluation of the petrogenesis was untaken by Duggan (1974). The generalized volcanic succession comprises an early mafic succession followed by rhyolitic lavas and tuffs that are in turn overlain by a younger mafic sequence. Two of the rhyolites – the Binna Burra and the Nimbin Rhyolites – are examined in this project.

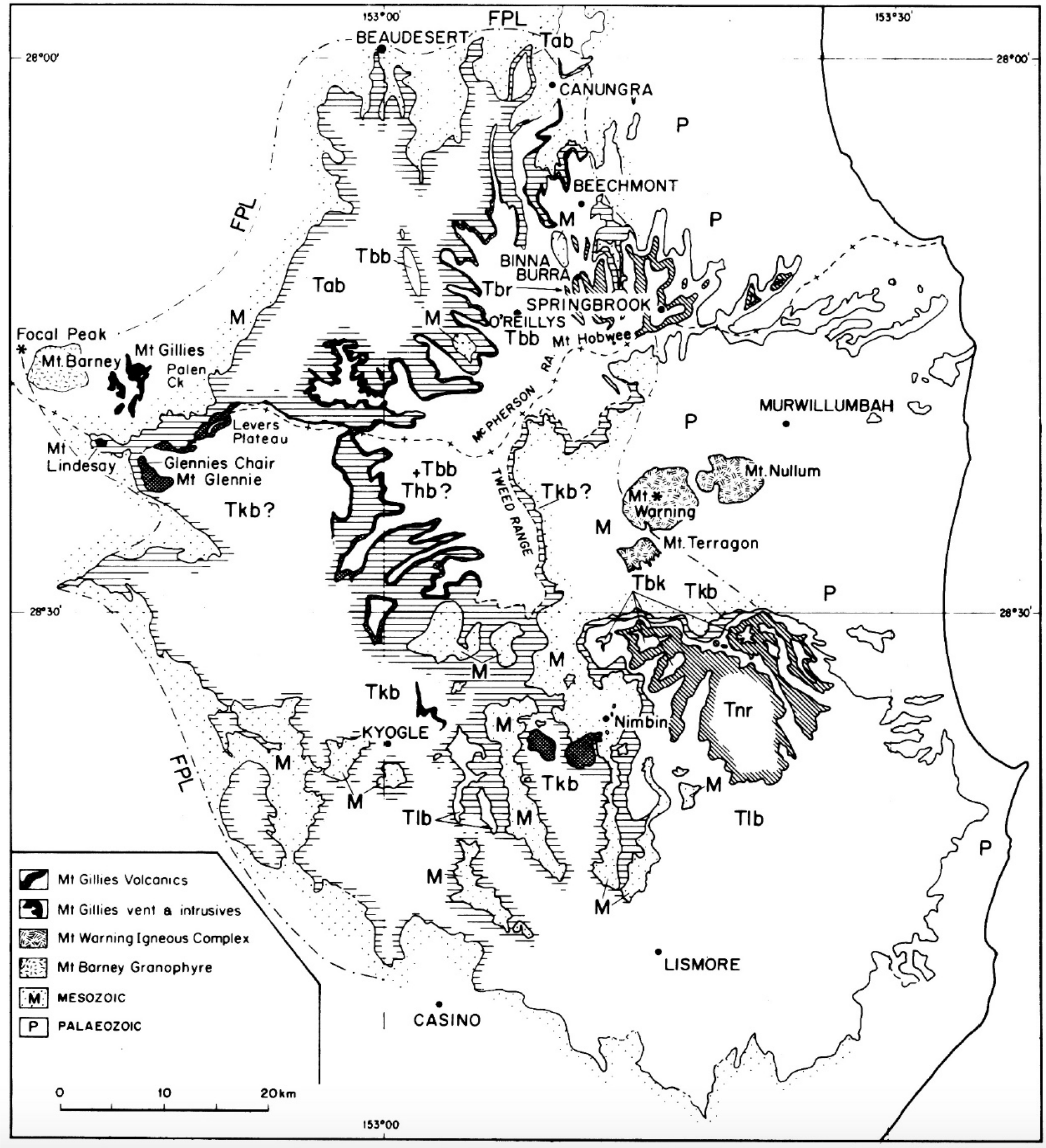

Figure 3. Geological map showing distribution of volcanic formations of the Tweed shield volcano, after Ewart et al. (1987). The volcanic succession consists of an early mafic sequence (Beechmont & Lismore Basalts) followed by rhyolitic lavas and tuffs (Binna Burra, Springbrook and Nimbin Rhyolites) that are overlain by a younger mafic sequence (Hobwee & Blue Knob Basalts). Basalts are shown in horizontally lined fields, while rhyolites are shown in diagonally lined fields. FPL: possible former limit of older basaltic lavas of the Focal Peak shield volcano (Albert & Kyogle Basalts). Thb: Hobwee Basalt, Tbk: Blue Knob Basalt, Tbr: Binna Burra and Springbrook Rhyolites, Tnr: Nimbin Rhyolite, Tbb: Beechmont Basalt, T1b: Lismore Basalt, Tab: Albert Basalt, Tkb: Kyogal Basalt, M: Mesozoic, P: Paleozoic.

The Nimbin Rhyolite is a complex of coalescing rhyolite lava domes and flows, along with minor pyroclastic deposits, erupted on the southern flank of the Tweed volcano (Fig. 3). The dome complex covers an area of roughly 400 km2 and reaches a maximum thickness of about 500 m. Individual lavas vary in thickness from 50 to 150 m and range from nearly aphyric to moderately porphyritic (10-30 vol. % crystals) flow-banded rhyolite, containing phenocrysts and micro-phenocrysts of quartz, sanidine, plagioclase, orthopyroxene, and minor clinopyroxene and ilmenite. Although extensive river and stream erosion have exposed the internal architecture of the domes and flows, dense vegetation limits access to most rock exposures. One voluminous lava flow defining the southern-most extent of the lava field, the Minyon Falls Rhyolite (Smith and Houston, 1995), affords excellent exposure of the basal obsidian, as well as the overlying crystalline core of the rhyolite, and was examined as part of all four student projects developed in this study.

The Binna Burra Rhyolite consists of at least five lava flows up to 100 m thick, with pyroclastic rocks at the base and near the top of the sequence, and includes a variety of plugs and dikes (Ewart et al., 1987). The pyroclastic rocks are predominantly fall deposits ranging from 20 to 120 m in thickness, but include at least one ash-flow tuff and boulder agglomerate. The rhyolite is biotite-bearing and thus is distinct from the rhyolite of the Nimbin dome complex. Sanidine from the Binna Burra Rhyolite yields an 40Ar/39Ar age of 23.9±0.2 Ma (Knesel et al., 2008). The conspicuous presence of volumetrically significant pyroclastic deposits, along with exposed vent structures, facilitated study of conditions and processes operating during shallow ascent of rhyolitic magma feeding both effusive and explosive activity.

STUDENT PROJECTS

Four students completed projects and submitted abstracts to the North Central GSA meeting in Duluth, MN (May, 2020). Summaries of their projects are presented below.

Chloe Campo (Trinity University) evaluated the influence of pre-eruptive magma temperature on the emplacement of rhyolite lava (Campo and Knesel, 2020). The chemical compositions of feldspars and pyroxenes were measured by scanning electron microscopy and were utilized, along with complimentary electron microprobe data, to calculate crystallization temperatures using the two-feldspar and two-pyroxene formulations described by Putirka (2008). Both thermometers indicate that micro-phenocrystic and groundmass minerals grew at pre-eruptive temperatures approximately 100ºC hotter than their phenocrystic counterparts and point to a late-stage thermal event driven by introduction of hot, mafic magma.

We then set out to establish whether the invading magma mixed with the rhyolite or simply transferred heat to it. Chemical analyses of colorless and brown-colored glassy flow bands within the rhyolite reveal that the bands are compositionally indistinguishable and, thus, are not likely the result of mixing of compositionally distinct magmas. This finding is consistent with analysis of microlite size and number densities indicating that flow banding in the rhyolite arose from degassing-related textural heterogeneities developed during shallow magma ascent (Seitzinger and Knesel, 2020; Seitzinger, this volume).

Chloe next explored the impact that pre-eruptive heating may have on the flow of lava. She discovered that the observed increase in temperature of about 100°C can produce a decrease in viscosity of roughly two orders of magnitude, and that this dramatic reduction may lead to a nearly 70% increase in the distance rhyolitic lava flows at the surface. Therefore, it appears that heating attendant with mafic recharge may not only trigger eruptions, it may also aid emplacement of highly degassed, aerially extensive silicic lava, without appealing to anomalously high eruption rates.

Brooke Dykstra (University of Illinois at Urbana-Champaign) investigated strain localization during emplacement of the Minyon Falls Rhyolite by examining the 3-dimensional orientation of acicular microlites in samples from the glassy base of the lava at near-vent and flow-front positions (Dykstra, Seitzinger and Knesel, 2020). The project benefitted from the dataset developed by Zenja Seitzinger in her study of microlite size and number densities (summarized below); Brooke's measurements expanded the stratigraphic coverage of the near-vent site. Orientation distributions were characterized by the standard deviation (σ) of microlite trend (ϕ) and plunge (θ). Preliminary analysis reveals little to no systematic variation of microlite alignment with microlite size or with stratigraphic or lateral position within the basal shear zone. Samples with the greatest and least degree of alignment are within about 0.5 m of each other, and alignment varies by up to a factor of 4 among individual flow bands within a single thin section.

The orientations of microlites and flow bands around rotated phenocrysts indicate that strain in the basal obsidian was dominated by simple shear, although a component of pure shear is likely in some bands. Comparison of the measured microlite orientations to theoretically predicted distributions of slender rods in a Newtonian fluid in simple shear flow (Manga, 1998) yields strains ranging from 2 up to 10 in both near-vent and flow-front positions. Overall, the strain estimates are high compared to those estimated for obsidian samples collected near the upper surfaces of other rhyolite domes (Castro et al, 2002; Befus et al., 2014; 2015). This observation is consistent with structural analysis (Smith, 1996) and numerical results (Befus et al., 2015) indicating that most of the strain associated with emplacement of viscous rhyolite lava is accommodated within a basal zone of shear, while the main mass of lava is rafted above.

Juliana Flint (State University of New York, Plattsburg) assessed flow conditions of both explosively and effusively erupted rhyolite by measuring the shapes and orientations of deformed bubbles in obsidian samples from pyroclastic deposits and an exposed vent of the Binna Burra Rhyolite, as well as obsidian from the Minyon Falls Rhyolite (Flint and Knesel, 2020). The approach takes advantage of the fact that bubble deformation in a highly viscous, low Reynolds number fluid, such as rhyolitic magma, is governed by the competing shear stress that deform the bubble and the surface-tension stresses that minimize interfacial area (Rust and Manga, 2002; Rust et al., 2003). The ratio of these stresses is the capillary number, Ca. The relationships between Ca and the shape and orientation of bubbles were used to evaluate the type and magnitude of shear stress associated magma flow.

Bubble orientations in all samples are indicative of predominantly simple shear, although minor components of pure shear, bubble-bubble interactions, and bubble relaxation appear to have also influenced bubble shape and orientation in some instances. Bubble deformation is modest in the obsidian lava, yielding shear stresses of a few kPa. In contrast, bubble geometries in obsidian clasts from pyroclastic flow and fall units record the greatest deformation with shear stresses up to 90 kPa. Bubbles in samples from the dissected vent, thought to be associated with a boulder tuff (agglomerate), yield intermediate shear stresses of a few 10s of kPa. The observed increase in shear stress recorded in the lava, fountain-fed agglomerate, and pyroclastic flow and fall units is consistent with the general model in which eruption style is governed by ascent rate.

Zenja Seitzinger (State University of New York, Geneseo) investigated the timing and location of microlite and flow-band formation during effusive emplacement of rhyolite (Seitzinger and Knesel, 2020). The size, orientation, and number density of clinopyroxene microlites were measured in the basal obsidian from the Minyon Falls Rhyolite. The obsidian contains dark bands of microlite-poor brown glass and light bands of microlite-rich colorless glass. Textural measurements were made for up to nine individual bands within individual thin-section for samples collected from flow-front and near-vent locations.

Band thickness ranges from 45 microns to 6 mm and microlite number densities (MND) range from about 108 to 109 cm-3. Most of this range is present at the scale of a single thin section. Bands with higher MND have smaller average crystal sizes and steeper (negative) slopes on crystal sized distribution (CSD) plots, compared to bands with lower microlite number density. None of the microlite properties correlate with band thickness, degree of microlite preferred orientation, or position within the basal shear zone. This observation led Zenja to conclude that most microlites were apparently unable to nucleate or grow appreciably during flow on the surface and that the microlite-defined flow bands formed during magma ascent. Therefore, while microlite preferred orientations within the basal shear zone register measurable re-orientation during emplacement (Dykstra, Seitzinger and Knesel, 2020), microlite number densities and size distributions reflect conduit processes. Given that number densities and size distributions of microlites vary on the scale of a thin-section, individual flow bands appear to record spatially complex variations in ascent rate, extent and/or depth of degassing, and residence time during transport in shallow volcanic conduits.

ACKNOWLEDGEMENTS

This material is based upon work supported by the Keck Geology Consortium and the National Science Foundation under Grant No. 1659322. We are grateful to Annie Barrett, Carol Blanchette and Chris Orr at the Valentine Eastern Sierra Reserves in Mammoth Lakes, CA, who provided us with an incredible experience at the Valentine Camp while in the field. This project benefitted greatly from the field work and exploratory research conducted by Anna Brown, Shari Cook, and Drew Luck at the University of Queensland.

REFERENCES

Ashley, P.M., Duncan, R.A., and Feebrey, C.A. (1995) Ebor Volcano and Crescent Complex, northeastern New South Wales: age and geological development. Australian Journal of Earth Science 42, 471-480.

Befus, K.S., Zinke, R.W., Jordan, J.S., Manga, M., and Gardner, J.E. (2014) Pre-eruptive storage conditions and eruption dynamics of a small rhyolite dome: Douglas Knob, Yellowstone volcanic field, USA. Bulletin of Volcanology 76, 1-12.

Befus, K.S., Manga, M., Gardner, J.E., and Williams, M. (2015) Ascent and emplacement dynamics of obsidian lavas inferred from microlite textures. Bulletin of Volcanology 77, 1-17.

Campo, C., and Knesel, K. (2020) Pre-eruptive temperatures and eruption dynamics of rhyolite lava, Nimbin Rhyolite dome complex, eastern Australia. Geological Society of America Abstracts with Programs 52, No. 5, doi: 10.1130/abs/2020NC-348134.

Cassidy, M., Manga, M., Cashman, K., and Bachman, O. (2018) Controls on explosive-effusive volcanic eruption styles: Nature Communications 9, 2839.

Castro, J., Manga, M., and Cashman, K. (2002) Dynamics of obsidian flows inferred from microstructures: insights from microlite preferred orientations. Earth and Planetary Science Letters 302, 38-50.

Castro, J.M., and Gardner, J.E. (2008) Did magma ascent rate control the explosive-effusive transition at the Inyo volcanic chain, California? Geology 36, 279-282.

Castro, J.M., and Dingwell, D.B. (2009) Rapid ascent of rhyolite magma at Chaiten volcano, Chile. Nature 461, 780-784.

Cichy, S.B., Botcharnikov, R.E., Holtz, F., and Behrens, H. (2011) Vesiculation and microlite crystallization induced by decompression: a case study of the 1991-1995 Mt Unzen eruption (Japan). Journal Petrology 52, 1469-1492.

Cohen, B.E., Vasconcelos, P.M., and Knesel, K.M. (2007) 40Ar/39Ar constraints on the timing of Oligocene intraplate volcanism in southeast Queensland. Australian Journal of Earth Science 54, 105-125.

Duggan, M.B. (1974) The mineralogy and petrology of the southern portion of the Tweed Shield Volcano, northeastern New South Wales, Unpubl. Ph.D. Thesis, Univ. of New England.

Duggan, M.B., and Mason, D.R. (1978) Stratigraphy of the Lamington Volcanics in far northeastern New South Wales, Journal of the Geological Society of Australia 25, 65-73.

Dykstra, B., Seitzinger, Z., and Knesel, K. (2020) Microlite orientations and strain localization within the basal shear zone of a large rhyolite lava dome, Minyon Falls, Australia. Geological Society of America. Abstracts with Programs 52, No. 5, doi: 10.1130/abs/2020NC-348339.

Ewart, A., Oversby, V.M., and Mateen, A. (1977) Petrology and Isotope Geochemistry of Tertiary Lavas from the Northern Flank of the Tweed Volcano, Southeastern Queensland, Journal of Petrology 18, 73-113.

Ewart, A. (1982) Petrogenesis of the Tertiary anorogenic volcanic series of southern Queensland, Australia, in light of trace element geochemistry and O, Sr, and Pb isotopes, Journal of Petrology 23, 344-382.

Ewart, A., Chappell, B.W., and Le Maitre, R.W. (1985) Aspects of the mineralogy and chemistry of the intermediate-silicic Cainozoic volcanic rocks of eastern Australia. Part 1: introduction and geochemistry, Australian Journal of Earth Science 32, 359-382.

Ewart, A., Stevens, N.C., and Ross, J.A. (1987) The Tweed and Focal Peak shield volcanoes, southeastern Queensland and northeast New South Wales, Pap. Dep. Geol. Univ. Qd. 11 (4), 1-82.

Flint, J., and Knesel, K. (2020) Bubble shapes and orientations in obsidian lavas, pyroclasts, and vents of the Tweed shield volcano, eastern Australia. Geological Society of America Abstracts with Programs 52, No. 5, doi: 10.1130/abs/2020NC-348341.

Gonnermann, H.M., and Manga, M. (2007) The fluid mechanics inside a volcano. Annual Review of Fluid Mechanics 39, 321-356.

Hammer, J.E., and Rutherford, M.J. (2002) An experimental study of the kinetics of decompression-induced crystallization in silicic melt: Journal of Geophysical Research, v. 107, doi: 10.1029/2001JB000281.

Johnson, R.W. (1989) Intraplate volcanism in Eastern Australia and New Zealand, 408 p.

Knesel K.M., Cohen B.E., Vasconcelos P.M., and Thiede D.S. (2008) Rapid change in drift of the Australian plate records collision with Ontong Java Plateau, Nature 454, 754-757.

Manga, M. (1998) Orientation distribution of microlites in obsidian. Journal of Volcanology and Geothermal Research 86, 107-115.

McDougall, I., and Duncan, R.A. (1988) Age progressive volcanism in the Tasmantid Seamounts. Earth and Planetary Science Letters 89, 207-220.

Myers, M.L., Wallace, P.J., Wilson, C.J.N., Watkins, J.M., and Liu, Y. (2018) Ascent rates of rhyolitic magma at the onset of three caldera-forming eruptions. American Mineralogist 103, 952-965.

Pallister, J.S., Diefenbach, A.K., Burton, W.C., Munoz, J., Griswold, J.P., Lara, L.E., Lowenstern, J.B., and Valenzuela, C.E. (2013) The Chaiten rhyolite lava dome: Eruption sequence, lava dome volumes, rapid effusion rates and source of the rhyolite magma. Andean Geology 40, 277-294.

Putirka, Keith D. (2008) Thermometers and Barometers for Volcanic Systems: Reviews in Mineralogy and Geochemistry 69, 61-120.

Rust, A.C., and Manga, M. (2002) Bubble shapes and orientations in low Re simple shear flow. Journal of Colloid and Interface Science 249, 476-480.

Rust, A.C., Manga, M., and Cashman, K.V. (2003) Determining flow type, shear rate and shear stress in magmas from bubble shapes and orientations. Journal of Volcanology and Geothermal Research 122, 111-132,

Rust, A.C., and Cashman, K.V. (2007) Multiple origins of obsidian pyroclasts and implications for changes in the dynamics of the 1300 B.P. eruption of Newberry Volcano, USA. Bulletin of Volcanology 69, 825-845.

Rutherford, M.J., and Gardner, J.E. (2000) Rates of magma ascent. In Encyclopedia of Volcanoes (Ed. Sigurdsson, H.) 207-217.

Seitzinger, Z., and Knesel, K. (2020) Flow bands and microlite textures in obsidian, Minyon Falls Rhyolite, Australia. Geological Society of America Abstracts with Programs 52, No. 5, doi: 10.1130/abs/2020NC-348340.

Smith, J.V., and Houston, E.C. (1995) Structure of lava flows of the Nimbin Rhyolite, northeast New South Wales: Australian Journal of Earth Sciences 42, 69-74.

Smith, J.V. (1996) Ductile-brittle transition structures in the basal shear zone of a rhyolite lava flow, eastern Australia: Journal of Volcanology and Geothermal Research. 72, 217-223.

Solomon, P.J. (1964) The Mount Warning Shield Volcano: a general geological and geomorphological study of the dissected shield, Pap. Dep. Geol. Univ. Qd. 5 (10), 1-12.

Sutherland, F.L. (2003) ‘Boomerang’ migratory intraplate Cenozoic volcanism, eastern Australian rift margins and the Indian-Pacific mantle boundary, Geological Society of Australia Special Publication 22 & Geological Society of America Special Paper 372, 203-221.

Toramaru, A. (2006) BND (bubble number density) decompression rate meter for explosive eruptions. Journal of Volcanology and Geothermal Research 154, 303-316.

Tuffen, H., James, M.R., Castro, J.M., and Schipper, C.I. (2013) Exceptional mobility of an advancing rhyolitic obsidian flow at Cordón Caulle volcano in Chile. Nature Communications 4, 2709.

Vasconcelos, P.M. Knesel, K.M., Cohen, B.C., and Heim, J.A. (2008) Geochronology of the Australian Cenozoic: a history of tectonic and igneous activity, weathering, erosion, and sedimentation, Australian Journal of Earth Science 55, 865-914.

Wellman, P., and McDougall, I. (1974) Cainozoic igneous activity in eastern Australia, Tectonophysics 23, 49-65.

KECK Geology Consortium
Learning Science Through Research
Published by the Keck Geology Consortium
Short Contributions
Keck Geology Consortium
Volume 33
May 2020
doi: 10.18277/AKRSG.2020.33.15

MICROLITE ORIENTATIONS AND STRAIN LOCALIZATION WITHIN THE BASAL SHEAR ZONE OF A LARGE RHYOLITIC LAVA, MINYON FALLS, AUSTRALIA

BROOKE DYKSTRA, University of Illinois at Urbana-Champaign
Research Advisor: Patricia Gregg

INTRODUCTION

The Minyon Falls Rhyolite is a large lava dome in the southern part of the Nimbin Rhyolite dome complex of the Tweed shield volcano in eastern Australia that was emplaced during the Early Miocene. In excess of 100 m thick and 4 km in diameter, the lava dome is comprised of a flow-banded obsidian overlain by banded crystalline rhyolite (Smith and Houston, 1994; Smith, 1996). Folds in the main mass of crystalline rhyolite record strains of <1 associated with gravity spreading during emplacement (Smith and Houston, 1994). In contrast, structures and textures of the basal obsidian indicate accommodation of large strains associated with shear roughly parallel to the base of the flow (Smith, 1996). To investigate the localization of strain within the basal shear zone, we consider the three-dimensional orientations of microlites within stratigraphically constrained samples of flow-banded obsidian from flow-front and near-vent localities. Because the degree to which microlites align during flow increases with increasing deformation, microlite orientation distributions can be used to infer flow properties such as flow type and strain (Manga, 1998; Castro et al., 2002).

METHODS

Theoretical Framework

When melt ascends through a shallow conduit, decompression and degassing result in the nucleation and growth of bubbles and microlites (Swanson et al., 1989; Toramaru, 2006). Variation in the concentration of microlites and/or bubbles often define a foliation common to silicic lavas referred to as flow banding (Manga, 2005). The textural characteristics and geometry of flow bands reflect the cumulative history of magmatic flow within the vent and at the surface. Here we take advantage of an integrated approach developed by Manga (1998) to gain quantitative insight into processes that occur during effusion of lava. Microlite orientations are measured in oriented thin-sections and are described by their trend (φ) and plunge (θ) as depicted in Figure 1. Comparison of measured distributions with those predicted by theory allows assessment of the type and magnitude of strain during flow.

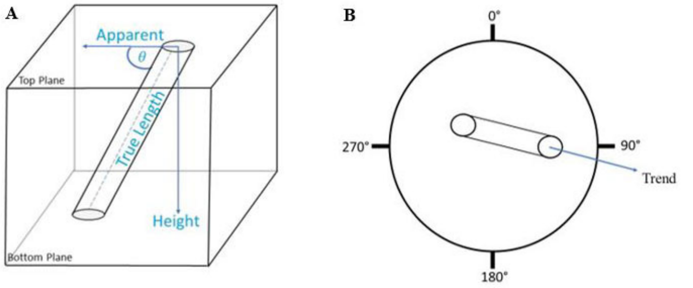

Figure 1. Schematic diagram illustrating characterization of microlite orientation through trend (φ) and plunge (θ), adapted from Castro et al. (2002). A: 3D schematic of a microlite between two focal planes. The apparent length measured from the top plane, moving down to the bottom plane to gain the height allows for the plunge (θ) to be calculated. The true length is then derived from the Pythagorean Theorem. B: Goniometer is utilized to determine the trend of the microlite based on its long axis.

The approach is underpinned by theoretical analysis of the motion of rigid rod-shape particles in dilute low-Reynolds-number shear flows (Manga, 1998). The equations for particle motion in simple shear flow are (Jeffery, 1992):

$$\frac{d\varphi}{dt} = \frac{G}{R^2+1}(R^2 \cos\varphi + sin^2(\varphi) \qquad \text{and}$$

$$\frac{d\theta}{dt} = G\frac{R^2-1}{R^2+1} sin\theta cos\theta sin\varphi cos\varphi,$$

while the equations for particle motion in pure shear flow are (Gray, 1966):

$$\frac{d\varphi}{dt} = G\frac{R^2-1}{R^2+1}\sin(2\varphi) \quad \text{and}$$

$$\frac{d\theta}{dt} = -\frac{1}{2}\frac{R^2-1}{R^2+1}\cos(2\varphi)\sin(2\theta)$$

where t is time (s), R is microlite aspect ratio, and G is strain rate (s^{-1}). The resulting three-dimensional orientation distributions can be conveniently characterized by the standard deviation (σ) of trend (φ) and plunge (θ). Using the equations given above, Manga (1998) showed that initially randomly oriented microlites in a simple shear flow progressively align in the direction of shear with increasing strain, but never perfectly align due to periodic rotation. In contrast microlites in a pure shear flow become perfectly aligned with increasing strain in the direction of extension. Therefore σ_φ and σ_θ approach zero in pure shear, and finite constants in simple shear flows (Manga, 1998).

Sample Background and Microlite Measurements

The obsidian samples examined here were collected from within the basal shear zone of the Minyon Falls Rhyolite (Brown, 2010; Cook, 2011). The structural and textural features of the glassy base and overlying crystalline core of the rhyolite are documented by Smith (1996) and Smith and Houston (1995), respectively. The base of the flow is comprised of a breccia overlain by coherent, flow-banded obsidian. Within 500 m of the inferred vent, the glassy base of the lava is roughly 3 m thick, but is in excess of 20 m near the southern front of the flow, some 4 km from the vent. The intact, banded obsidian records intense ductile shearing in multiple folds, rotated phenocrysts, alignment of microlites, and micro-folding of microlite-defined flow bands. In the lower part of the basal obsidian, flow bands are often discontinuous and are cut by mesoscale and microscale faults at low angles. The underlying basal breccia is comprised of monolithic clasts that are variably plastically deformed, with strong alignment of elongated clasts at distal locations. The clasts also show internal ductile textures (e.g., flow banding, micro-folds, etc.) similar to that in the coherent obsidian above. Near the vent where the breccia is thin (~0.5m thick) and in the top meter of the breccia in distal sites, clasts are angular to sub-rounded with distinct margins. However, with increasing distance below the intact obsidian at distal locations, clasts become rounded and elongate, with less distinct boundaries. Clasts range in size from 15 cm down to microscopic fragments that are indistinguishable from the glassy matrix in the field.

Detailed analysis of the spatial relationships of the brittle and ductile structures outlined above led Smith (1996) to conclude that: (1) the breccia formed by shear-induced fragmentation at the base of the flow, rather than as an overridden surface breccia; and (2) the basal shear zone accommodated most of the deformation during emplacement, while the main mass of lava was translated above. To investigate how strain is distributed within the basal zone of shear, we examined microlite orientations from two locations within the glassy base of Minyon Falls Rhyolite. The first site, referred to as the near-vent site with sample numbers beginning with MR11, is located roughly 0.5 km northeast of the inferred vent and includes four stratigraphically controlled samples of the intact obsidian and one sample of a sub-rounded clast from the underlying breccia. The second site is located at the southernmost extent of the lava, about 4 km from the vent area. This site is referred to as the flow-front site and is represented by three samples beginning with MR02.2. These three samples are within the zone of the basal breccia showing brittle-ductile transition structures (Smith, 1996).

All thin-sections were cut perpendicular to layering defined by flow bands with the original sample orientation in mind, where the "up" direction is parallel with the greater length of the slide (Fig. 2). The stratigraphic order of the banded MR11 thin-sections are reflected as 9 at the top, 7, 6T, 6B (all within the intact obsidian), and sample 2 at the bottom, within the basal breccia; the MR02 thin sections are ordered from sample 2 at the top, 3 in the middle, and 4 at the stratigraphic bottom (Brown, 2010; Cook, 2011). The method employed to measure microlite

Figure 2. Scan of thin-section MR11.7, showing microlite measurement sites (asterisks) for colorless and brown-colored flow bands along a vertical transect parallel to the stratigraphic "up" position of the oriented rock sample.

orientations is depicted in Figure 1 and described in Seitzinger (this volume). The method is similar to the simplified approach of Befus et al. (2014), which was adapted from the digital reconstruction method of Manga (1998). Because of space limitations, the details of the method are not repeated here.

The micro-textural analysis conducted here takes advantage of the large microlite orientation dataset developed by Seitzinger (this volume), who concentrated on quantification and interpretation of microlite size and number densities with the rhyolite. To expand the stratigraphic coverage, additional analyses were undertaken as part of this project for sample MR11.9, which is representative of the upper half of the intact obsidian at the near-vent site. All other data was collected by Seitzinger (this volume). With each thin-section, data was collected for up to nine individual flow bands along a roughly vertical transect relative to the "up" direction of the slide (Fig. 2). Microlite orientation distributions were measured for 33 flow bands at the near-vent site and 15 flow bands at the flow-front site.

RESULTS

Microlite Orientations

The orientation distributions of microlites are characterized by the standard deviation (σ) of trend (φ) and plunge (θ), with uncertainties of about 1° and 5° respectively (Manga, 1998; Befus et al., 2014). Due to inherent better resolution, we focus our attention here on measured trend distributions. Results for stratigraphically controlled samples at the flow-front and near-vent locations are shown in Figure 3.

The largest number of microlite measurements are from the near-vent site, where the majority of flow bands display a high degree of a microlite alignment ($\sigma_{\phi} < 20°$). The exception is sample MR11.7, which is characterized by less-well aligned microlites with σ_{ϕ} values ranging from 24° up to 38°. Microlites are also well alignment at the flow front, although there is no apparent improvement in alignment despite flowing roughly 4 km from the vent. The mean values for σ_{ϕ} are statistically indistinguishable between both sites (Fig. 3).

Despite the overall high degree of a microlite alignment within the basal shear zone, orientation distributions vary by up to a factor of four among flow bands within individual thin-sections (e.g., MR11.6B). This small-scale heterogeneity does not correlate with flow-band type, as defined by glass color and microlite

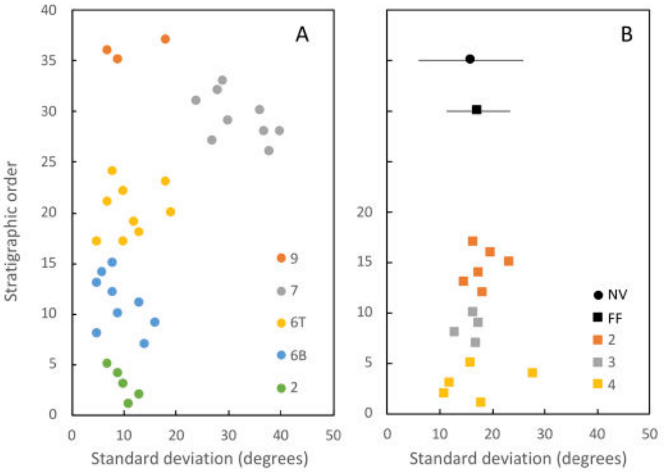

Figure 3. Variation of standard deviation of microlite trend angles (x-axis) with relative stratigraphic height (y-axis) for near-vent, A, and flow-front, B, locations. Mean values for the near-vent and flow-front sites are labeled NV and FF, respectively, and are shown at the top of panel B.

number density. Mean σ_ϕ values for all colorless and brown-colored flow bands analyzed are statistically indistinguishable (15±10° and 17±10°, respectively), and the goodness of fit, as expressed by R^2, for MND plotted against σ_ϕ (not shown) is less than 0.01 (MND data from Seitzinger, this volume).

Strain Estimates

The orientations of microlites and flow bands around rotated phenocrysts indicate that strain in the basal obsidian was primarily accumulated by simple shear (Fig. 4). Comparison of the measured microlite orientations to theoretically predicted distributions of slender rods in a Newtonian fluid in simple shear flow (Manga, 1998) yields strains ranging from 2 up to about 10 for most flow bands in both near-vent and flow-front positions. However, about a third of the flow bands yield standard deviations for trend angles that indicate infinite strain, assuming flow by simple shear alone. These low σ_ϕ values (down to 5°) appear to require a component of pure shear (e.g., Befus et al., 2014). Assuming pure shear alone, our σ_ϕ values indicate shear strains of up to about 3 (Manga, 1998). It seems likely that most of the microlite distributions reflect re-alignment in some combination of pure and simple shear flow. In any event, these strain estimates are high compared to those obtained for surface samples elsewhere (Castro et al., 2002; Befus et al., 2014; 2015).

DISCUSSION & CONCLUSIONS

Preliminary analysis reveals little to no systematic variation of microlite trend alignment with stratigraphic or lateral position within the basal shear zone of the Minyon Falls Rhyolite. With few exceptions, microlites are well aligned within the intact flow-banded obsidian and the underlying basal breccia. The degree of alignment is noticeably high compared to microlite orientation distributions measured for samples representative of the upper surfaces of rhyolite lava flows and domes (Befus et al., 2014; 2015). The high degree of microlite alignment at the base of the flow is consistent with numerical results indicating that most of the strain associated with emplacement of viscous rhyolite lava is accommodated within a basal zone of shear, while the main mass of lava is rafted above (Befus et al., 2015).

Figure 4. Photomicrographs showing deformation of flow bands around micro-phenocrysts, consistent with simple shear (from sample MR11.9).

Although the shapes of flow bands deformed by phenocrysts are consistent with simple shear (Fig. 4), some flow bands display microlites of too well alignment to have experienced simple shear alone. The apparent combination of pure and simple shear hinders an attempt to uniquely constrain the strain responsible for microlite alignment. Nevertheless, our measured orientation distributions for both flow-front and near-vent sites yield similar mean strain estimates (approaching 2 and 6 for pure and simple shear, respectively) for each site, based on mean values for the standard deviation of trend angles (Fig. 3).

A lack of improvement of microlite orientation with distance from the vent (Fig. 3) has been observed for surface samples from both small and large rhyolite lavas (Befus et al., 2014; 2015). One explanation for this lack of increased alignment with distance traveled on the surface is that microlite alignment is inherited from flow in the conduit and that flow at the surface was unable to further align microlites (Befus et al., 2014; 2015). This scenario seems likely for the upper portions of flows, where folds indicate strains less than 1 (Smith and Houston, 1994), but it is unlikely to apply to the base of rhyolite lava flows and domes where most of the strain associated with emplacement is expected to be concentrated. Although basal shear appears to be capable of improving the alignment of microlites from that potentially imparted in the conduit, it does not systematically increase microlite alignment with distance travel during subaerial flow. This observation is consistent with a model whereby the zone of basal shear migrates upward into the overlying lava as the flow advances (Smith, 1996).

ACKNOWLEDGEMENTS

This material is based upon work supported by the Keck Geology Consortium and the National Science Foundation under Grant No. 1659322.

REFERENCES

Befus, K.S., Zinke, R.W., Jordan, J.S., Manga, M., and Gardner, J.E., 2014, Pre-eruptive storage conditions and eruption dynamics of a small rhyolite dome: Douglas Knob, Yellowstone volcanic field, USA. Bulletin of Volcanology 76, 1-12.

Befus, K.S., Manga, M., Gardner, J.E., and Williams, M., 2015, Ascent and emplacement dynamics of obsidian lavas inferred from microlite textures. Bulletin of Volcanology 77, 1-17.

Brown, A., 2010, Flow dynamics, strain history and structural evolution of the basal shear zone of silicic lava, Minyon Falls Rhyolite, New South Wales, Australia. Unpublished Honors Thesis, University of Queensland, p. 53.

Castro, J., Manga, M., and Cashman, K., 2002, Dynamics of obsidian flows inferred from microstructures: insights from microlite preferred orientations: Earth and Planetary Science Letters 199, 211-226.

Cook, 2011, Ascent and emplacement history of silicic lava inferred from microlite and bubble shapes and orientations Minyon Falls Rhyolite, New South Wales, Australia, Unpublished Honors Thesis, University of Queensland, p. 250.

Manga, M., 1998, Orientation distribution of microlites in obsidian. Journal of Volcanology and Geothermal Research 86, 107-115.

Manga, M., 2005, Deformation of flow bands by bubbles and crystals. Geological Society of America Special Paper 396, 47-53.

Smith, J.V., and Houston, E.C., 1995, Structure of lava flows of the Nimbin Rhyolite, northeast New South Wales: Australian Journal of Earth Sciences 42, 69-74.

Smith, J.V., 1996, Ductile-brittle transition structures in the basal shear zone of a rhyolite lava flow, eastern Australia: Journal of Volcanology and Geothermal Research. 72, 217-223.

Swanson, S. E., Naney, M. T., Westrich, H. R., Eichelberger, J. C., 1989, Crystallization history of Obsidian Dome, Inyo Domes, California. Bulletin of Volcanology, 51, 161-176.

Toramaru, A., 2006, BND (bubble number density) decompression rate meter for explosive eruptions. Journal of Volcanology and Geothermal Research 154, 303-316.

Learning Science Through Research
Published by the Keck Geology Consortium
Short Contributions
Keck Geology Consortium
Volume 33
May 2020
doi: 10.18277/AKRSG.2020.33.16

FLOW BANDS AND MICROLITE TEXTURES IN OBSIDIAN, MINYON FALLS RHYOLITE, AUSTRALIA

ZENJA SEITZINGER, SUNY Geneseo
Research Advisor: Dori Farthing

INTRODUCTION

The Minyon Falls Rhyolite is a Miocene aged, 1.25 km^3 lava dome that was emplaced effusively during the late stages of volcanism of the basaltic Tweed shield volcano in eastern Australia (Smith and Houston, 1995). Extensive weathering and erosion have cut vertically through the lava dome, offering a unique exposure of the crystalline interior and glassy base of the rhyolite (Smith, 1996). Flow bands within the basal obsidian preserve structures and textures indicating accommodation of large shear strains during emplacement of the dome (Smith, 1966; Brown, 2010; Cook, 2011). This study aims to better understand the conduit processes and ascent history of magma that fed the Minyon Falls Rhyolite through a quantitative micro-textural investigation of individual flow bands from the basal shear zone.

Banding in the basal obsidian of the Minyon Falls Rhyolite is well-defined by variations in glass color and microlite concentrations (Fig. 1). Microlites are rod-shaped acicular crystals with lengths typically less than 50 microns that are found ubiquitously in obsidian lavas and pyroclastic obsidian (Ross, 1962). Volatile exsolution in ascending magma causes the liquidus temperatures to increase, creating large effective undercoolings that drive the nucleation and growth of microlites (Hammer and Rutherford, 2002). The study of the number density and size distributions of microlites can therefore provide insight into the dynamics and history of magma ascent in shallow conduits that ultimately feed eruptions of silicic magma (Cashman, 1988; Marsh, 1988; 1998; Castro et al., 2002; Toramaru et al., 2008; Befus et al., 2014).

METHODS

Obsidian samples were collected from the basal shear zone of the Minyon Falls Rhyolite at two localities. The first site is roughly 500 m N-NE of the inferred vent, hereafter referred to as the near vent site and denoted by sample numbers beginning with MR11. Sample MR11.2 was collected near the top of a 0.3 to 0.5-m thick basal breccia overlain by 2.5 m of flow-banded obsidian lava. Samples MR11.6 and MR11.7 were collected within the flow-banded obsidian at approximately 0.1 m and 1 m, respectively, from the contact with the basal breccia. The second site is

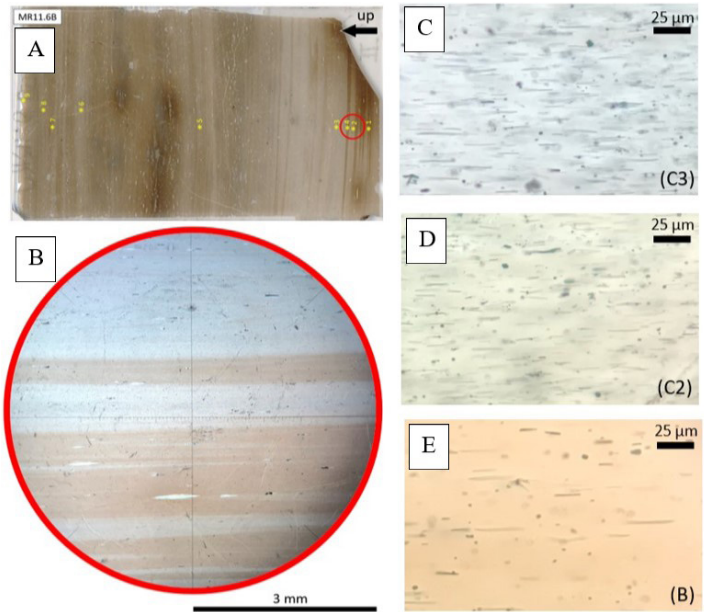

Figure 1. Flow banded obsidian from the Minyon Falls Rhyolite basal shear zone. (A) MR11.6T thin section; yellow stars indicate location of microlite collection sites red circle indicates location of B; up direction is indicated by arrow. (B) Flow banding in plain polarized light (ppl) (4x); (C) C3 band in ppl (40x); (D) C2 band in ppl (40x); (E) B band in ppl (40x).

located at the southern margin of the lava dome about 4 km from the inferred vent. Sample MR02 was collected within the basal breccia at the flow front, which contains deformed clasts elongated roughly parallel to the foliation of the overlying flow-banded obsidian. Microlites at both locations are primarily clinopyroxene (as determined by EDS analysis on the JEOL JSM-6010LA scanning electron microscope at Trinity University) and are generally aligned parallel to banding, except in the vicinity of sparse phenocrysts.

Micro-textural measurements were made for five thin sections; MR11 thin sections 2, 6B (bottom), 6T (top), and 7 represent the relative stratigraphic order from bottom to top respectively at the near vent site. A single thin section was analyzed from sample MR02 (section 9) from the flow front location. All thin sections were cut perpendicular to the flow foliation with the "up" direction parallel to the long edge of the slide (Brown, 2010; Cook, 2011). To establish criteria for selection of bands for quantitative petrographic analyses, a central vertical transect was marked on each thin section parallel to the sample's up direction. At a magnification of 20x, glass color, band thickness, and relative microlite content were determined for each band at the points it crossed the transect.

Microlite populations were characterized for four to nine individual bands for each thin section. Thickness and band type were considered when choosing collection sites in order to provide a data set representative of the entire thin section. A total of 3573 pyroxene microlites were measured within 37 separate collection sites (i.e. individual bands). Using the 40x objective on a petrographic microscope, the apparent length of each microlite within the variable sample volumes was measured with the calibrated scale within the ocular; microlite plunge depth was determined by focusing through the transparent glass onto either end of the microlite; and trend angle relative to the plane of banding was measured using the goniometer on the rotating stage (Castro et al., 2002). True length of each microlite was calculated with simple trigonometry using the apparent length and depth (Befus et al., 2014; 2015). Replicate analyses for ten pyroxene microlites of variable size and orientation measured ten separate times in a band of moderate MND yielded a standard deviation for true microlite length of ± 0.37 microns. Size and orientation measurements were taken for roughly 100 microlites in each collection site (i.e., band), with the sample volume scaled appropriately. Collection volumes varied between 3.75 x 10^4 and 9.26 x 105 μm^3. Microlite number densities were then determined for each band by dividing the number of microlites counted by the volume of the thin section imaged for that collection site.

RESULTS

Four band types were identified within the samples (Table 1): B, brown glass with low to moderate microlite concentrations; C1, cloudy, glass unsuitable for microlite data collection; C2, colorless glass with moderate microlite concentrations; and C3, colorless glass with high microlite concentrations. All band types were found in both the banded and brecciated zones. Bands of brown glass make up on average 14 ±10% of the analyzed samples, while bands of colorless glass, including both C2 and C3, make up on average 69 ±7%, and C1 bands make up 17 ±13%. Band thickness ranges from 0.045 mm to 6.5 mm and is independent of color, type, and stratigraphic position.

Pyroxene microlite number densities and sizes were measured for 14 brown (B) bands and 23 colorless (C) bands, of which 8 were C2 type and 15 were C3 type.

Table 1. Summary of all microlite results.

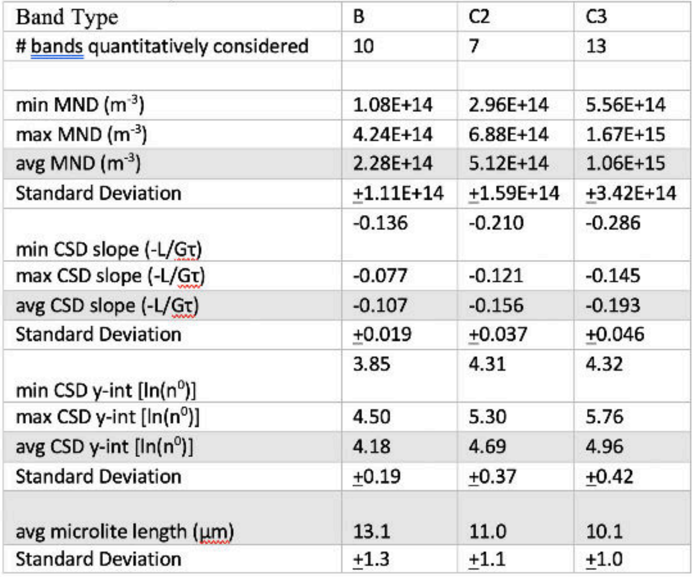

Band Type	B	C2	C3
# bands quantitatively considered	10	7	13
min MND (m^{-3})	1.08E+14	2.96E+14	5.56E+14
max MND (m^{-3})	4.24E+14	6.88E+14	1.67E+15
avg MND (m^{-3})	2.28E+14	5.12E+14	1.06E+15
Standard Deviation	±1.11E+14	±1.59E+14	±3.42E+14
min CSD slope (-L/Gτ)	-0.136	-0.210	-0.286
max CSD slope (-L/Gτ)	-0.077	-0.121	-0.145
avg CSD slope (-L/Gτ)	-0.107	-0.156	-0.193
Standard Deviation	±0.019	±0.037	±0.046
min CSD y-int [ln(n^0)]	3.85	4.31	4.32
max CSD y-int [ln(n^0)]	4.50	5.30	5.76
avg CSD y-int [ln(n^0)]	4.18	4.69	4.96
Standard Deviation	±0.19	±0.37	±0.42
avg microlite length (μm)	13.1	11.0	10.1
Standard Deviation	±1.3	±1.1	±1.0

This distribution of measurements broadly reflects the abundance of band types within the sample set. MND values range from 1.08 x 10^{14} m^{-3} to 1.67 x10^{15} m^{-3} which is approximately an order of magnitude difference. The ranges, averages, and standard deviations of the characteristic microlite populations for each band type are summarized in Table 1.

Crystal Size Distribution (CSD) plots constructed using 5-µm size bins generate log-linear trends with coefficient of determination (R2) values of 0.85 or greater for the majority of flow bands (Fig. 2). I focus my discussion below on these samples.

Although there is important overlap between the band types (Fig. 3), colorless bands have higher average MNDs, smaller average crystal lengths, steeper characteristic CSD slopes, and higher nucleation densities (derived from CSD intercepts) compared to brown bands (Table 1). When slope of CSDs for individual bands are plotted as a function of MND, a positive correlation is observed, and when CSD slope is plotted as a function of average microlite length, a negative correlation is observed (Fig. 3).

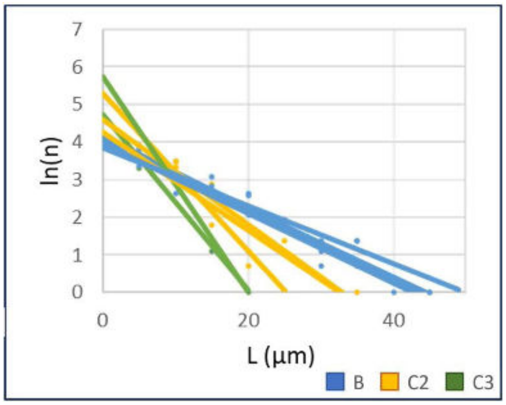

Figure 2. CSD-Fan of MR11.6T bands. Nine separate collection sites are represented here with each trendline color coded to their respective band type.

DISCUSSION

One of the objectives of this study is to assess the timing and location of microlite crystallization and their relation to band formation. Most of the range of microlite size distributions and number densities are observed at the scale of individual thin sections and are not correlated with stratigraphic height or with the degree of microlite alignment within the basal shear zone. These observations indicate that the majority of acicular pyroxene microlites crystallized during magma ascent in the conduit and do not appear to have been significantly modified by further nucleation or growth during emplacement at the surface. Given that the bands are defined in part by microlite concentrations and sizes, it is reasonable to conclude that the flow bands also formed in the conduit.

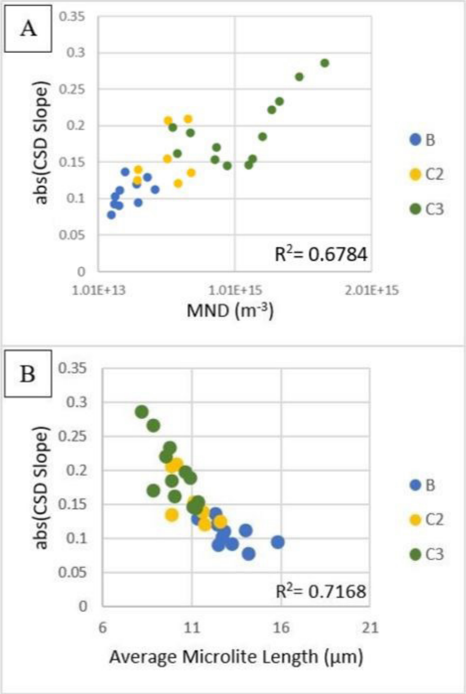

Figure 3. CSD-Fan of MR11.6T bands. Nine separate collection sites are represented here with each trendline color coded to their respective band type.

Micro-textural variability observed in flow-banded obsidian have been interpreted to reflect variations in ascent rate and residence time during magma transport in shallow volcanic conduits (Castro and Mercer, 2004). Whether high MND values correlates with fast or slow ascent may depend on magma composition. In general, volatile exsolution resulting from magma ascent induces a state of supersaturation ideal for microlite crystallization. A couple between degassing and crystallization may be appropriate for some andesite and dacitic magmas where MND appears to scale with magma ascent rate (Tormamaru et al., 2008). However, in rhyolitic magmas, the loss of volatiles may increase melt viscosity to a point where nucleation and growth of microlites are inhibited (Cassidy et al., 2018). In this scenario, microlites do not reflect the extent, or at least the rate, of degassing as they are kinetically prevented from doing so.

Castro and Mercer (2004) note that MND values for extensively degassed obsidian lavas have a wide range of MND, a range comparable to that reported here for the Minyon Falls Rhyolite. On the basis of kinetic consideration, they propose a model in which microlite variations are governed by the geometry of flow in the conduit. Magma ascent velocity is expected to decrease away from the center of the conduit because the conduit margins exert destructive frictional forces on the ascending melt (Fig. 4). Slow ascent closer to conduit walls allows more time for microlites to crystallize (i.e. higher MND), while faster ascent towards the center of the conduit limits the time for microlites to crystallize (i.e. low MND). However, if CSD slope is a function of growth time (Marsh, 1998), the positive correlation between CSD slope and MND observed here (Fig. 3) is inconsistent with a model based on kinetic limitations to crystallization in highly viscous rhyolitic magma. If so, flow bands with higher MND may in fact reflect faster ascent than bands with lower MND, similar to that proposed for some intermediate magmas.

Alternatively, flow bands may form through a process of repeated shear-related fragmentation and annealing of fragments during magma ascent in in shallow volcanic conduits (Gonnermann and Manga, 2003; 2005; Castro et al., 2005; Tuffen et al., 2003). An ascending melt that experiences excessive shear stress may cross a kinetic boundary shifting from fluid-like to solid-like behavior and fragment into clasts and ash; this process is known as shear-induced fragmentation. Textural heterogeneity, for example expressed as flow banding, may be achieved by repeated fragmentation events followed by melt relaxation and reorganization of internal structure (RFH). At the start of an RFH cycle, the brittle response to the excessive shear stress creates a fracture, resulting in a temporary zone of local decompression (Fig. 4). The localized zone of low pressure surrounding the fracture is expected to initiate volatile exsolution (Castro et al., 2005; Cabrera et al., 2011) and a high degree of undercooling, facilitating the abundant nucleation of microlites (Fig. 4). Bands with high MNDs, smaller average microlite lengths, and steeper CSD slopes (Fig. 3) may therefore be interpreted to have experienced greater degrees of undercooling, while bands with low MNDs, larger average microlite lengths, and shallower CSD slopes may have experienced lesser degrees of undercooling.

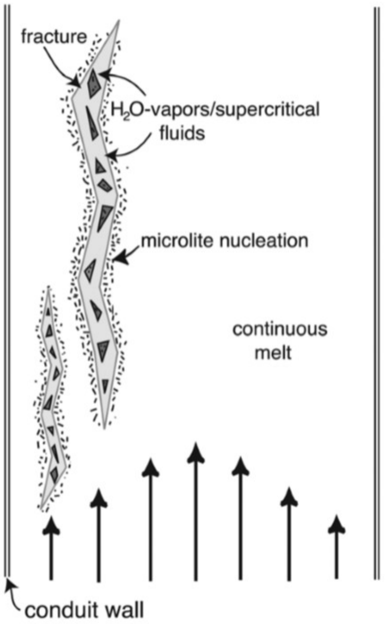

Figure 4. Schematic conduit cross section illustrating possible conduit processes during the ascent and eruption of silicic magma, including flow velocity profile (arrows) and shear-induced fragmentation (Castro et al., 2005).

Analysis of water content profiles transecting healed faults in pyroclastic obsidian revealed low water content along structures interpreted as fault suture zones and both abrupt and gradual increases in water content moving further away (Cabrera et al., 2011). These results raise the possibility that local zones within the ascending magma may experience individualized degassing histories in response to melt fracturing. If correct, the Minyon Falls microlite characteristics (Fig. 3), including the fan-like pattern of CSD trendlines within a single thin section (Fig. 2) may be interpreted to record variation in water exsolution and associated undercooling within proximity to shear-induced fractures (Fig. 4). The greatest MND and steepest CSD slopes may record zones of greater volatile exsolution closest to the fracture; the decrease in MND and CSD slope steepness may result from increasing distance away from the fracture.

Alternatively, the degassing and undercooling driving the microlite crystallization preserved in any flow band may be dependent on the depth of shear fragmentation. Melt fracturing at deeper levels in the conduit should induce lesser extents of degassing and smaller undercooling compared to fragmentation at shallower levels. If crystallization is in response to the sudden gas loss from the melt, lower effective undercooling at greater depth may then lead to lower MND and shallower CSD slopes. Continued ascent and fragmentation at shallower levels would lead to bands with higher MND and steeper CSD slopes.

In either case, as shear stresses relax following fragmentation, the melt reverts to fluid-like behavior and anneals the space created by the opened fracture (Tuffen et al. 2003). The brecciated magma surrounded by a microlite rich zone may deform plastically and elongate by the ascending forces. Repeated fragmentation events may create intermittent fracture networks that promote the permeable flow of exsolved volatiles to travel through and escape, resulting in an open system degassing mechanism that is consistent with effusive eruptions (Cabrera et al., 2011).

CONCLUSIONS

Based upon the microanalysis of flow bands within the basal shear zone of the Minyon Falls lava dome, the following conclusions can be made:

(1) The lack of any correlation between band thickness, glass color, MND, and microlite size and preferred orientation with stratigraphic height within the basal shear zone suggests that microlite-defined flow bands form during magma ascent.

(2) Colorless bands are characterized by high MNDs, smaller average microlite lengths, and steeper CSD slopes, while brown bands are characterized by low MNDs, larger average microlite lengths, and shallower CSD slopes.

(3) Given that number densities and size distributions of microlites vary widely on the scale of a thin section, individual flow bands are interpreted to provide a record of spatially complex variations in water exsolution rate and degree of undercooling during transport. The observed textural variations may be explained by variable ascent rate and/or repeated fragmentation and healing events (RFH) within the shallow volcanic conduit.

ACKNOWLEDGEMENTS

This material is based upon work supported by the Keck Geology Consortium and the National Science Foundation under Grant No. 1659322.

REFERENCES

Befus, K.S., Manga, M., Gardner, J.E., and Williams, M., 2015, Ascent and emplacement dynamics of obsidian lavas inferred from microlite textures: Bulletin of Volcanology, v. 77, p. 1-17, doi: 10.1007/s00445-015-0971-6.

Befus, K.S, Zinke, R.W., Jordan, J.S., Manga, M., and Gardner, J.E., 2014, Pre-eruptive storage conditions and eruption dynamics of a small rhyolite dome: Douglas Knob, Yellowstone volcanic field, USA: Bulletin of Volcanology, v. 76, p. 1-12, doi: 10.1007/s00445-014-0808-8.

Brown, A., 2010, Flow dynamics, strain history and structural evolution of the basal shear zone of silicic lava, Minyon Falls Rhyolite, New South Wales, Australia. Unpublished Honors Thesis, University of Queensland, p. 53.

Cabrera A., Weinberg, R.F., Wright, H.M.N., Zlotnik, S., and Cas, R.A.F., 2011, Melt fracturing and healing: a mechanism for degassing and origin of silicic obsidian: Geology, v. 39, p. 67-70, doi: 10.1130/G31355.1.

Cashman, K.V., 1988, Crystallization of Mount St. Helens 1980-1986 dacite: A quantitative textural approach: Bulletin of Volcanology, v. 50, p. 194-209.

Cassidy, M., Manga, M., Cashman, K., and Bachmann, O., 2018, Controls on explosive-effusive volcanic eruption styles: Nature Communications, doi: 10.1038/s41467-018-05293-3.

Castro, J.M., Dingwell, D.B., Nichols, A.R.L., and Gardner, J.E., 2005, New insights on the origin of flow bands in obsidian: Geological Society of America Special Paper 396, p. 55-65, doi: 10.1130/2005.2396(05).

Castro, J.M. and Mercer, C., 2004, Microlite textures and volatile contents of obsidian from the Inyo volcanic chain, California: Geophysical Research Letters, v. 3, doi:10.1029/2004GL020489.

Castro, J., Manga, M., and Cashman, K., 2002, Dynamics of obsidian flows inferred from microstructures: insights from microlite preferred orientations: Earth and Planetary Science Letters, v. 199, p. 211-226, doi: 10.1016/S0012-821X(02)00559-9.

Cook, S., 2011, Ascent and emplacement history of silicic lava inferred from microlite and bubble shapes and orientations Minyon Falls Rhyolite, New South Wales, Australia, Unpublished Honors Thesis, University of Queensland, p. 250.

Gonnermann, H.M., and Manga, M., 2003, Explosive volcanism may not be an inevitable consequence of magma fragmentation: Nature, v. 426, p. 432-435.

Gonnermann, H.M., and Manga, M., 2005, Flow banding in obsidian: A record of evolving textural heterogeneity during magma deformation: Earth and Planetary Science Letters, v. 236, p. 135-147, doi: 10.1016/j.epsl.2005.04.031.

Hammer, J.E. and Rutherford, M.J., 2002, An experimental study of the kinetics of decompression-induced crystallization in silicic melt: Journal of Geophysical Research, v. 107, doi: 10.1029/2001JB000281.

Marsh, B.D., 1988, Crystal Size Distribution (CSD) in rocks and the kinetics and dynamics of crystallization: Contributions to Mineralogy and Petrology, v. 99, p. 277-291.

Marsh, B.D., 1998, On the interpretation of crystal size distributions in magmatic systems: Journal of Petrology, v. 39, p. 553-599.

Ross, C.S., 1962, Microlites in glassy volcanic rocks: American Mineralogist, v. 47, p. 723-740.

Smith, J.V., 1996, Ductile-brittle transition structures in the basal shear zone of a rhyolite lava flow, eastern Australia: Journal of Volcanology and Geothermal Research, v. 72, p. 217-223, doi: 10.1016/0377-0273(96)00009-1.

Smith, J.V., and Houston, E.C., 1995, Structure of lava flows of the Nimbin Rhyolite, northeast New South Wales, Australian Journal of Earth Sciences, v. 42, p. 69-74.

Toramaru, A., Noguchi, S., Oyoshihara, S., and Tsune, A., 2008, MND (microlite number density) water exsolution rate meter: Journal of Volcanology and Geothermal Research, v. 175, p. 156-167, doi: 10.1016/j.jvolgeores.2008.03.035.

Tuffen, H., Dingwell, D.B., and Pinkerton, H., 2003, Repeated fracture and healing of silicic magma generate flow banding and earthquakes: Geology, v. 31, p. 1089-1092.

KECK Geology Consortium
Learning Science Through Research
Published by the Keck Geology Consortium
Short Contributions
Keck Geology Consortium
Volume 33
May 2020
doi: 10.18277/AKRSG.2020.33.17

THE IMPORTANCE OF GEOMORPHIC CONTROLS ON HYDRAULIC PROCESSES IN NORTHERN YELLOWSTONE NATIONAL PARK

LYMAN PERSICO, Whitman College

INTRODUCTION

The greater Yellowstone ecosystem is the largest mostly intact temperate-zone ecosystem in the world (Fig 1). Within Yellowstone, riparian corridors are key zones that provide abundant water and food resources. These corridors are particularly important in the relatively dry semiarid landscape of northern Yellowstone National Park, which is characterized by sagebrush, grasslands, and scattered conifer groves (Yellowstone National Park, 1997). In the early 20th century, many streams in northern Yellowstone hosted abundant beaver and their dams created extensive wetlands along valley floors (Fig. 2, Warren, 1926). Beaver and their dams have been largely absent from Yellowstone since the mid-20th century (Jonas, 1955). The causes of beaver extirpation and associated decline of riparian habitat is a topic of scientific intrigue (National Research Council, 2002; Yellowstone National Park, 1997). According to some, the loss of beaver is the direct result of competition with elk (Chadde and Kay, 1991). In the early 20th century, elk populations increased dramatically due to the extermination of wolves. The high numbers of elk over-browsed willow and aspen outcompeting beaver and degrading riparian habitat. This sequence of events is hypothesized to be part of a trophic cascade triggered by wolf removal. Using the trophic cascade framework, some have proposed that stream incision in northern Yellowstone caused an ecosystem state switch from beaver-willow to elk-grasslands during the latter half of the 20th century (Fig. 2).

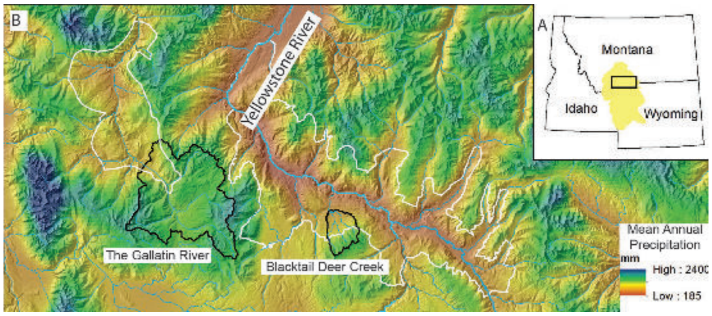

Figure 1. The Greater Yellowstone ecosystem spans across Wyoming, Idaho, and Montana (A). In northern Yellowstone (extent shown in A), low elevations are relatively dry (PRISM Climate Group, 2004) and limited snow pack creates winter foraging habitat for Elk (B). The Blacktail Deer Creek drainage basin (black line) is part of the winter range of the northern Yellowstone elk herd (white line). In Yellowstone National Park, the lower reaches of the Gallatin River drainage basin (black line) are part of the winter range of the Gallatin River elk herd (white line).

The transition from a dominantly riparian landscape to grasslands is attributed to the combined effects of the loss of beaver and intensive elk browsing that altered both the form and function of streams (Wolf et al., 2007). The loss of beaver dams increased channel gradients that triggered channel incision (Beschta and Ripple, 2018; Wolf et al., 2007). Incision disconnected channels from floodplains because high frequency flood events no longer were able to inundate floodplains. Additionally, incision effectively lowered water tables thus limiting willow and aspen recovery after wolf reintroduction (Marshall et al., 2013). The decreased riparian vegetation also caused channels to increase in width, further degrading riparian habitat (Beschta and Ripple, 2006; Chadde and Kay, 1991; Wolf et al., 2007). Regardless of changes to beaver populations and vegetation density, there are other factors that control stream dynamics and channel form.

River function and channel morphology are controlled by myriad of factors including hydraulic flow properties, bank material, subsurface conditions, and

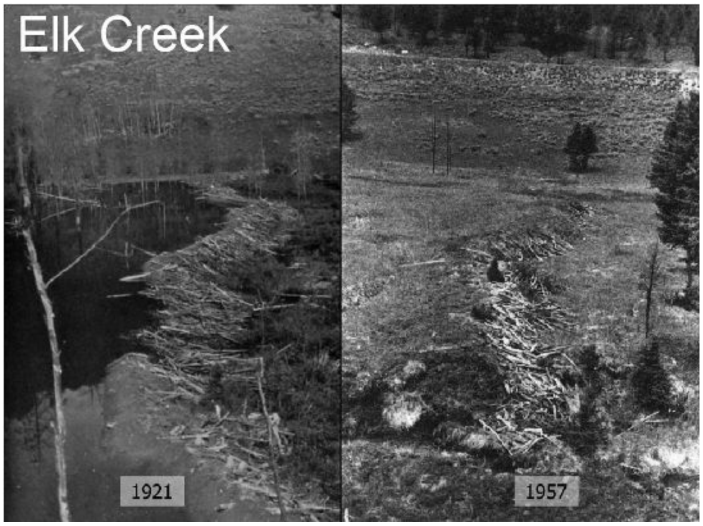

Figure 2. The Northern Range stream of Elk Creek contained many beaver dams in the 1920s that extended across much of the valley floor. Those beaver dams were abandoned by the 1950s and the stream has incised over 2 m from the top of the beaver bond sediments.

climatic variability (Knighton, 1998). For example, in Yellowstone, sediment size is an important control on channel morphology and the frequency of floodplain inundation (Meyer, 2001). And climate variability influences surficial processes throughout the entire drainage basin (Meyer et al., 1995). Climate change can alter forest fire frequency and severity and alter sediment loads delivered to channels (e.g. Legleiter et al., 2003; Meyer et al., 1992; Meyer et al., 1995). Climate variability can also influence ecologic function such as beaver activity (Persico and Meyer, 2012) and aspen regeneration (Romme et al., 1995). Morpho-stratigraphic evidence indicates that climate variability is significant control on the long-term history of channel dynamics and that some stream incision predates the historical period on many streams in northern Yellowstone (Meyer et al., 1995; Persico and Meyer, 2009).These factors must be accounted for when assessing how streams have responded to trophic cascade events in the 20th century.

In the summer of 2019, our five-student Keck research project focused on characterizing the hydraulic characteristics and Holocene fluvial history of two streams in Northern Yellowstone. Our goal was to document underlying geomorphic controls on stream function and history. This context is vital to assess how vegetation changes affected 20th century stream behavior. The field season began on Blacktail Deer Creek in north central Yellowstone (Fig. 3). The stream is part of the National Ecological Observatory Network (NEON) and has experienced willow resurgence in the past two decades (Beschta and Ripple, 2007; Marshall et al., 2013). We next travelled to the Gallatin River in western Yellowstone (Fig. 4). The Gallatin River contains riparian habitat that is both in and out of elk winter range (Brazda, 1952; Peek et al., 1967). We worked collectively in the field for three weeks to collect data sets that were used independently in each student project. Along each stream reach, we characterized channel, terrace and floodplain morphology by topographic survey using RTK GPS and a total station (Fig. 5A &B). We surveyed channel cross sections and channel/water surface long profiles with cm-scale accuracy. We also characterized channel bed material by pebble counts

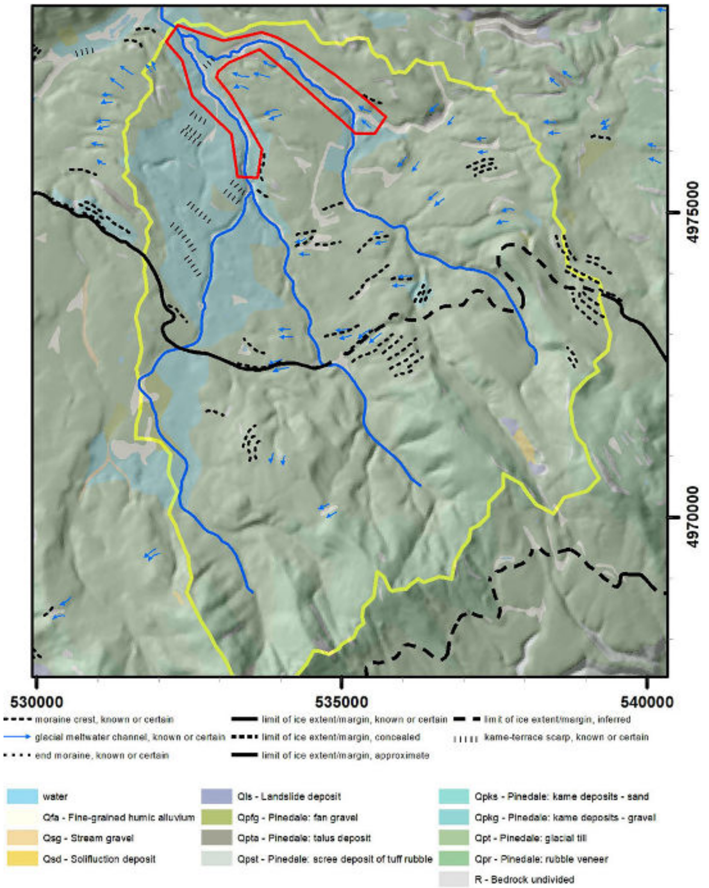

Figure 3. Blacktail Deer Creek drainage basin (yellow line) drains the northern flank of the Washburn Range. The range was entirely glaciated by the Yellowstone Ice Cap during the LGM (Pierce, 1979). The Blacktail Deer Creek drainage network is heavily influenced by meltwater channels (blue arrows) and kame deposits associated with the recission of the northern Yellowstone outlet glacier (Pierce, 1973a). Redline indicates the extent of the 2019 field season surveys.

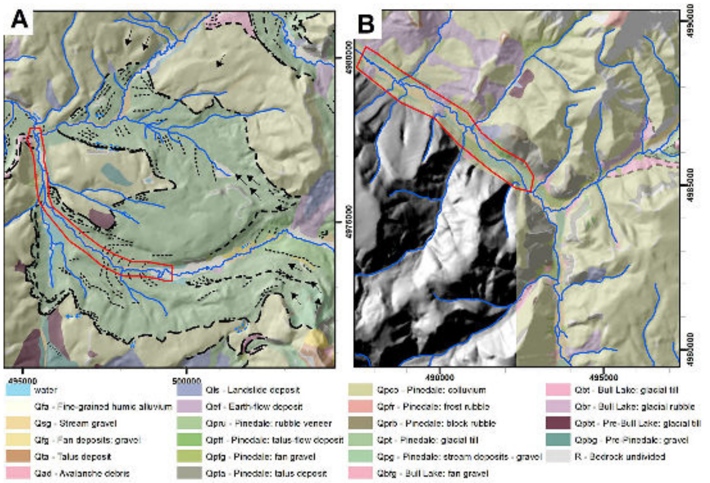

Figure 4. The Gallatin River drains the western flank of the Gallatin Range. The upper portions of the watershed were glaciated during the LGM (Pierce, 1973b) and the slope of the stream is controlled by recessional moraines (A, line symbology explained in Fig. 3). The lower reach of the river was not glaciated at the LGM and the valley floor contains glacial outwash and alluvial fan deposits (B). Redline indicates the extent of the 2019 field season surveys.

(Fig. 5C). We identified and mapped geomorphic surfaces on the valley floor including kame terraces, Holocene fluvial terraces, paleochannels, active floodplains and channels. We also described terrace deposit stratigraphy at selected locations and sampled for 14C. The 14C samples allow us to constrain the timing of channel aggradation and terrace formation. After field work, the team travelled back to Whitman College to digitize field observations, prepare samples for 14C analyses, and begin the process of creating a hydraulic flow models based on the topographic surveys.

STUDENT PROJECTS

Trent Foky (Whitman College) focused on the geomorphic history of Blacktail Deer Creek and created a surficial geologic map. Trent used field observations of geomorphic surfaces in conjunction with topographic surveys, high-resolution orthorectified aerial imagery, and 1-m lidar derived DEM (National Ecological Observatory Network, 2019) to map the extent of the different surfaces. The timing of terrace formation was constrained using 14C ages (see Chantal's project) and a volcanic ash that we identified in terrace stratigraphy. Trent also analyzed the nature of the geomorphic surfaces and characterized the slopes of the active channel relative to the terrace surfaces. Trent's work documents that most of the valley floor is a fill terrace that aggraded during the early and middle Holocene. The active channel and floodplain are confined to a narrowly incised corridor in this surface. This limits the total area of the valley floor that is influenced by 20th century riparian vegetation changes.

Alice Hinzmann (Carleton College) studied the hydraulic characteristics of the Gallatin River. She used four reference stream reaches to study how potential geomorphic and trophic cascade-related processes have influenced the flooding behavior of the river. She estimated the discharge for 2, 5, and 10-year recurrence interval floods using multiple regression of known gauge stations with basin area and elevation (Johnson and Parrett, 2004). Alice used the surveyed cross sections to create a hydraulic model using HEC-RAS software. With this model Alice predicted the size of flood necessary to inundate floodplain and terrace surfaces. Alice's modeling shows that floodplain surfaces are not inundated during high frequency low magnitude flood events, even sites that are outside of elk winter range. Additionally, some reach gradients are controlled by local base level constraints that produced channel that fill more frequently (Fig 5). Alice's results are important as

Figure 4. The 2019 Keck Yellowstone Research team surveyed channel geometry using RTK GPS and a total station. The upper reaches of the Gallatin River (A) are relatively low gradient because of local base level control set by recessional moraines (Fig. 3A). Overbank flooding occurs with higher frequency relative to the lower reaches where the river has incised into late Pleistocene outwash deposits (B). The research team characterized bed material using gravelometers and zig-zag pebble counts. Blacktail Deer Creek (C) aggraded during the early and middle Holocene and incised during the late Holocene prior to the historical period.

they highlight how deceptively simple concepts like floodplain, terrace, and bankfull recurrence interval and controlled by site-specific geomorphic characteristics related to the Quaternary geomorphic history of the drainage basin.

Chantal Iosso (Washington and Lee College) focused on advancing our understanding of the timing of fluvial depositional events on both Blacktail Deer Creek and the Gallatin River. Chantal identified exposed sections of terrace and floodplain deposits where she described the stratigraphy and soil morphology. She tediously picked though the exposed sediments looking for charcoal, twigs, or pinecones for 14C age analyses. Chantal cleaned the samples of modern organic material. Chantal calibrated the 14C ages and compared them to other records of fluvial processes in Yellowstone. Chantal also identified an ash in stratigraphy of the widespread terrace on the east fork of Blacktail Deer Creek. The ash was deposited during an eruption for Glacier Peak at 11.2 ka. Chantal also documented floodplain sediments that are inset within the widespread 1.5 m terrace that date to late Holocene. These dates combined with the geomorphic mapping indicate that the Blacktail Deer Creek aggraded during the early and middle Holocene and was followed by a period of late Holocene incision.

April Phinney (Wheaton College) focused on the hydraulic characteristics of the east and west forks of Blacktail Deer Creek. Similar to Alice's project, April estimated discharges at the ungauged study reaches using multiple regression analyses (Miller, 2003). April then produced a hydraulic model using surveyed topographic cross sections in HEC-RAS. April mapped inundation extent of various flood magnitudes on the high-resolution LiDAR-derived DEM (National Ecological Observatory Network, 2019). Both the east and west forks of Blacktail are in elk winter range and have experienced over-browsing of riparian vegetation in the 20th century and recent increase in willow. April's modeling indicates that despite these similarities, the east and west forks respond very differently to flooding. Along the west fork, even high magnitude (100-yr) floods are confined to a narrow incised channel. The east fork, however, has overbank flooding during low magnitude floods. These results indicate that geomorphic factors like basin area and stream power are important controls on the amount of flood plain inundation during flood events.

Eliza Van Wetter (Whitman College) explored historical changes to channel patterns and also analyzed the magnitude of discharges required to activate the channel bed material along Blacktail Deer Creek. Eliza compared high-altitude aerial imagery from the middle 20th century with recent high-resolution orthographic imagery using GIS. This analysis shows that streams have mostly remained stable during the past 60 years. The only differences are where there have been stream avulsions and creation of new channels and abandonment of older channels. Eliza's work helps to explain the various paleochannels that Trent mapped on both the east and west fork of Blacktail Deer Creek. Eliza determined the shear stresses required to initiate sediment movement in channels and compared that to shear stress during flood events that April estimated using HEC-RAS. These analyses indicate that even during large floods a significant portion of the bed material is immobile due to its large size. This large sediment is likely relict Pleistocene glacial outwash that underlies the Holocene stream deposits. This suggests that incision is limited by local base level control created by the underlying glacial sediments. This work is important to understanding the Holocene evolution of Blacktail Deer Creek and persistent controls of geomorphic history on modern process.

SUMMARY

Collectively, the five student projects provide a nuanced analysis of fluvial processes and geomorphic history of both Blacktail Deer Creek and the Gallatin River. The results of these analyses indicate that geomorphic history has persistent and widespread control on modern channel geometry and hydraulic processes. Along Blacktail Deer Creek, the valley floor aggraded during the early and middle Holocene and has incised in the late Holocene, prior to the historical period (Fig 5C). The magnitude of incision is controlled by local base level related to glacial deposits. Additionally, stream power is important because the larger west fork can effectively incise through fine-grained Holocene terrace deposits. Along the Gallatin River, channel stability and form are controlled by the extent and type of late Pleistocene deposits. The upper reaches are more stable due to limited ability to incise into recessional moraine deposits. The lower reaches are less stable as the river has incised into thick outwash gravels and alluvium during the Holocene.

ACKNOWLEDGEMENTS

This material is based upon work supported by the Keck Geology Consortium and the National Science Foundation under Grant No. 1659322. Further financial and laboratory support was provided by Whitman College. We thank Roy Renken, Annie Carlson and Beth Horton of the National Park Service for their support.

REFERENCES

Beschta, R. L., and Ripple, W. J., 2006, River channel dynamics following extirpation of wolves in northwestern Yellowstone National Park, USA: Earth Surface Processes and Landforms, v. 31, no. 12, p. 1525-1539.

Beschta, R. L., and Ripple, W. J., 2007, Increased willow heights along northern Yellowstone's Blacktail Deer Creek following wolf reintroduction: Western North American Naturalist, v. 67, no. 4, p. 613-617.

Beschta, R. L., and Ripple, W. J., 2018, Can large carnivores change streams via a trophic cascade?: Ecohydrology, v. 0, no. 0, p. e2048.

Brazda, A. R., 1952, Elk migration patterns, and some of the factors affecting movements in the Gallatin River drainage, Montana [M.S.: Montana State University.

Chadde, S. W., and Kay, C. E., 1991, Tall-willow communities on Yellowstone's Northern Range: A test of the "natural-regulation" paradigm, in Keiter, R. B., and Boyce, M. S., eds., The Greater Yellowstone Ecosystem: Binghamton, Yale University Press, p. 231-263.

Johnson, D. R., and Parrett, C., 2004, Methods for estimating flood frequency in Montana based on data through water year 1998: Water-Resources Investigations - U. S. Geological Survey.

Jonas, R. J., 1955, A population and ecological study of the beaver (Castor canadensis) of Yellowstone National ParkM.S.]: University of Idaho, 193 p.

Knighton, D., 1998, Fluvial Forms and Processes A New Perspective, New York, Oxford University Press.

Legleiter, C., Lawrence, R., Fonstad, M., Marcus, W., and Aspinall, R., 2003, Fluvial response a decade after wildfire in the northern Yellowstone ecosystem: a spatially explicit analysis: Geomorphology, v. 54, no. 3-4, p. 119-136.

Marshall, K. N., Hobbs, N. T., and Cooper, D. J., 2013, Stream hydrology limits recovery of riparian ecosystems after wolf reintroduction: Proceedings of the Royal Society B-Biological Sciences, v. 280, no. 1756.

Meyer, G. A., 2001, Recent large-magnitude floods and their impact on valley-floor environments of northeastern Yellowstone: Geomorphology, v. 40, no. 3-4, p. 271-290.

Meyer, G. A., Wells, S. G., Balling, R. C., and Jull, A. J. T., 1992, Response of alluvial systems to fire and climate change in Yellowstone-National-Park: Nature, v. 357, no. 6374, p. 147.

Meyer, G. A., Wells, S. G., and Jull, A. J. T., 1995, Fire and alluvial chronology in Yellowstone National Park: Climatic and intrinsic controls on Holocene geomorphic processes: Geological Society of America Bulletin, v. 107, no. 10, p. 1211-1230.

Miller, K. A., 2003, Peak-flow characteristics of Wyoming streams: Water-Resources Investigations - U. S. Geological Survey.

National Ecological Observatory Network, 2019, High-resolution orthorectified RGB camera imagery and mosaics, Elevation - Lidar: Provisional data downloaded from http://data.neonscience.org on 9/1/19., Batelle, Boulder, CO, USA.

National Research Council, 2002, Ecological Dynamics on Yellowstone's Northern Range, Washington DC, National Academy Press.

Peek, J. M., Lovaas, A. L., and Rouse, R. A., 1967, Population Changes within the Gallatin Elk Herd, 1932-1965: The Journal of Wildlife Management, v. 31, no. 2, p. 304-316.

Persico, L., and Meyer, G., 2009, Holocene beaver damming, fluvial geomorphology, and climate in Yellowstone National Park, Wyoming:

Quaternary Research, v. 71, no. 3, p. 340-353.

Persico, L., and Meyer, G., 2012, Natural and historical variability in fluvial processes, beaver activity, and climate in the Greater Yellowstone Ecosystem: Earth Surface Processes and Landforms, v. 38, no. 7, p. 728-750.

Pierce, K. L., 1973a, Surficial geologic map of Mammoth Quadrangle and part of the Gardiner Quadrangle, Yellowstone National Park, Wyoming and Montana: Miscellaneous Geologic Investigations Map.

Pierce, K. L., 1973b, Surficial geologic map of the Mount Holmes Quadrangle and parts of the Tepee Creek, Crown Butte, and Miner quadrangles, Yellowstone National Park, Wyoming and Montana: Miscellaneous Geologic Investigations Map.

Pierce, K. L., 1979, History and dynamics of glaciation in the northern Yellowstone National Park area, 729F.

PRISM Climate Group, O. S. U., 2004, 30-yr Normal Annual Precipitation: http://prism.oregonstate.edu.

Romme, W. H., Turner, M. G., Wallace, L. L., and Walker, J. S., 1995, Aspen, elk, and fire in northern Yellowstone National Park: Ecology, v. 76, no. 7, p. 2097-2106.

Warren, E. R., 1926, A study of the beaver in the Yancey region of Yellowstone National Park, Syracuse, Roosevelt Wildlife Annals 1.

Wolf, E. C., Cooper, D. J., and Hobbs, N. T., 2007, Hydrologic regime and herbivory stabilize an alternative state in Yellowstone National Park: Ecological Applications, v. 17, no. 6, p. 1572-1587.

Yellowstone National Park, 1997, Yellowstone's Northern Range: Complexity and Change in a Wildland Ecosystem, Mammoth Hot Springs, National Park Service, 148 p.

KECK Geology Consortium
Learning Science Through Research
Published by the Keck Geology Consortium
Short Contributions
Keck Geology Consortium
Volume 33
May 2020
doi: 10.18277/AKRSG.2020.33.18

UNRAVELING THE GEOMORPHIC HISTORY OF BLACKTAIL DEER CREEK

TRENT FOKY, Whitman College
Research Advisor: Lyman Persico

INTRODUCTION

Yellowstone National Park has been at the center of scientific inquiry since it first received federal protection in 1872. It has served as a research hotspot for both biologists and geologists alike. The surrounding region is known as the Greater Yellowstone Ecosystem and includes flora and fauna that interact in an ecosystem that is highly protected from the majority of outside anthropogenic effects. The absence of major anthropogenic impacts in greater Yellowstone has resulted in one of the largest intact temperate ecosystems in the world (Knight & Landres, 1998). From within the boundaries of Yellowstone, one of the most divisive ecological debates on the planet began: the effects that wolves have had on the greater Yellowstone ecosystem (National Research Council, 2002). Wolves were removed from the park in the 1920's and subsequently reintroduced from 1995 to 1997 (National Research Council, 2002). This loss and reintroduction of wolves provides a unique opportunity to observe the effects that top predators have on other organisms and fluvial systems. From this extirpation and reintroduction, the debate about how apex predators can influence an entire ecosystem began.

Trophic cascade theory states that changes to organisms in higher trophic levels have trickle-down effects on each lower trophic level. Yellowstone's wolves have become an example of the trophic cascade theory. The removal of wolves from the park in the 1920's, caused elk populations to increase due to the lack of apex predators. The increase in the total elk numbers or change in elk foraging behavior ("culture of fear") then increased herbivory on deciduous tree species, especially on elk winter grounds(Chadde & Kay, 1991). During winter, snow severely limits where elk can live, and they become confined into smaller areas: winter ranges. Some research suggests that within these elk winter ranges, there is increases in herbivores which leads to severe overgrazing of willows and aspens along riparian corridors (Ripple & Beschta, 2004). Overgrazing leads to less woody debris in streams and fewer plants anchoring the banks in place. The lack of wolves caused an increase in herbivory from elk, a loss of woody plants species, and therefore a lower hydraulic roughness. This change in hydraulic roughness thereby caused incision and widening of streams (Beschta & Ripple, 2006, 2018; Beschta & Ripple, 2018).

The goal of our research is to understand the geomorphic causes for changes in stream behavior and morphology of Blacktail Deer Creek. Our research seeks to discover and understand the possible changes to stream morphology stemming from both trophic cascades and other fluvial factors. We use the stratigraphic and geomorphic record to document the late Pleistocene and Holocene history of stream behavior and assess how modern channel form and processes are related to the longer-term record of stream behavior. Other environmental factors that influence stream behavior include changes to wildfire regimes (Legleiter et al., 2003), changes to beaver damming frequency (Persico & Meyer, 2013) or climate-induced changes to flood frequency (Meyer et al., 1995). Research has indicated that fluctuations in beaver behavior, stream capture and fire related flood events could have triggered incision in the region (Persico & Meyer, 2009). A working map of the region provides the localities of critical stratigraphic relationships, and morphological features that better provide insight into the dynamic conditions along Blacktail Deer Creek. We hope to better understand when and where incision, aggradation, and channel shifts occurred along Blacktail Deer Creek by taking a holistic view and considering a large variety of potential fluvial altering factors.

STUDY AREA

Blacktail Deer Creek is located on the Blacktail Deer Plateau in the northern Yellowstone National Park. The Northern Yellowstone boundary is low in elevation (1604m) and dry (25-38cm of rain per year) compared to the rest of the park (Yellowstone National Park, 1997). The sage and grassland is covered with an intermittent series of forests. The East and West fork of Blacktail Deer Creek flows out of the Washburn range and across the Blacktail Deer Plateau to the Yellowstone River. West Fork Blacktail Deer Creek drains 35km2 and East Fork Blacktail Deer Creek drains 27km2. Blacktail Deer Creek flows on through glacial meltwater channels, remnants from the Pinedale glaciation that dominated Yellowstone during the Pleistocene. (Pierce, 1979; Meagher & Houston, 1998). The plateau is predominately covered in kame terraces that creates a hummocky topography (Pierce, 1979). On the kame surfaces, sagebrush dominates with interspersed islands of aspen and pine trees. The riparian areas of East and West Blacktail Deer Creek are covered with willow and sedge species (Beschta & Ripple, 2018). Additionally, the plateau is serves as elk winter range habitat as well as other ungulates and predators. The plateau also hosts a beaver population which have potential to greatly alter the fluvial characteristics of the stream (Smith, 2003).

METHODS

Field

We performed field work in July and August of 2019. This work was characterized by field mapping of geomorphic surfaces and valley floor topographic surveys along East and West Blacktail Creek. We mapped surfaces by hand-drawing contacts on a printed orthographic and DEM maps. We used a handheld GPS and printed maps to demarcate different surfaces. The accuracy of these contacts was aided via surveying through the use of RTK (1-cm accuracy) and D-GPS (20-cm accuracy) surveys. We mapped the kame boundaries, paleo-channels, river terraces, floodplain, and active channel. We completed this by walking contacts and analyzing relative elevational differences between each surface. We mapped the terrace highest above the modern channel (oldest terrace in the valley) as T1. Inset terraces, or younger fluvial terraces were marked as T2, T3, and so on depending on the height above the active channel. In addition to this mapping, detailed cross sections and longitudinal profiles of the drainages were made using RTK and D GPS. These cross sections were surveyed along each fork of the creek at intervals of approximately 30 meters. Cross sections were surveyed perpendicular to the stream and went from the edge of the kame, across the valley floor, to the opposite confining boundary of kame deposits. These were used to quantify terrace elevations relative to active and paleo channels. All the mapping and notes created during this phase of research served as guiding material for the later production of a digital map.

Stratigraphic sections were used to characterize the terrace deposits including sampling of organic material for 14C analyses. These locations were primarily focused around terraces near both active and paleo-channels. In order to locate datable material, active or old cut banks in the terrace were located and debris was cleared away to provide a clear look at the stratigraphy. We then searched the column for charcoal and other organic woody debris that would be suitable for radio carbon dating. Samples were then carefully collected, photographed, and recorded in detail about their location in the column. We also looked for volcanic ashes incorporated into terrace sediments. A volcanic ash collected was identified by the Pete Hooper GeoAnalytical Laboratory of Washington State University.

Laboratory

Using ArcGIS, we digitized the field maps. In ArcMap, the orthographic photos and identification of vegetation differences were readily identified. Kame surfaces are covered in sage and other fluvial surfaces are dominated by a variety of grass and bush species. This stark contrast in vegetation aided in the differentiation of kame terraces from fluvial terraces. Polygons were drawn over the top of kame deposits to show their locations on the map. Active channels were easily identified due the visibility of water. Using LiDAR derived DEM from NEON, other geomorphic surfaces could be noted. This DEM made for clear identification of paleo-channels and alluvial fans along the stream reaches. Lastly, the demarcation of distinct terrace surfaces was performed. The objective for terrace identification was to match up terrace deposits that had the same relief above the active channel. Additionally, the map separated out terraces that had lower relief within the valley. Profile lines as well the cross sections were used to create topographic profiles that were perpendicular to the active stream channel. These cross sections revealed the valley floor topography and the different terraces heights. Using multiple elevational profiles and the shading in the DEM, a terrace surface could be identified based upon its height above the active channel. Using this identified height above the active channel, terraces of different relative ages were demarcated with a polygon. In addition to the surficial map of geomorphic surfaces, raster slope maps, DEM's and hill shades were all produced as supplemental material to further interpret the landscape.

RESULTS

Based upon the field mapping, the use of a high-resolution DEM, and aerial photos a map showing the geomorphic surfaces of the valley floor was produced (Fig. 1). The mapping reveals that along East Fork of Blacktail Deer Creek, the majority of the valley bottom is the T1 terrace. The T1 terrace is the terrace with the highest relief (1.0-1.5 meters) above the active channel and therefore represents the oldest terrace. The cross sections show the relief for identifying the terrace surfaces (Fig. 2). This T1 terrace is incised where the T2 terrace and paleo-channels are preserved. The paleo-channels, incised primarily in T1 terraces, can be traced back to the location of the active channel. Additionally, this map shows that most of the inset terraces lie on active and abandoned point bars. The paleo-channels and T2 terraces are inset in the T1 terrace (Fig 1). Many of the T2 terrace surfaces are preserved along point bars along active channels or old paleo-channels that had incised into the T1 terrace. The cross section in Figure 2 shows the complexity in certain stream reaches because the active channel has not significantly incised. Along some reaches, the active channel is at a higher elevation relative to the proximal paleo-channel (Fig. 2).

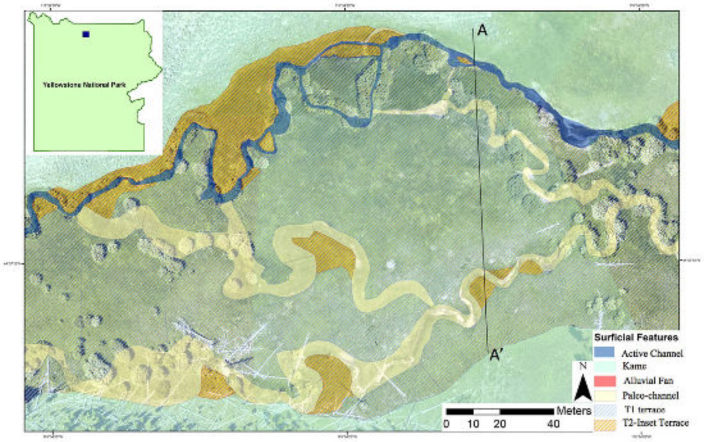

Figure 1. Surficial Geomorphic Map- East Blacktail Deer Creek. This image shows geomorphic surfaces overlaying the orthographic photo of the reach. A-A' shows the location of the cross section in Figure 2. Inset shows mapped area within the Yellowstone National Park Boundary.

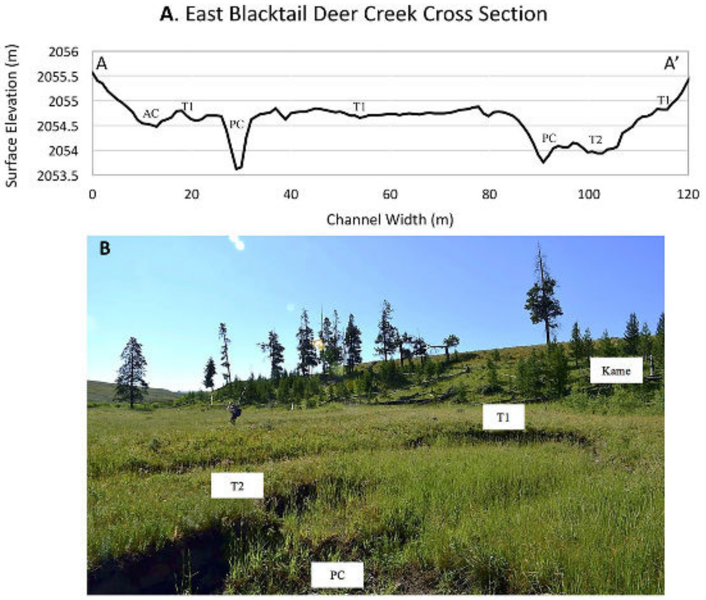

Figure 2. A) East Blacktail Deer Creek Cross Section from Figure 1. Labels on cross section indicate the identified feature on surficial geomorphic map. Kame is located on either side of the valley floor. Note paleo channels are at a lower elevation than the active channel on this reach. AC=active channel, PC= paleo-channel, T1= Uppermost Terrace, T2=inset terrace. B) East Fork of Blacktail Deer Creek. This image shows the surfaces that were identified during mapping. Notice person for scale.

It is important to constrain the geochronology for

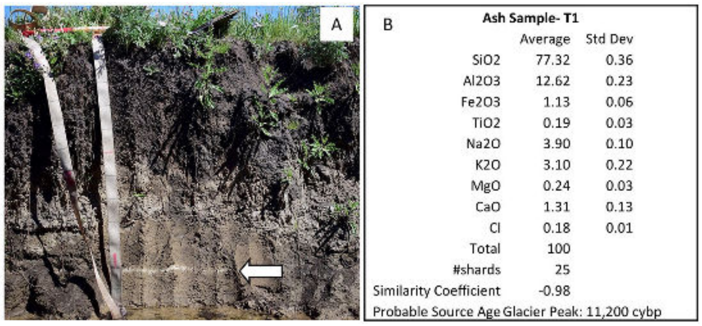

Ash Sample- T1

	Average	Std Dev
SiO2	77.32	0.36
Al2O3	12.62	0.23
Fe2O3	1.13	0.06
TiO2	0.19	0.03
Na2O	3.90	0.10
K2O	3.10	0.22
MgO	0.24	0.03
CaO	1.31	0.13
Cl	0.18	0.01
Total	100	
#shards	25	
Similarity Coefficient	-0.98	

Probable Source Age Glacier Peak: 11,200 cybp

Figure 3. A) Image of stratigraphic column containing volcanic ash. Arrow indicates ash deposit. Image courtesy of Lyman Persico. B) Analysis of glass composition of ash from T1 terrace on East Blacktail Deer Creek (normalized weight % oxides).

when each surface was formed was to interpret the geomorphic history of Blacktail Deer Creek. Terrace ages were constrained on the east fork with a series of radiocarbon dates and a volcanic ash. The ash layer is located 1m below the surface of the highest terrace, T1 (Fig. 2). Analysis of the glass contained in the ash indicates that it is from the eruption of Glacier Peak ca. 11.2 ka (Fig. 3). A radiocarbon date higher in the stratigraphy of the T1 Terrace produced a date of ~3.3 ka. The T1 terrace was aggraded between 11-3.3ka. Additionally, the T1 terrace contains a well-developed soil containing a thick A- horizon, which indicates long term stability. A slip terrace on the T2 surface is dated at 1.4ka (Persico & Meyer, 2009). Fluvial deposits inset within the high terrace on the east fork date to the late Holocene, 1.0-1.4 ka. Thus, incision of the highest terrace and subsequent deposition of the inset material occurred between 1.4-3.3ka.

The paleochannels, active channels, and terrace surfaces have different slopes along both east and west forks (Fig. 4). The direction and slope of the raster tiles reveals the slope trend in terraces, kame, active and paleo-channels. There are 15 paleo-channels at the area near the confluence. This projection also shows alluvial fan along the East Fork Blacktail Deer Creek. East Fork is suspended on top of kame east of the confluence thus allowing aggradation of the alluvial fan. The broad flat valley decreased stream power in the east fork, which deposited sediment and created an alluvial fan. The shallow slope of the fan ends with a distinct drop into the confluence (Fig. 4). West Fork Blacktail Deer Creek maintains a slope around 0.0174. East fork maintains a slope of 0.118.

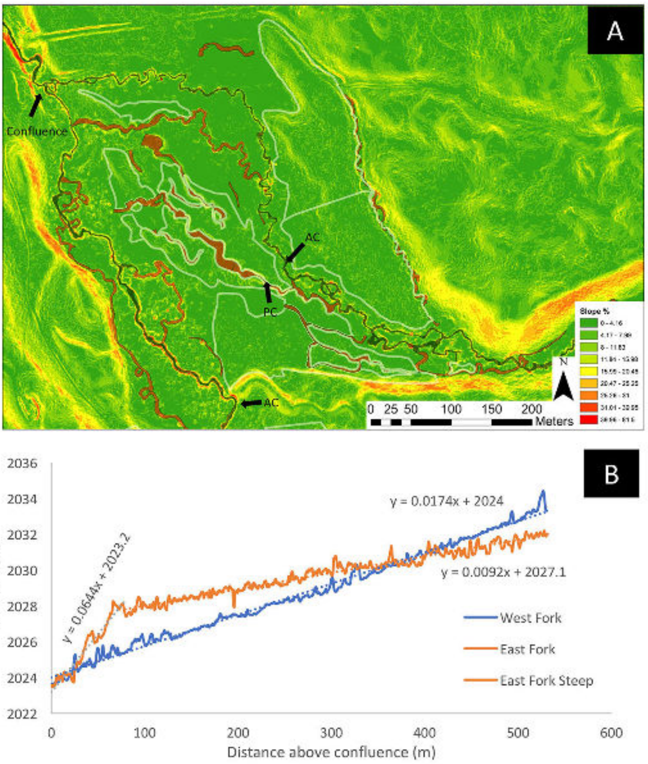

Figure 4. A) Slope Raster Map of confluence of West and Blacktail Deer Creek. East fork flows in from the right side of image and the west fork enters from the south. Black shaded region is the active channels and red shading shows the paleo-channels. White outlines Kame. B) Longitudinal profile showing the slops of West and East Fork Blacktail Deer Creek.

DISCUSSION

The morphology of the West and East forks of Blacktail Deer Creeks are influenced by both Holocene and late Pleistocene geomorphic events. The Pinedale and Bull Lake glaciation events produced large amounts of ice and meltwater that influence much of the modern topography. The glacial meltwater channels and kame deposits control the drainage network pattern and net ability for channel incision. Glaciation during the Pleistocene deposited voluminous kame deposits and created a complex series of meltwater channels (Pierce, 1979). Much of this kame surface contains large cobbles and boulders that anchor the features into place and prevent incision in modern creeks. These meltwater channels and kame surfaces have dictated where Blacktail Deer Creek can currently flow. Given the size of stream and size of the sediment in the outwash deposits, the stream cannot move or meander beyond the confines of the meltwater channels. This has effectively confined drainage network of Blacktail Deer Creek. On East

Fork Black Tail Deer Creek, the slope of the channel is controlled by the kame terrace located just above the confluence (Fig. 4b).

The significance of the T1 terrace is that it records a long-term record of valley floor aggradation and then surface stability. The T1 terrace comprises most of the valley floor and formed between 11-3.3ka. The T1 terrace represents a system-wide aggradation of the valley floor. This widespread aggradation is likely a result of changes to sediment supply to valley floors related to deglaciation of the Yellowstone Plateau. Voluminous aggradation occurs after glaciation because sediments are being flushed out of over-steepened glacial deposits (Church & Ryder, 1972). These paraglacial processes may have resulted in widespread valley floor aggradation and the creation of the T1 terrace along relatively small streams like Blacktail Deer Creek that were able to effectively transport all sediment moved from hillslopes to the valley floor. The inset terraces (T2) date to the late Holocene at 1.0-1.4 ka. The T2 surfaces, often located on meander bends, are evidence of a transition of the fluvial system to channel both lateral migration and incision. The T2 dates and locations in the stream system indicate a fundamental change occurred along Blacktail Deer Creek between 1.4-3.3ka. During this time-period the incision of the T1 terrace began and the deposition of the inset terraces began. This boundary marks a critical period in which the stream is no longer carrying paraglacial sediments but has transitioned to the start of the neoglacial (Whitlock, 1993). This change to cooler conditions could increase stream discharge at the same time that sediment loads are decreased due to more vegetation on hillslopes. This incision significantly predates the removal and reintroduction of wolves in Yellowstone National Park. Additionally, the paleochannel mapping demonstrates that channel avulsion and incision has occurred well before the streams moved to their current location. The widespread occurrence of the T1 terrace over majority of the valley floor, indicates that much of the valley floor is not influenced by recent channel modifications. Therefore, trophic-cascade factors are not the only variable causing geomorphological changes along Blacktail Deer Creek. While wolves and trophic cascades have the potential to affect streams, the changes along Blacktail Deer Creek other factors in the Holocene such as climatic variability and hillslope sediment supply are also important controls on the channel. Changes in fire regimes, or stream captures stimulated the morphological shifts along East and West Blacktail Deer Creek. The complexity of the environment requires analysis of all the factors involved in the creek morphology, and not exclusive analysis of ecological elements.

ACKNOWLEDGEMENTS

This material is based upon work supported by the Keck Geology Consortium and the National Science Foundation under Grant No. 1659322.

REFERENCES

Beschta, R., & Ripple, W. (2006). River channel dynamics following extirpation of wolves in northwestern Yellowstone National Park, USA. Earth Surface Processes and Landforms, 1525-1539.

Beschta, R., & Ripple, W. (2018). Can Large Carnivores Change Stream via a Trophic Cascade? Ecohydrology, 1-13.

Chadde, S., & Kay, C. (1991). Tall-willow Communities on Yellowstone's Northern Range: A Test of the "Natural Regulation" Paradigm. The Greater Yellowstone Ecosystem, 231-263.

Church, M., & Ryder, J. (1972, October). Paraglacial sedimentation: a consideration of fluvial processes conditioned by glaciation. GSA Bulletin, 83(10), 3059-3071.

Knight, R., & Landres, P. (1998). Stewardship Across Boundaries. Washington D.C.: Island Press.

Laundré, J., Hernández, L., & Altendork, K. (2001). Wolves, Elk and Bison: Reestablishing the "Landscape of Fear" in Yellowstone National Park, USA. Canadian Journal of Zoology, 79, 1401-1409.

Legleiter, C., Fonstad, M., Aspinall, R., Lawrence, R., & Marcus, W. (2003). Fluvial Response a Decade after Wildfire in the Northern Yellowstone Ecosystem: a Spatially Explicit Analysis. Geomorphology, 54(3-4), 119-136.

Marshall, K., Thompson Hobbs, N., & Cooper, D. (2013). Stream Hydrology Limits the Recovery of Riparian Ecosystems after Wolf

Reintroduction. Proceedings of the Royal Society B-Biological Sciences, 1756.

Meagher, M., & Houston, D. (1998). Yellowstone and Biology of Time. Norman: University of Oklahoma Press.

Meyer, G., Wells, S., & Timothy Jull, A. (1995). Fire and Alluvial Chronology in Yellowstone National Park: Climatic and Intrinsic Controls on Holocene Geomorphic Processes. Geologic Society of America Bulletin, 107, 1211-1230.

National Research Council. (2002). Ecological Dynamics on Yellowstone's Northern Range. Washington,DCd: National Academy of Sciences.

Persico, L., & Meyer, G. (2009). Holocene beaver damming, fluvial geomorphology, and climate in Yellowstone National Park, Wyoming. Quaternary Research, 340-353.

Persico, L., & Meyer, G. (2013). Natural and Historical Variability in Fluvial Processes, beaver activity, and Climate in the Greater Yellowstone Ecosystem. Earth Surface Processes and Landforms, 38, 728-750.

Pierce, K. (1979). History and Dynamics of Glaciation in the Northern Yellowstone National Park Area. Geological Survery Professional Paper, 1-90.

Ripple, W., & Beschta, R. (2004). Wolves and the Ecology of Fear: Can Predation Risk Structure Ecosystems? BioScience, 54(8), 755-766.

Ripple, W., & Beschta, R. (2011). Trophic Cascades in Yellowstone: The first 15 years after wolf introduction. Biological Conservation, 205-213.

Smith, D. (2003). 2003 Beaver Survey. National Park Service, Department of the Interior. Mammoth , WY: Natinal Park Serrice.

Whiting, P., Matisoff, G., Fornes, W., & Soster, F. (2005). Suspended Sediment Sources and Transport Distances in the Yellowstone River Basin. Geologic Society of America Bulletin(117), 515-529.

Whitlock, C. (1993). Postglacial vegetation and climate of Grand Teton and southern Yellowstone National Parks. Ecological Monographs, 63(2), 173-198.

Wolf, E., Cooper, D., & Hobbs, N. (2007). Hydrologic Regime and Herbivory Stablilize an Alternative State in Yellowstone National Park. Ecological Applications, 1401-1409.

Yellowstone National Park. (1997). Yellowstone's northern range : complexity & change in a wildland ecosystem. Mammoth Hot Springs, Wyoming: National Park.

KECK Geology Consortium
Learning Science Through Research
Published by the Keck Geology Consortium
Short Contributions
Keck Geology Consortium
Volume 33
May 2020
doi: 10.18277/AKRSG.2020.33.19

POTENTIAL MECHANISMS OF GEOMORPHIC CHANGE OPERATING ON FLOODPLAIN AND CHANNEL FORM ON THE GALLATIN RIVER IN NORTHWESTERN YELLOWSTONE

ALICE HINZMANN, Carleton College
Research Advisor: Mary Savina

INTRODUCTION

In recent years, northern Yellowstone National Park has drawn interest from scientists interested in the region's ecology. Of particular interest to researchers is the effect of wolf extirpation on ecosystem health. After the removal of wolves in the 1920s, predation of elk dropped significantly, and consequently the elk population skyrocketed (Kay, 1997). This larger population of elk has over-grazed the willow population in some regions of Yellowstone, decreasing food sources for other animals such as beaver. Beaver are a keystone species because their dams slow down stream velocity, promoting the development of floodplains and riparian zones (Ripple and Beschta, 2012). The relationship between beaver and willow is a positive feedback loop, as drained beaver ponds provide an ideal location for willow establishment (Wolf et al., 2007). Some have hypothesized that due to beaver loss in Yellowstone, stream incision has occurred in the northern area of the park (Beschta and Ripple, 2006 and 2019). This has resulted in streams that are disconnected from their historical floodplains, thus diminishing riparian habitat.

After the reintroduction of wolves into the ecosystem in 1995, researchers became interested in whether the effects of the extirpation of wolves could be reversed, and to what degree. Wolf et al. (2007) examine the codependent nature of beavers and willows, and determine that while the reintroduction of wolves has caused a decrease in the elk population, this action alone is not sufficient to return the Yellowstone landscape to its historical state. Instead, the authors posit that the increased stream incision during the period of willow over-grazing has rendered a return to the historical state impossible. However, other research has pointed to the recovery of these riparian zones with the establishment of new inset floodplains in areas where willows have begun to recover from elk herbivory (Beschta and Ripple, 2019).

This study focuses on the geomorphology and hydraulic dynamics of the Gallatin River in northwestern Yellowstone. The goal of the research is to determine what factors influence fluvial processes and channel form to help understand the potential for trophic cascade related changes to the geomorphology. This study investigates the hydraulic processes of the river and determines whether the floodplain and terrace surfaces that border the river are inundated by 2-year, 5-year, or 10-year floods. With this data, I seek to understand potential geomorphic controls on the Gallatin River, and whether they are related to the ongoing research into the effects of trophic cascades resulting from wolf extirpation and reintroduction.

GEOLOGICAL SETTING

The Gallatin River originates in the Gallatin Range of the Rocky Mountains and flows northwest before converging with the Missouri River. The upper Gallatin Basin is located at an elevation of around 2000 meters, with prominent mountain peaks and wide valley bottoms (Beschta and Ripple, 2006). The Gallatin Range was glaciated during the last glacial maximum (LGM), and there are moraines, outwash terraces, and glacial lake sediments influencing the valley floor morphology (Pierce, 1979).

This study focuses on the section of the Gallatin River that runs through the park. Data was collected at five reaches along the river (Fig. 1). The studied section of the river runs through a valley with gradual elevation change. Reach 1 is located the farthest upstream and is typified by high sinuosity and marshland in its upper section. Reach 2 continues along the valley floor and splits into multiple channels for some sections of the reach. Both Reach 1 and Reach 2, which are separated by a small feeder creek, are located outside of elk winter range (Beschta and Ripple, 2006). Reach 3 is marked by the confluence of Fan Creek with the Gallatin River and by multiple active channels. Reach 4 and Reach 5 are located just upstream of the border between Yellowstone National Park and the Gallatin National Forest.

METHODS

We characterized channel and floodplain dimensions by surveying valley cross sections along the Gallatin River using high-resolution RTK GPS (accurate within 1-2 cm), supplemented with a total station when necessary. These data were collected in August 2019. Upon returning from the field, I created a hydraulic model of the Gallatin River using the US Army Corps of Engineers' Hydrologic Engineering Center's River Analysis System (HEC-RAS). The program requires two types of data to build the channel flow model; channel geometry/characteristics and stream discharge.

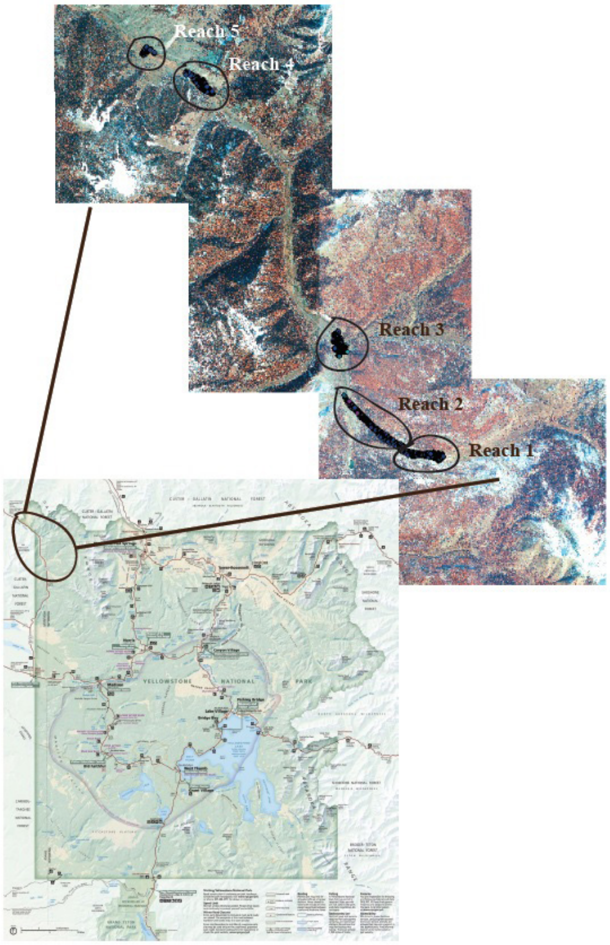

Figure 1. Map of the study area, including cross section locations.

To generate the channel geometry for each reach, I implemented the GPS and total station data that were collected in the field. I then input Manning's roughness values for the channel and the banks of 0.03 and 0.15, respectively. These values were selected based off of roughness values from Arcement and Schneider (1989). In order to represent the singular channel flow that defines most of the study area, I applied the HEC-RAS levee marker on reaches where the model inaccurately predicted multi-channel flow.

To estimate discharge during flooding events I used multiple regression methods to estimate discharge on the Gallatin River, which is not gauged in our study area. I was able to determine discharges for the 2-year, 5-year, and 10-year floods based off of the following United States Geological Survey (USGS) formula for calculating discharge for ungauged sites on a gauged stream (Parrett and Johnson, 2004):

$$Q_{T,U} = Q_{T,G}\left(\frac{DA_U}{DA_G}\right)^{exp_r}$$

In this equation, $Q_{T,U}$ and $Q_{T,G}$ are the peak flows in cubic feet per second for the T-year flood at the ungauged and gauged site, respectively. DA_U and DA_G are the drainage areas in square miles for the ungauged site and the gauged site, respectively, and exp_r is the regression coefficient that corresponds to the T-year flood.

I generated a plot of typical discharge for the 2-year, 5-year, and 10-year floods on the Gallatin Gateway stream gauge using the USGS PeakFQ program. The drainage area of the Gallatin River at the Gallatin Gateway gauge station is 1318 km2 per the USGS Water Data site, and I determined the drainage areas for each of the five reaches using topographic maps and Google Earth. The values I used for expAEP in the study area are listed in the USGS report on estimating flood frequency in Montana through water year 1998 (Parrett and Johnson, 2004). For the Gallatin River, which falls within the Upper Yellowstone-Central Mountain Region, these values were 0.877, 0.768, and 0.712 for the 2-year, 5-year, and 10-year floods respectively.

After calculating the discharge values, I entered them into steady flow data along with the slope of each reach, which I calculated using the measurement tools in the HEC-RAS program. With these data, I ran a total of 15 steady flow analyses – three simulations per reach.

RESULTS

For each reach in the study area, I determined whether the floodplains were consistently inundated across the entire reach at the 2-year, 5-year, and 10-year floods. I considered a reach's floodplains to be consistently inundated when the water level achieved bankfull stage in at least half (≥ 50%) of the cross sections for that reach. A summary of my findings can be found in Figure 2. During the 2-year flood, the floodplains for 0 out of 5 reaches are consistently inundated. For the 5-year flood, 2 out of 5 reaches—reaches 3 and 4—have floodplains that are consistently inundated. During the 10-year flood, the floodplains are consistently inundated in 5 out of 5 reaches.

DISCUSSION

As indicated by the results, the majority of the reaches in this study require at least a 10-year flood in order for their floodplains to be consistently inundated. In a typical stream, a flood with a recurrence interval of 4 years will produce a bankfull flow and affect the channel (Leopold et al., 1964). Thus, it seems unlikely that a large flood is required for the floodplains on the Gallatin River to be inundated. This clear separation between the Gallatin River and its floodplains indicates that the stream has incised over time.

Channel incision on the Gallatin River may be due to the loss of beaver and willow populations from the park after wolf extirpation. However, it is also important to consider other possible geomorphic controls acting on the Gallatin River and how they may affect channel morphology.

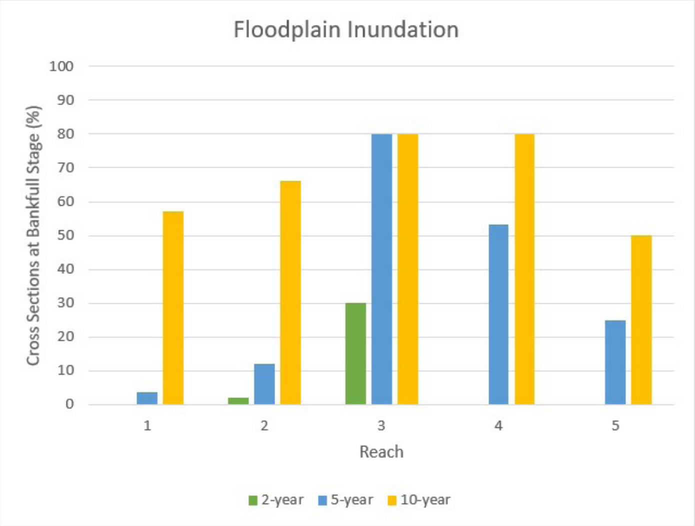

Figure 2. A summary of the HEC-RAS simulations displaying the percentage of inundated cross sections per flood for each cross section.

Wolf Extirpation and Riparian Vegetation Loss

One possible explanation for the current morphology of the Gallatin River is channel incision as a result of losing riparian vegetation. Beschta and Ripple lay out such a hypothesis in their 2006 paper, where they claim that a trophic cascade driven by the extirpation of wolves from Yellowstone was the cause of this vegetation loss.

As described by Kay (1997), wolf extirpation was directly responsible for an elk population boom, which in turn has led to overbrowsing of willows and a decrease in their population. Willows are considered riparian vegetation, which means that they contribute to the development of effective floodplains. Riparian vegetation is effective in maintaining bank stability and preventing excessive channel erosion. When this vegetation is removed, banks can become unstable and a greater degree of channel erosion may occur. This increased channel erosion leads to separation of a river from its floodplains, as the channel continues to incise to a point where the original floodplain can no longer be inundated. This may be the case along the Gallatin River in several places. In Reach 5, such channel incision is clearly evident (Fig. 3). The water level achieves bankfull stage in 2 out of 4 cross sections during the 10-year flood, but it is clear from the cross

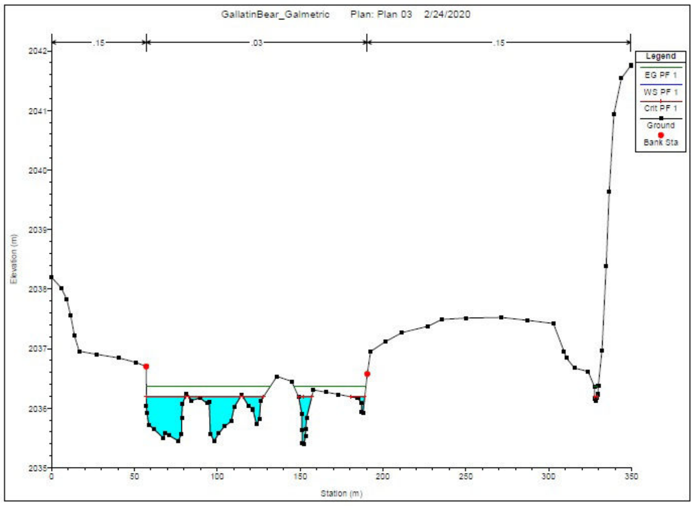

Figure 3. HEC-RAS output for Reach 5, cross section 1 during the 10-year flood.

sections that the stream has incised through a surface 0.5-1.0 m above the current channel. Instead, when Reach 5 is inundated by a 10-year flood, the bankfull stage achieved by the water level is at the elevation of what appears to be an inset floodplain. As proposed by Beschta and Ripple (2019), inset floodplains indicate that a channel is recovering from a period of high incision. If it is the case that these inset floodplains started forming after the reintroduction of wolves, then they would be evidence in favor of the theory that wolf extirpation led to channel incision.

Other Potential Geomorphic Controls

A loss of riparian vegetation due to elk herbivory is not a sufficient explanation for the apparent channel incision that has occurred along the entire study area. As previously mentioned, both Reach 1 and Reach 2 are located outside of elk winter range. Therefore, these areas have not been subject to intensive elk herbivory. If elk herbivory were the dominant control on channel form, then there would be more floodplain inundation in the upper reaches than the downstream reaches. This is not the case, as there are several cross sections in reaches 1 and 2 where the water level does not achieve bankfull stage even during the 10-year flood, much like in Reach 5 (Fig. 4). Elk herbivory may be exerting an influence over channel morphology in the lower reaches, but it does not do so for the upper reaches. Thus, an alternate explanation is needed.

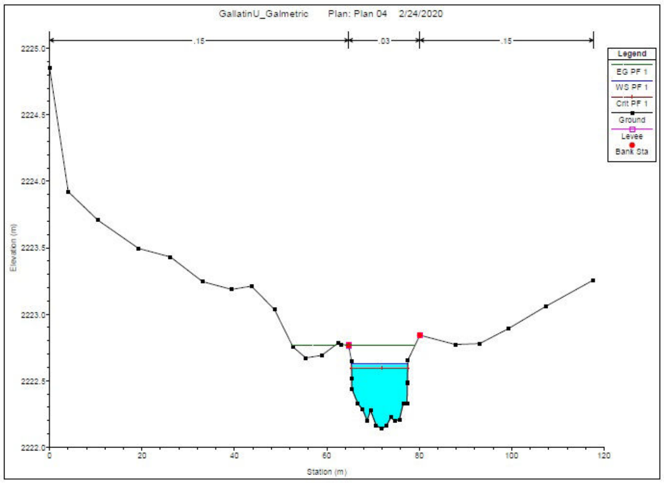

Figure 4. HEC-RAS output for Reach 1, cross section 6 during the 10-year flood.

Much of the Gallatin River runs over glacial till and outwash gravels (REF). There are sections throughout where the channel base contains several pebbles wider than 180 cm, and few pebbles of sand size or smaller. The presence of pebbles of this size indicates that the high discharge of the Gallatin River has removed the smaller size fractions from the channel base. Further channel incision in these areas would require the removal of glacial till, which is not possible for a river the size of the Gallatin. Thus, when discharge is high, such as in a flood event, the channel incises outward instead of down. Channel expansion also accounts for the infrequent inundation of floodplains on reaches 1 and 2 during the 2-year and 5-year floods. As the channel expands, more water is required to achieve bankfull stage. In the upper reaches of the Gallatin River where the stream discharge is lower, a larger flood is required in order to fill the channel and inundate the floodplain.

Another potential geomorphic control on the Gallatin River is channel slope. The water surface profiles for most of the study area exhibit slope values between 0.01 and 0.013. However, in the upstream section of Reach 1, the slope is 0.0015 (Fig. 5). Additionally, cross sections located in the flat portion of Reach 1 exhibit more floodplain inundation than the cross sections located in the steeper portion of Reach 1. Reaches 1, 2, and 3 are located on a recessional moraine from the LGM, which influences the flat topography in this area. This section is also unique among the study area in terms of the channel bed.

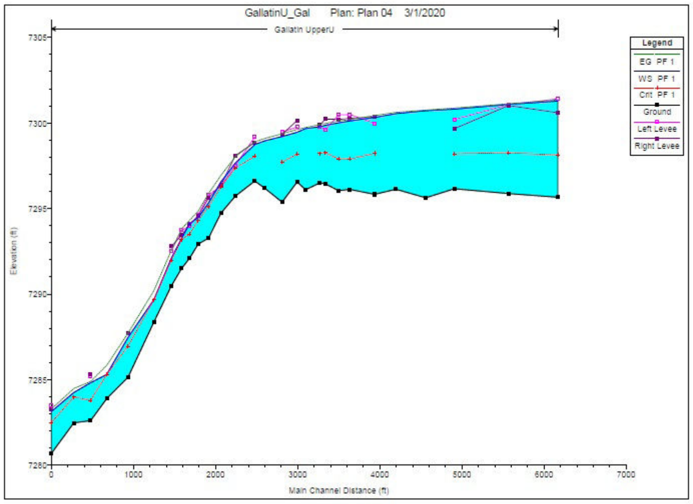

Figure 5. HEC-RAS output of the water surface profile for Reach 1 during the 10-year flood.

While much of the study area is characterized by larger pebble size fractions, the upstream section of Reach 1 contains a much larger percentage of pebbles 2 mm and smaller.

The makeup of the channel bed in the upper section of Reach 1 may indicate that the water velocity in that section is too low to move most pebble sizes. In such a case, it is unlikely that channel incision has occurred on a measurable scale. If the difference between a reach where only glacial till remains and a reach where there are pebbles of all size fractions is the slope, then it must play an important role in stream morphology along the Gallatin River.

CONCLUSION

On the Gallatin River, a 10-year flood is required to consistently inundate the floodplain in each of the studied reaches. This result indicates that the river is currently separated from a well-defined surface 0.5-1.0m above the channel. The reasons for this separation may be complicated, as the underlying geomorphology of the Gallatin River is not consistent along the stream. It is likely that the upstream reaches and the downstream reaches are acted upon by different processes that have caused the separation. In the downstream reaches, channel incision appears to be the main mechanism of separation, and may also be responsible for promoting the development of an inset floodplain. In the upstream reaches, channel bed material and channel slope exhibit a more drastic influence on overall channel morphology.

It is possible that the extirpation and subsequent reintegration of wolves in Yellowstone have had effects on the geomorphology of the Gallatin River in the lower reaches of the study area. However, the channel morphology of the upper reaches cannot be explained by the same mechanism. In fact, channel incision appears unable to affect the upper reaches. More research should be conducted on these upper reaches in order to better understand the morphology that governs them.

ACKNOWLEDGEMENTS

This material is based upon work supported by the Keck Geology Consortium and the National Science Foundation under Grant No. 1659322. Thank you to my advisors, Dr. Lyman Persico and Dr. Mary Savina, who guided me through this process. Additionally, I would like to thank the others in the research group: T. Fokey, C. Iosso, A. Phinney, and E. Van Wetter. I would also like to thank my family and friends for their nonacademic—but just as crucial—support.

REFERENCES

Arcement, G. J., Jr., and Schneider, V. R., 1989, Guide for Selecting Manning's Roughness Coefficients for Natural Channels and Flood Plains: U.S. Geological Survey Water-Supply Paper 2339, 38 p.

Beschta, R. L., and Ripple, W. J., 2006, River channel dynamics following extirpation of wolves in northwestern Yellowstone National Park, USA: Earth Surface Processes and Landforms, v. 31, p. 1525-1539.

Beschta, R. L., and Ripple, W. J., 2019, Can large carnivores change streams via a trophic cascade?: Ecohydrology, v. 12, doi: 10.1002/eco.2048

Kay, C. E., 1997, Viewpoint: Ungulate herbivory, willows, and political ecology in Yellowstone: Journal of Range Management, v. 50, p. 139-145.

Leopold, L. B., Wolman, M. G., and Miller, J. P. (1964). Fluvial processes in geomorphology: W. H. Freeman and Company, San Francisco, California.

Parrett, C., and Johnson, D. R., 2004, Methods for Estimating Flood Frequency in Montana Based on Data through Water Year 1998: U.S. Geological Survey Water-Resources Investigation Report 03-4308, 99 p.

Pierce, K. L. (1979). History and dynamics of glaciation in the northern Yellowstone National Park area. Professional Paper.

Ripple, W. J., and Beschta, R. L., 2012, Trophic cascades in Yellowstone: The first 15 years after wolf reintroduction: Biological Conservation, v. 145, p. 205-213.

Wolf, E. C., Cooper, D. J., and Hobbs, N. T., 2007, Hydrologic regime and herbivory stabilize an alternative state in Yellowstone National Park: Ecological Applications, v. 17, p. 1572-1587.

KECK Geology Consortium
Learning Science Through Research
Published by the Keck Geology Consortium
Short Contributions
Keck Geology Consortium
Volume 33
May 2020
doi: 10.18277/AKRSG.2020.33.20

CLIMATE INFLUENCES ON STREAM PROCESS IN YELLOWSTONE OVER THE LAST 7000 YEARS: A LOOK AT THE STRATIGRAPHIC RECORD

CHANTAL IOSSO, Washington and Lee University
Research Advisor: David Harbor

INTRODUCTION

Yellowstone National Park (YNP), America's first National Park, experienced many different management strategies since its inauguration. By 1926, wolves were essentially eradicated from YNP as part of a widespread predator control program throughout the United States. Park managers, concerned that the excessively large elk populations were degrading riparian habitat in elk wintering areas, employed a widely unpopular elk-culling program in the 1960s (Keiter & Boyce, 1991). In 1995, in an attempt to restore the ecosystem, the NPS reintroduced gray wolves to the park (Wolf, Cooper, & Hobbs, 2007). This sequence of management decisions coincided with major variations in YNP ecosystems, leading to debate over the impacts of wolves in the park.

The Northern Range encompasses the northern portion of YNP at low elevation with minimal snowpack where the northern elk herd spends winters (Yellowstone National Park 1997). Impacts to the ecosystem related to wolf removal and restoration is the subject of significant debate (Yellowstone National Park 1997). When wolves were removed in the early 1900s, elk overconsumed willows and other woody plants along streams, depriving beaver of their food and dam-building materials. Beavers were effectively outcompeted for resources and extirpated from the ecosystem (Chadde & Kay 1991). Beschta and Ripple (2018) suggest that overconsumption of willows lowered root density in the stream banks, reducing their shear strength and increasing erodibility in floods, resulting in incised and widened streams. Following wolf reintroduction in 1995, some streams experienced taller willow, evidence of beaver activity, and a new inset floodplain (Beschta and Ripple 2018). These observations suggest that stream channels have begun to "recover" due to trophic cascade-initiated ecosystem processes. Similarly, songbird and bear populations increased during this period, which Ripple & Beschta (2012) tie to trophic cascades after wolf restoration. Other studies support the trophic cascade hypothesis as a driver for ecosystem change following wolf removal, but consider changes irreversible: Marshall, Hobbs, & Cooper (2013) compared willow regrowth in areas with and without artificial damming and elk herbivory, and found that without beaver damming, excluding elk did not result in significantly increased growth of willows. They concluded that willows could not recover following stream incision they connect to wolf removal. Others question the trophic cascade mechanism for willow recovery due to lack of evidence of recovery (Kauffman et al. 2010) or insufficient replication, control, or acknowledgement of other potential causes in trophic cascade studies (Ford & Goheen 2015; Peterson et al. 2014).

Commonly the late 19th and early 20th centuries, prior to wolf removal, is used as a guide for the natural condition of the YNP ecosystem. The period was, however, the wettest period in the past 700 years, followed by an unusually dry period (severe droughts in the 1930s and 1950s) during the time that wolves were absent (Gray et al. 2007). Climatic variability may be an important factor in the ecosystem changes and stream dynamics in Yellowstone. For example, previous radiocarbon dating work on streams in the Northern Range indicate that beaver abundance and channel aggradation can be influenced by millennial scale climate changes (Persico and Meyer 2013). Fire, which is often concurrent with dry periods in YNP, is also a major control on stream dynamics (Meyer et al., 1995). Aggradation of alluvial fans occurs during warm periods, because periodic intense rain events after drought and fires trigger voluminous hillslope sediment transport and debris flow deposition on fan surfaces. This same process could also result in floodplain aggradation. Legleiter et al. (2003) also connect fires to stream morphology changes in YNP. Immediately after fires, excess sediment transported from hillslopes take 5-10 years to move downstream. Higher discharges on the sediment-depleted landscape then result in incision (Legleiter et al. 2003). These previous studies clearly link climate and stream changes.

We hypothesize that beaver pond deposits will be more frequent during wet periods, while fire-related deposits and floodplain aggradation will occur more during periods of drought. In order to determine the relationship between climate, beaver activity, and stream incision/aggradation in YNP, we compare the record of stream deposits, including beaver activity with climatic records over the last 7000 years. Dated beaver-pond sediments will provide information about the times that beaver activity was high over this period, while ages of different surfaces such as floodplains will constrain the timing of stream deposition and incision. Climate-related trends in beaver-pond deposits over the late Holocene will draw into question the singularity of the trophic cascade hypothesis as a mechanism for ecosystem change.

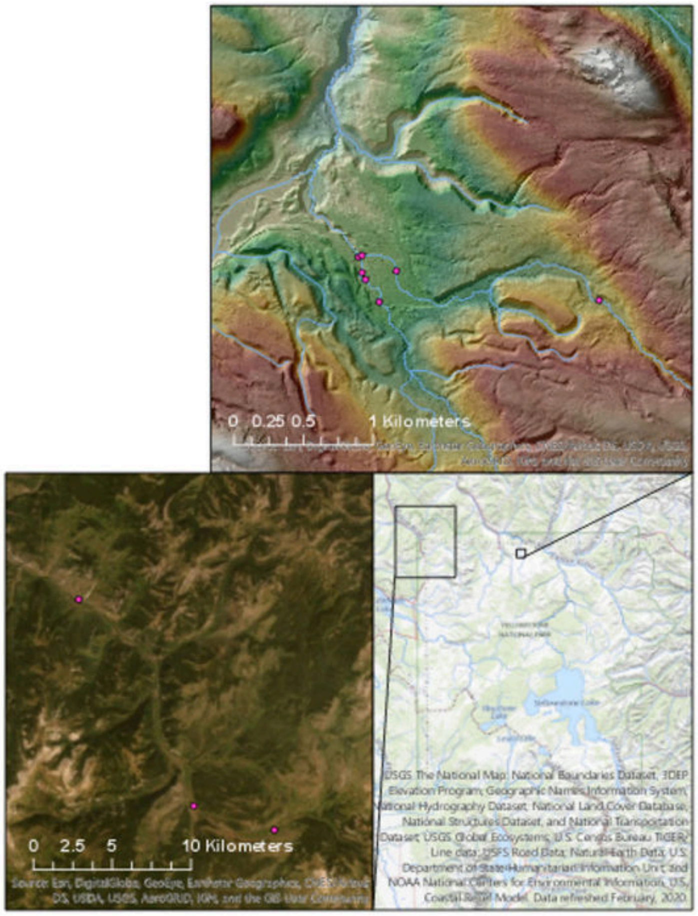

Figure 1. Blacktail Deer Plateau sampling sites (top) and Gallatin River sites (left) where we dated radiocarbon samples are identified here with pink dots, compared to their position in Yellowstone National Park (bottom right). Topographic surface is courtesy of LIDAR data provided by NEON.

If climate plays a major role in controlling ecosystem and stream dynamics in YNP, future aridification of the west could be an important influence on stream behavior in addition to trophic cascade events.

METHODS

We spent four weeks during the summer of 2019 in the Northern Range of Yellowstone National Park collecting data for this project. The project focused on Blacktail Deer Creek and the Gallatin River, as both are locations where channels have possibly changed by trophic cascade-related events (Beschta & Ripple, 2006, and 2018). The East and West Forks of Blacktail Deer Creek drain 27 and 35 square kilometers, respectively. Radiocarbon samples were collected along 12 sites on the Blacktail Deer Plateau, near the north entrance of Yellowstone, and at 9 sites along the Gardiner River, in northwest YNP (Figure 1).

Sources sampled for radiocarbon included cutbanks, terraces, floodplains, and beaver pond deposits, which will provide information of beaver activity, rates of deposition of streams, and ages of geomorphic surfaces over the last 7000 years, independent of wolf removal. The majority of these sites are within the elk winter range, where the impacts of elk overpopulation caused by wolf removal (including stream widening and reduced beaver populations) would be most apparent. Areas we sampled that extend beyond the northern range of the elk herd should exhibit completely different geomorphic characteristics, if wolf control of elk populations are the main factors influencing stream morphology in this area.

Sample collection: At each site, I cleared a fresh,

Table 1. All samples collected and dated for this study.

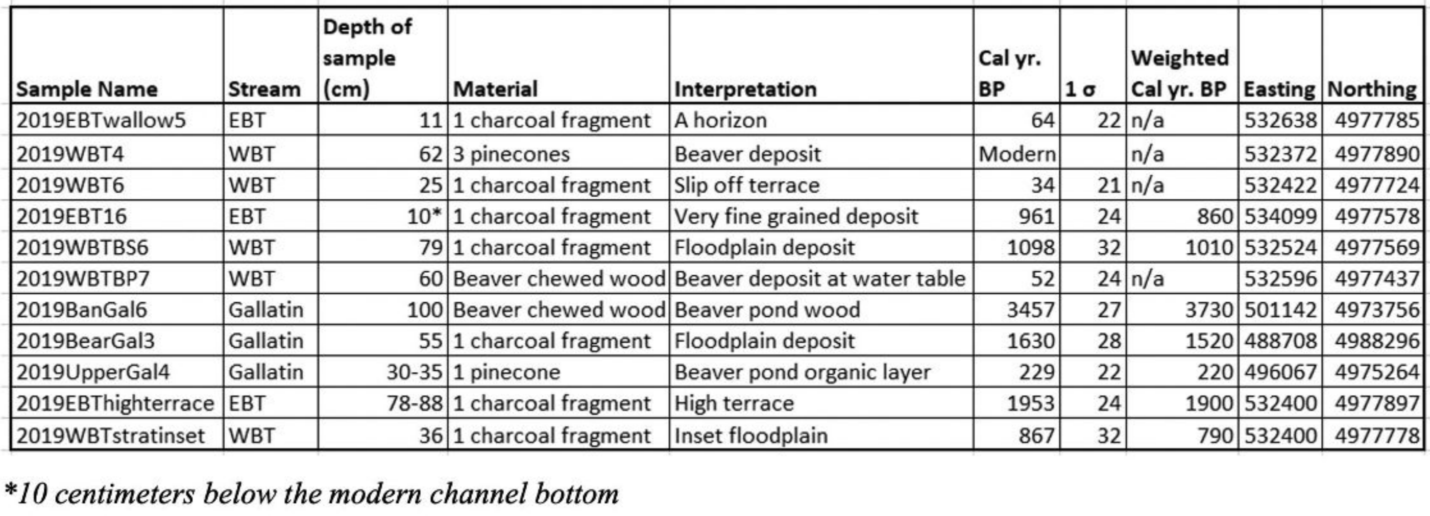

Sample Name	Stream	Depth of sample (cm)	Material	Interpretation	Cal yr. BP	1 σ	Weighted Cal yr. BP	Easting	Northing
2019EBTwallow5	EBT	11	1 charcoal fragment	A horizon	64	22	n/a	532638	4977785
2019WBT4	WBT	62	3 pinecones	Beaver deposit	Modern		n/a	532372	4977890
2019WBT6	WBT	25	1 charcoal fragment	Slip off terrace	34	21	n/a	532422	4977724
2019EBT16	EBT	10*	1 charcoal fragment	Very fine grained deposit	961	24	860	534099	4977578
2019WBTBS6	WBT	79	1 charcoal fragment	Floodplain deposit	1098	32	1010	532524	4977569
2019WBTBP7	WBT	60	Beaver chewed wood	Beaver deposit at water table	52	24	n/a	532596	4977437
2019BanGal6	Gallatin	100	Beaver chewed wood	Beaver pond wood	3457	27	3730	501142	4973756
2019BearGal3	Gallatin	55	1 charcoal fragment	Floodplain deposit	1630	28	1520	488708	4988296
2019UpperGal4	Gallatin	30-35	1 pinecone	Beaver pond organic layer	229	22	220	496067	4975264
2019EBThighterrace	EBT	78-88	1 charcoal fragment	High terrace	1953	24	1900	532400	4977897
2019WBTstratinset	WBT	36	1 charcoal fragment	Inset floodplain	867	32	790	532400	4977778

10 centimeters below the modern channel bottom

vertical face of stratigraphy to analyze. I sampled any exposed organic material such as charcoal, beaver-chewed wood, or pinecones. Large angular charcoal fragments were sampled to avoid errors associated with inbuilt age (e.g. redeposition or organic material that is significantly older than the deposit). Each sample was bagged individually (without touching the sample) with depth from the surface, soil/stratigraphy description, and GPS location. Each soil and stratigraphic layer was also described (color, texture, material, etc.), interpreted, and sampled. I also photographed the stratigraphy with a scale for future interpretation.

Sample preparation: I refrigerated soil and radiocarbon samples until I could dry them in an oven at 105 degrees Celsius for several hours, to evaporate off all the water. Then, I used a binocular microscope, tweezers, and x-acto knives to clean all modern organic matter or contaminants off the radiocarbon samples for dating, such as small roots and clay. Cleaned samples were then placed into new, sterile, labelled packages for shipping.

Radiocarbon dating: Two shipments with 20 total samples were shipped to DirectAMS, a radiocarbon dating lab. I used Calib704, a radiocarbon dating calibration program, to determine the potential distribution of ages for the samples given a variable record of C14 production over time in the atmosphere (Stuvier, Reimer, & Reimer 2020). We summed the probability that a deposit was associated with each year multiplied by the year to produce a weighted calibrated age. Weighted calibrated ages better estimate the potential age of the sample and are more stable than using the intercept alone (Telford et al. 2004).

RESULTS

Streams on the Blacktail Plateau are inset within glacial outwash channels amongst higher kame terraces from the Last Glacial Maximum (Pierce 1979). In the outwash, 1.5 meters above the current channel and associated abandoned meanders, there is a consistent, extensive fluvial surface along both forks of the Blacktail stream. We sampled radiocarbon from this surface and surfaces inset within it at a range of depths and sites (Table 1 has a full list of sites sampled; Fig. 2 shows examples of floodplain and beaver-pond deposits sampled). Many of the analyzed stratigraphies exhibited thick, developed A-horizons (Fig. 2).

Most beaver activity is within the last 500 years, a wetter period. Ages of beaver-pond deposits overlap between this and previous studies (Persico & Meyer 2013). Conversely, floodplain deposits are concentrated around 1000 and 2000 cal yr. BP, corresponding with drought as recorded by the drought index reconstruction (Fig. 3).

Dates for some samples were excluded due to of inbuilt age (i.e. sample age > deposit age). Inbuilt

Figure 2. Left: Sampling for charcoal at a cutbank stratigraphic column along the Gallatin River. This stratigraphy had large channel cobbles topped by floodplain deposits and soil development at the top, indicating a long period of stability (it is unlikely that this surface was abandoned as recently as 1920). Orange flags mark locations of charcoal samples. The charcoal sample that is second from the bottom, "2019BearGal3", has been dated at ~1520 cal yr. BP, in a sandy lens with abundant charcoal of floodplain deposits. This sample is likely from a fire-related flood. Right top: A zoomed-out view of the area surrounding that stratigraphy. Right bottom: A beaver pond deposit near the current waterline on the West Fork Blacktail Creek. The root-filled layer may be an old beaver dam. The lowest orange flag denotes a beaver-chewed wood sample, "2019WBTBP4", dated at ~50 cal yr. BP. Although the beaver pond deposit is from historic times, we believe that it does not represent the age of the stratigraphy it was found in, as beavers may have placed sticks at variable heights across the channel.

age is identified where samples collected higher in the stratigraphy had older ages than those lower in the stratigraphy. These samples likely represented redeposited material from older deposits. Even for other samples, it is possible that the age represents older charcoal redeposited from earlier deposits or a very old tree. Care was taken to choose angular charcoal pieces that were less likely to be redeposited, but this is a potential source of error in ages.

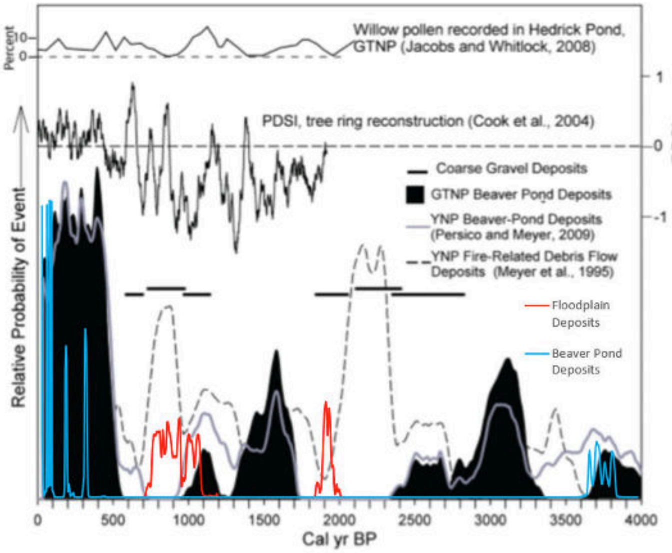

Figure 3. Age probabilities of radiocarbon samples in floodplain deposits (red lines) or beaver pond deposits (blue lines) compared with records of drought, willow prevalence, and ages of fire-related and beaver-related deposits from Persico & Meyer 2013.

DISCUSSION AND CONCLUSION

The stratigraphic record in the Northern Range of YNP provides evidence for correlations between climate, beaver activity, and stream morphology over the last 7000 years. Beaver activity in this broad area is more prevalent during cooler, wetter periods. Conversely, most floodplain deposition occurs during warmer, drier periods. The long-term relationship between climate and YNP ecosystems, combined with the thick A-horizons that take time to develop after incision (Fig. 2), make the theory of recent incision due to a trophic cascade after wolf removal alone dominating ecosystem change unlikely.

Three samples provide evidence for general timing of stream processes on East Fork Blacktail. From Persico and Meyer (2009), radiocarbon dates at the surface of a laterally continuous, high fluvial terrace date to around 3300 cal. yr. BP, dating the end of a period of infill and floodplain aggradation. A sample dated from an inset slip-off terrace at 1450 cal yr. BP documents timing of incision. 2019EBT16, from ~860 cal. yr. BP, which was found 10 centimeters below the modern channel bed, suggests incision occurred long before the historical period.

The timing of fluvial processes in the greater Yellowstone ecosystem are controlled by millennial-scale climatic variability; beaver pond deposits are more prevalent in wetter, less drought-prone periods (Persico and Meyer, 2013). Most of the beaver pond deposits in this study have similar timing patterns—particularly the last 500 years and between 3600 and 4800 cal. year BP (Table 1). The overlap suggests that regional-scale climate variability, rather than localized impacts of wolves in the Northern Range alone, are a control on fluvial processes including beaver-pond aggradation. Beaver pond deposit ages also closely correspond to ages from Persico and Meyer, 2009, which is focused on other Yellowstone Northern Range streams (Fig. 3). Additionally, 2019WBT4, a beaver pond deposit in the incised terrace surface of the West Fork of Blacktail Deer Creek was modern, indicating that stream incision occurred prior to 1950 and beavers have been active on WBT since 1950 despite the absence of wolves.

Terrace formation coincides with cool periods during the Holocene, as higher discharges and lower sediment loads result in incision (Meyer, Wells, & Jull 1995). Conversely, variable and intense precipitation occurs during warm periods, combined with fires, which result in fire-related floods and alluvial fan deposition (Meyer et al. 1995). This same mechanism could produce floodplain deposits with charcoal. We found charcoal ages in floodplain deposits to be concentrated within the Medieval Warm Period (700-1100 cal yr. BP) and between 1800 and 2000 cal yr, BP, which corresponds with ages of fire-related debris flows and sedimentation in Meyer et al. 1995, and with periods of drought (Fig. 3). For example, sample 2019EBT16 is a charcoal sample found in a very fine-grained floodplain deposit 10 centimeters beneath the modern channel bottom dated at ~860 cal yr. BP. It represents floodplain deposition during a warm period, and also indicates overall infill of channels since this period. Similarly, 2019WBTstratinset, dated at 790 cal yr. BP, also falls within this warm period and represents infill of a paleochannel inset in a higher kame surface. This supports the idea that floodplain deposition occurs in warmer, drier periods.

The prevalence of both beaver pond deposits and potentially fire-related floodplain deposits in the stratigraphic record of the Northern Range of YNP and the broader Greater Yellowstone Ecosystem emphasizes the importance of both processes over the late Holocene. A state with abundant beaver, wolves, and large willows, and reduced elk populations that occurred during the early 1900s is not necessarily the default. Rather, climate changes may dictate varied megafauna populations and stream conditions.

The history of beaver activity and stream morphology over the last 7000 years in Yellowstone National Park is complicated by variable underlying geology, many climatic changes, and complex ecosystem dynamics. A selection of radiocarbon dates along a large swath of the Northern Range is insufficient to confidently describe thousands of years of history, but nonetheless suggest a story more complex than the trophic cascade theory. Rather, our results supported our hypothesis that beaver activity corresponds to wetter periods, while floodplain deposits correspond to drier periods.

Climate models, such as the Great Plains Regional Climate Trends report from the United States Global Change Research Program (Kunkel et al. 2013), predict that Yellowstone and the surrounding areas will experience wetter winters and hotter seasons within the next 20+ years. Beaver health is reduced during warmer spring conditions and wetter falls (Campbell et al. 2013), so populations may be impacted by continued warming. Additionally, they are limited by a maximum flow that they can maintain their dams in (Persico & Meyers, 2009), so extreme flooding during higher-than-average spring flooding would potentially cause more dam failures resulting in less sustainable beaver habitat. More broadly, if climate is a significant driver of ecosystem changes in Yellowstone, there may be large alterations to the ecosystem balance in the future.

ACKNOWLEDGEMENTS

This material is based upon work supported by the Keck Geology Consortium and the National Science Foundation under Grant No. 1659322. Many thanks to Dr. Lyman Persico, the primary investigator and advisor for this project, for coordinating grants, permitting, and data collection, along with invaluable assistance in interpretation of the data. Additionally, I would like to recognize Dr. David Harbor as a secondary advisor and Eliza Van Wetter, Trent Foky, April Phinney, and Alice Hinzmann for data collection assistance in Yellowstone.

REFERENCES

Beschta, R. L. & Ripple, W. J. (2018). Can large carnivores change streams via a trophic cascade? Ecohydrology, 1-13.

Campbell, R. D., Newman, C., Macdonald, D. W., and Rosell, F. (2013). Proximate weather patterns and spring green-up phenology effect Eurasian beaver (Castor fiber) body mass and reproductive success: the implications of climate change and topography. Global Change Biology, 19: 1311-1324. doi: 10.1111/gcb.12114

Chadde, S. W. and C. E. Kay (1991). Tall-willow communities on Yellowstone's Northern Range: A test of the "natural-regulation" paradigm. The Greater Yellowstone Ecosystem. R. B. Keiter and M. S. Boyce. Binghamton, Yale University Press: 231-263.

Ford, A. T. and J. R. Goheen (2015). "Trophic Cascades by Large Carnivores: A Case for Strong Inference and Mechanism." Trends in Ecology & Evolution 30(12): 725-735.

Gray, S. T., Graumlich, L. J., & Betancourt, J. L. (2007). Annual precipitation in the Yellowstone National Park region since AD 1173. Quaternary Research, 68:18-27.

Kauffman, M. J., et al. (2010). "Are wolves saving Yellowstone's aspen? A landscape-level test of a behaviorally mediated trophic cascade." Ecology 91(9): 2742-2755.

Keiter, R. B. & Boyce, M. T. (1991). The Greater Yellowstone Ecosystem: Redefining America's Wilderness Heritage. Yale University Press.

Kunkel, K.E., L.E. Stevens, S.E. Stevens, L. Sun, E. Janssen, D. Wuebbles, M.C. Kruk, D.P. Thomas, M. Shulski, N. Umphlett, K. Hubbard, K. Robbins, L. Romolo, A. Akyuz, T. Pathak, T. Bergantino, and J.G. Dobson. (2013). Regional Climate Trends and Scenarios for the U.S. National Climate Assessment. Part 4. Climate of the U.S. Great Plains, NOAA Technical Report NESDIS 142-4, 82 pp.

Legleiter, C., et al. (2003). "Fluvial response a decade after wildfire in the northern Yellowstone ecosystem: a spatially explicit analysis." Geomorphology 54(3-4): 119-136.

Marshall, K.N., Hobbs, N.T., and Cooper, D.J., 2013, Stream hydrology limits recovery of riparian ecosystems after wolf reintroduction: Proceedings of the Royal Society B: Biological Sciences, v. 280, p. 20122977, doi:10.1098/rspb.2012.2977.

Meyer, G. A., Wells, S. G., & Jull, A. J. T. (1995). Fire and alluvial chronology in Yellowstone National Park: Climatic and intrinsic controls on Holocene geomorphic processes. Geological Society of America Bulletin, 1211-1230.

Persico, L. & Meyer, G. (2009). Holocene beaver damming, fluvial geomorphology, and climate in Yellowstone National Park, Wyoming. Quaternary Research, 340-353.

Persico, L. & Meyer, G. (2013). Natural and historical variability in fluvial processes, beaver activity, and climate in the Greater Yellowstone Ecosystem. Earth Surface Processes and Landforms, 38:728-750.

Peterson, R. O., et al. (2014). Trophic Cascades in a Multicausal World: Isle Royale and Yellowstone. Annual Review of Ecology, Evolution, and Systematics. Palo Alto, Annual Reviews. 45: 325-+.

Pierce, K. L. (1979). History and dynamics of glaciation in the northern Yellowstone National Park area. Professional Paper.

Ripple, W. J. & Beschta, R. L. (2012). Trophic cascades in Yellowstone: the first 15 years after wolf reintroduction. Biological Conservation, 145:205-213.

Stuiver, M., Reimer, P.J., and Reimer, R.W., 2020, CALIB 7.1 [WWW program] at http://calib.org, accessed 2020-3-11

Telford, R. J., et al. (2004). "The intercept is a poor estimate of a calibrated radiocarbon age." The Holocene 14(2): 296-298.

Wolf, E. C., Cooper, D. J., & Hobbs, N. T. (2007). Hydrologic regime and herbivory stabilize and alternative state in Yellowstone National Park. Ecological Applications, 17(6): 1572-1587.

Yellowstone National Park (1997). Yellowstone's Northern Range: Complexity and Change in a Wildland Ecosystem. Mammoth Hot Springs, National Park Service.

Beschta, R. L., and Ripple, W. J., 2006, River channel dynamics following extirpation of wolves in northwestern Yellowstone National Park, USA: Earth Surface Processes and Landforms, v. 31, p. 1525-1539.

Beschta, R. L., and Ripple, W. J., 2019, Can large carnivores change streams via a trophic cascade?: Ecohydrology, v. 12, doi: 10.1002/eco.2048

Kay, C. E., 1997, Viewpoint: Ungulate herbivory, willows, and political ecology in Yellowstone: Journal of Range Management, v. 50, p. 139-145.

Leopold, L. B., Wolman, M. G., and Miller, J. P.

(1964). Fluvial processes in geomorphology: W. H. Freeman and Company, San Francisco, California.

Parrett, C., and Johnson, D. R., 2004, Methods for Estimating Flood Frequency in Montana Based on Data through Water Year 1998: U.S. Geological Survey Water-Resources Investigation Report 03-4308, 99 p.

Pierce, K. L. (1979). History and dynamics of glaciation in the northern Yellowstone National Park area. Professional Paper.

Ripple, W. J., and Beschta, R. L., 2012, Trophic cascades in Yellowstone: The first 15 years after wolf reintroduction: Biological Conservation, v. 145, p. 205-213.

Wolf, E. C., Cooper, D. J., and Hobbs, N. T., 2007, Hydrologic regime and herbivory stabilize an alternative state in Yellowstone National Park: Ecological Applications, v. 17, p. 1572-1587.

KECK Geology Consortium
Learning Science Through Research
Published by the Keck Geology Consortium
Short Contributions
Keck Geology Consortium
Volume 33
May 2020
doi: 10.18277/AKRSG.2020.33.21

GEOMORPHIC CONTROLS ON HYDRAULIC PROCESSES OF BLACKTAIL DEER CREEK, YELLOWSTONE NATIONAL PARK

APRIL I. PHINNEY, Wheaton College (IL)
Research Advisor: Andrew J. Luhmann

INTRODUCTION

The Greater Yellowstone Ecosystem spans 22 million acres of national park, national forest, national wildlife refuge, and BLM land in Wyoming, Montana, and Idaho ("What is the Greater Yellowstone Ecosystem?," n.d.). The GYE is home to the largest concentration of wildlife in the 48 contiguous states (Chan et al., 2016). With the protected Yellowstone National Park at its heart, it is a key location for ecosystem research. Trophic cascade theory is an ecologic model explored here. It predicts that altering one ecosystem element can result in system-wide change; even seemingly unrelated ecosystem factors are closely connected through a chain of cause and effect relationships (Herendeen, 1995).

In Greater Yellowstone, some research has employed trophic cascade theory to understand how changes in the wolf population have initiated widespread ecological effects including potential impacts to the physical habitat of streams. The eradication of wolves in the early 20th century led to increased elk populations and their resultant browsing of riparian vegetation (Kay, 1997; Ripple and Beschta, 2003). With reduced aspen and willow branches to construct dams, beavers moved to larger streams and crafted bank burrows. Beaver dams that may have historically pooled water to form shallow, wide, regularly inundated floodplains (Gurnell, 1998; Polvi and Wohl, 2011; Persico and Meyer, 2012; Giriat, 2016) fell into disrepair and eventually broke up during high discharge flood events (Butler and Malanson, 2005). As dams and ponds were eradicated, stream slope increased causing incision into the previous floodplain (Wolf et. al., 2007; Ripple and Beschta, 2017). The resulting deep, wide channels prevented overbank flooding and instead developed small inset floodplains flanking river flow within the steep, newly formed channel banks (Beschta and Ripple, 2006, 2019).

In order to better characterize channel geometries and their controls, this study investigated what surfaces flood at various discharges. Since predicting bank-full discharges often requires more nuanced study than field observations (Knighton, 1998), detailed cross section topography surveys were collected to create hydraulic models of inundation depths and lateral extent along five stream reaches. We explored if surfaces on the valley floor are inundated during high frequency flood events. We also compared flooding along different stream sections and considered other possible controls (stream migration, bank collapse, alluvial fans, and stream discharge) on valley floor inundation. Ultimately, we modeled floodplain inundation as a means to understand Blacktail Deer Creek's complex historic morphology and explored the role that beaver dam removal (and trophic cascade theory by extension) may have played.

STUDY AREA

Blacktail Deer Creek consists of two prominent tributaries, the west and east forks, which join south of Grand Loop Road. On the Blacktail Deer plateau the stream network is superimposed on kame terraces and outwash channels from the Pinedale glaciation (22-15 ka (Licciardi and Pierce, 2018). Current stream flow is confined within the bottom of these outwash channels for river reaches 4EF, 3EF, and 2EF (Fig. 1). Along this region, the east fork meanders through valley fill deposits alternating from deep pools to

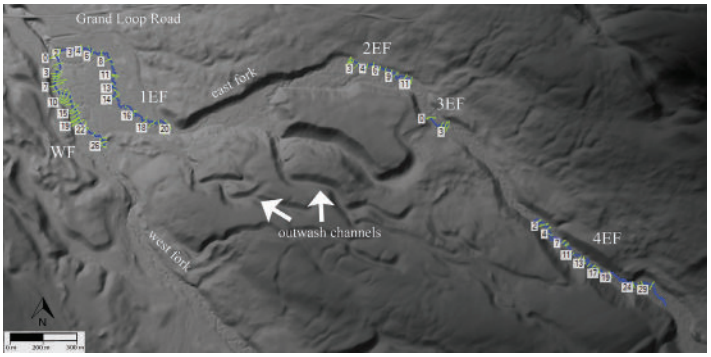

Figure 1. Overview of river reaches with cross sections.

riffle sequences. Both east and west tributaries exit restrictive outwash channels to meander across a gently sloping alluvial fan overlaying kame terrace deposits (reaches 1EF and WF). 1EF alternates between muddy pools along meander bends and shallow riffle sections lined by small willows. The west fork is faster flowing with cobbles, gentle meanders, larger willows, and wider steep channels.

METHODS

To characterize the floodplain inundation of Blacktail Deer Creek, we simulated stream geometry and discharge by integrating RTK GPS measurements and LiDAR DEM imagery. Historic stream gage data and calculated flood recurrence intervals provided representative stream discharges that were used to develop inundation maps.

Field Data Collection

GPS-surveyed stream cross sections along the east and west forks of Blacktail Deer Creek complemented DEM datasets by providing elevation data among willows and beneath water flow. Along the west fork, we gathered cross sections extending upstream from the east fork confluence. On the east fork, we collected cross section coordinates along four reaches (1EF, 2EF, 3EF, and 4EF) representative of changing geomorphic surroundings (Fig. 1).

Real-time kinematic (RTK) GPS connections, where a hand-held GPS rover referenced a base station with precise satellite coordinates, provided GPS coordinates with 13 cm accuracy in dense foliage. We spaced cross sections at approximately 20-meter intervals, selecting locations accessible between willows and representative of general flow (meander bends, straight sections, and alternating riffle and pool segments). Data points included locations of elevation change along the banks, water surface, channel edge, channel elevation changes, and thalweg. Water levels represented low August discharges.

Estimating Peak Discharges

Discharge values were derived from both measured and modeled data. Historic stream gage data from the U.S. Geological Survey provided peak discharges from 1937-1941 for the east fork (2020a) and 1937-1946 and 1988-1993 for the west fork (2020b). A regression model calibrated for northwestern Wyoming streams calculated representative flows for various flood recurrence intervals (Miller, 2003):

$$Q_{\mathrm{T}} = K(A^{a})\left(\left(\frac{E-3{,}000}{1{,}000}\right)^{e}\right)((L-100)^{l})$$

where Q_T is discharge at a recurrence interval of T years (cubic feet per meter), K is a regression constant, A is watershed area (square miles), E is average basin elevation (feet), L is longitude (decimal degrees), and a, e, and l are regression coefficients (Table 1). We generated GIS polygons of the east and west fork watersheds to calculate basin areas of 9 square miles and 15 square miles, respectively. The GIS zonal statistics tool linked the watershed areas to the DEM raster to calculate mean basin elevations of 727.6 m for the west fork and 714.5 m for the east fork. The average longitude was 110.589675º. We utilized 2 and 10-year floods to characterize high recurrence interval flood discharges.

Hydraulic Modeling of Flood Discharges

LiDAR DEM data gathered using the point tool in ArcMap complemented field GPS cross-sectional data, which provided accurate coordinates where the LiDAR DEM could not penetrate foliage and water. GPS and DEM points were then integrated as single Excel files for each of the four river reaches.

The Hydrologic Engineering Center’s River Analysis System (HEC-RAS) was used to generate stream flow and inundation models from this cross-sectional data. We measured distance in meters between cross-

Table 1. Calculation of flood peak discharges

Flood Recurrence Interval (year)	West Fork Q m^3/s	East Fork Q m^3/s
1.5	2.4	1.4
2	3.0	1.8
5	5.0	3.1
10	6.4	4.0
25	8.3	5.3
50	9.6	6.3
100	11.1	7.3
500	14.9	10.0

sections for the left bank, channel, and right bank with the RAS ruler. Manning's n roughness values for the floodplains and channel (Table 2), which estimated the frictional impact of vegetation and rocks upon water flow, were selected according to the guidelines outlined by Chow (1959) and Arcement and Schneider (1989). Bank edges were estimated as data points closest to the waterline of a 2-year flood modeled by steady flow analysis. Levies were inserted to prevent simulated flows from inundating paleochannels and other low elevation regions before first overtopping channel banks. Steady flow analysis simulated flow as an unchanging discharge along the stream utilizing our regression values and available gage data. Manning's equation approximated characteristic upstream and downstream flow through the normal depth option in HEC-RAS. To calculate this value, we estimated the friction slope (Brunner and Gee, n.d.) as the change in mid-channel elevations over the change in total horizontal displacement for each cross-section reach (Table 2). The critical depth model was calculated as a mixed regime flow (Goodell, 2011) to account for changes between stable subcritical flow along gentle slopes and turbulent supercritical flow corresponding with steeper slopes (Ponce, n.d.).

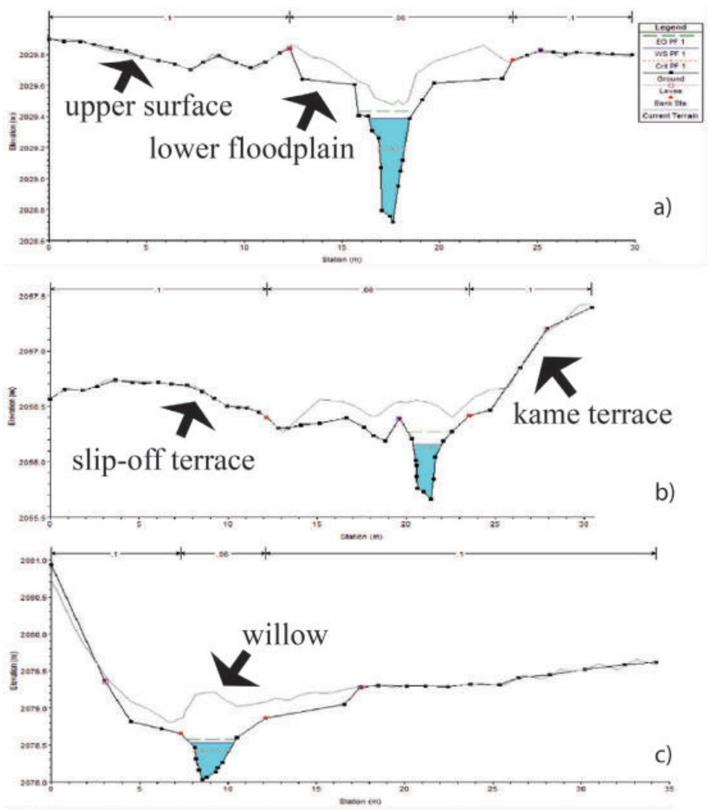

Figure 2. Cross sections with a 0.7 m2/s flood displaying (a) characteristic alluvial cross section (1EF 6) with a well-defined lower floodplain and upper surface, (b) cross section 2EF 5 displaying a stepped slip-off terrace on the left bank and a steep kame terrace on the right bank characteristic of reaches 4EF, 3EF, and 2EF, and (c) light gray DEM line captures a willow in the middle of the actual channel of cross section 4EF 1. Legend names represent the following: EG PF 1 is the energy gradeline peak flow, WS PF 1 is the water surface peak flow, Crit PF 1 is the critical peak flow, Ground is the ground elevation, Levee is the bank levee, Bank Sta is the cross section number, and Current Terrain is the LiDAR DEM elevation.

Table 2. Values used for HEC-RAS hydrologic modeling

	WF	1EF	2EF	3EF
Floodplain Manning's n (unitless)	0.12	0.1		
Channel Manning's n (unitless)	0.05	0.06		
Reach Slope (unitless)	0.02	0.023	0.008	0.024

Various discharge values on RAS-Mapper were then simulated to visually depict the extent of floodplain inundation. After drawing the river path to specify which flow paths the river should follow between cross-sections, we generated a new background terrain map combining the detailed LiDAR-DEM with our interpolated cross-sectional stream geometry to eliminate willow elevations (Fig. 2c). The resulting maps depict the extent of inundation for 2-, 10-, and 100-year floods along the west fork, and <1.5- (i.e., the maximum recorded discharge of 0.7 m^3/s), 10- and 100-year floods for the east fork.

RESULTS

Stream Discharge Values

The limited historic stream gage data and calculated regression discharge values provided an estimate of flood recurrence intervals. Our east fork regression predictions (Table 1) averaged 37% greater than Beschta and Ripple's (2019) values. Our calculated

1.5-year discharge was 100% larger than the maximum stream gage flood (0.7 m^3/s) measured in four years (1937-1941) (U. S. Geological Survey, 2020a). However, the same discharge event along the Yellowstone River at Corwin Springs was also smaller than a 1.5-year recurrence interval (U. S. Geological Survey, 2020c). Stream regressions for the west fork align at 8% higher than Beschta and Ripple's (2019) values. According to our calculations, the maximum stream gage prediction (4.0 m^3/s) for 1937-1946 (U. S. Geological Survey, 2020b) was a 2- to 5-year flood, which compares closely to the Yellowstone River's corresponding 2-year flood (U. S. Geological Survey, 2020c). The maximum 5.1 m^3/s discharge (2020b) had a 5-year recurrence interval, which aligns with the same event creating a 10-year flood along the Yellowstone River (2020c). Since our regression values along the east fork we high, we incorporated the maximum east fork gage discharge of 0.7 m^3/s with 2-, 10-, and 100-year discharges in the inundation maps.

Inundation Modeling

Reaches 4EF, 3EF, and 2EF inundated a similar region surrounding the channel (Fig. 3). Channel geometries for a 0.7 m^3/s discharge varied from 0.38-1.1 m deep and 0.8-7.5 m wide as they altered between deep, steep channels to channels of similar depth and width. Floodplains occurred at a variety of heights ranging from 0.5 to 1.6 m above the channel base.

1EF demonstrated two characteristic reaches with floodplain inundation and channel depth decreasing and channel width increasing near the confluence (Fig. 3). The upper channel of 1EF (cross sections 20 to 15) was 0.4-0.9 m deep and 1.3-2.8 m wide at a 0.7 m^3/s discharge and did not have consistent floodplain levels. Paleochannels now separated by fan/terrace surfaces radiated from this upper extent and did not inundate. The middle section (cross sections 14-4) had channels 0.4-0.7 m deep and 1.8-3.6 m wide. A small surface 0.7-1.3 m above the channel base inundated with a 5-year flood, while the higher surface (0.9-1.2 m above the channel) inundated with a 50-year recurrence (Fig. 2a). Bank collapse was observed as a common feature along meander bends. Downstream (cross sections 3 to 0), channels were shallower (0.3-0.6 m) and wider (2.8-4.2 m) at a 0.7 m^3/s flow, and had extremely uneven channel beds from underlying kame terrace boulders. Two surfaces occurred at similar 0.8-1.2 m and 1.0-1.4 m heights above the channel bed. However, the lower surface required larger 10- to 25-yr floods to inundate, and the upper surface was not inundated even a by a

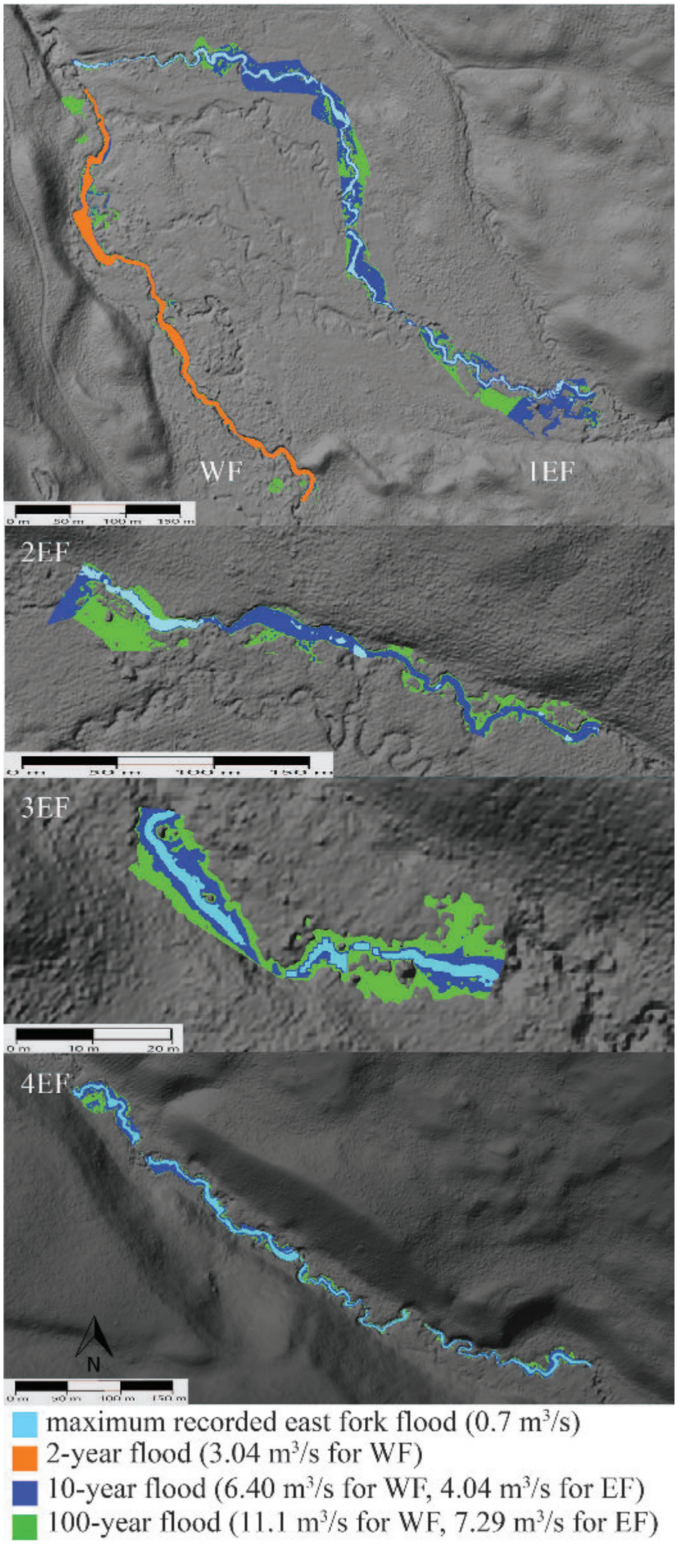

Figure 3. Blacktail Deer Creek inundation at different discharges.

500-year flood. The inundation map (Fig. 3) similarly demonstrated that flooding is widespread between cross sections 15-5 (flood waters would have extended beyond the edge of our cross-section geometries had we not created artificial channel edges) and decreased between cross sections 3-0.

The west fork did not widely flood; 2-, 10-, and 100-year floods were generally confined within steep channel banks (Fig. 3). Channel geometry was an inconsistent 0.3-1.0 m deep and 4.0-14.4 m wide for a 2-year flood. Numerous dry or swampy paleochannels lay alongside the stream that did not activate during flooding events.

DISCUSSION

Much of our research assumes that flood recurrence intervals are predictable measures of bank-full discharge. We recognize that actual flooding can be more variable. Particularly, predictions for 1.5-year bank-full channels may flood less frequently (Williams, 1978). Our data functions best as a general comparison between various stream sections with the same stream controls instead of as precise predictions of future inundations at specific locations.

Beschta and Ripple's (2019) interpretation that floodplain shape and inundation was characterized by the former presence and recent absence of beavers should impact various reaches of the river similarly. Elk populate the entire region, equally browsing foliage along both reaches of the creek. Gnawed twigs in the sedimentary record and current beaver dams indicate that beavers are active along both the east and west forks. Trophic controls remain the same between all reaches, but channel geometry and floodplain inundation vary significantly between the sections of Blacktail Deer Creek. Geologic and geomorphic controls must be considered to adequately explain for the changing river hydraulics.

Stream migration, impacted by underlying kame and valley fill deposits, may account for key floodplain characteristics of 4EF, 3EF, and 2EF. The lowest surfaces did not form as inset-floodplains following recent stream incision since these surfaces vary in height and inundate at different discharges. What Beschta and Ripple (2019) identified as the higher historic floodplain exhibits similar variation. Instead of two clear floodplains, multiple notched levels gently slope towards the current channel and represent slip-off terraces (Fig. 2b). Trapped between unerodable kame terraces, the upper east fork laterally migrated and gradually carved multiple channels.

Unlike the three upstream east fork reaches, 1EF exhibits two inundation surfaces (Fig. 2a) that correspond to the historic and inset floodplains that Beschta and Ripple (2019) describe. Field observations indicate some of these lower surfaces originated as bank failures. As the meandering river incised fine alluvial fan sediments, cut banks collapsed into the channel to form lower inundation surfaces.1EF floods differently along various sections of the alluvial fan. Above the confluence, the east fork drops to match the elevation of the west fork resulting in headward fan erosion, increased channel slope, and reduced floodplain inundation. Large boulders indicate that the stream has incised to meet the underlying kame terrace deposit.

Floodplain inundations also significantly differ between the two river tributaries. Although the west fork is pinned between kame terraces similar to 4EF, 3EF, and 2EF, the west fork floods less land. The west fork's higher discharge effectively transports sediment downstream and incises steep banks that prevent flooding.

The variety of Blacktail Deer Creek's channel geometries indicate an old, complex floodplain history shaped by a variety of geomorphic controls. The Pinedale glaciation covered Yellowstone's Northern Range with large kame terraces (Licciardi and Pierce, 2018). Melting glaciers released large quantities of sediment that filled outwash channels with aggrading river terraces and alluvial fans from the early to late Holocene. Around 3.3 ka, glacial sediment transport decreased according to terrace charcoal dating (Persico and Meyer, 2009). Blacktail Deer Creek, constrained between kame terraces began to incise the Holocene valley fill deposits to create various slip-off terraces. The lower alluvial fan continued to slowly aggrade to the present day.

CONCLUSIONS

Previous explanations of channel characteristics that extend trophic cascade theory to stream morphology cannot adequately explain changes in channel geometry and floodplain inundation along Blacktail Deer Creek. While trophic cascade-related events may impact the physical morphology of channels, multiple additional geologic and geomorphic controls determine channel and floodplain geometries more significantly than the absence of beaver dams. Since the late Pleistocene, stream migration, alluvial deposition, bank collapse, and stream discharge have gradually shaped Blacktail Deer Creek.

ACKNOWLEDGEMENTS

This material is based upon work supported by the Keck Geology Consortium and the National Science Foundation under Grant No. 1659322. Thank you, Lyman Persico for envisioning and guiding this project; Andrew Luhmann for providing encouragement and mentorship along the way; and Alice Hinzmann, Chantal Iosso, Eliza Van Wetter, and Trent Foky for being enthusiastic field comrades.

REFERENCES

Arcement, G. and Schneider, V., 1989, Guide for selecting manning's roughness coefficients for natural channels and flood plains: U.S. Geological Survey Water-Supply Paper 2339.

Beschta, R., and Ripple, W., 2019, Can large carnivores change streams via a trophic cascade?, Ecohydrology, v. 12., p. e2048.

Beschta, R., and Ripple, W., 2006, River channel dynamics following extirpation of wolves in northwestern Yellowstone National Park, USA: Earth Surface Processes and Landforms, v. 31, p. 1524–1539.

Brunner, G., and Gee, M., n.d., Boundary and Initial Conditions: NOAA.

Butler, D. and Malanson G., 2005, The geomorphic influences of beaver dams and failures of beaver dams: Geomorphology, v. 71, p. 48-60.

Chan, L., Nelson, M., Kruger, L., and Klein, B., 2016, Greater Yellowstone Ecosystem: National Park Service.

Chow, V., 1959, Open-channel hydraulics: New York, McGraw-Hill, McGraw-Hill civil engineering series.

Giriat, D., Gorczyca, E., and Sobucki, M., 2016, Beaver ponds' impact on fluvial processes (Beskid Niski Mts., SE Poland): Science of the Total Environment, v. 544, p. 339–353.

Goodell, C., 2011, Mixed flow regime options-LPI method: The RAS Solution.

Gurnell, A., 1998, The hydrogeomorphological effects of beaver dam-building activity: Progress in Physical Geography, v. 22, p. 167–189.

Herendeen, R.A., 1995, A unified quantitative approach to trophic cascade and bottom-up: top-down hypotheses: v. 176, p. 13–26.

Kay, C., 1997, Viewpoint: Ungulate herbivory, willows, and political ecology in Yellowstone: Journal of Range Management, v. 50, p. 139–145.

Knighton, D., 1998, Fluvial forms and processes: a new perspective: London, Oxford University Press.

Licciardi, J., and Pierce, K., 2018, History and dynamics of the Greater Yellowstone Glacial System during the last two glaciations: v. 200, p. 1–33.

Miller, K.A., 2003, Peak-Flow characteristics of Wyoming streams: USGS Water-Resources Investigations Report 03–4107.

Persico, L., and Meyer, G., 2009, Holocene beaver damming, fluvial geomorphology, and climate in Yellowstone National Park, Wyoming: Quaternary Research, v. 71, p. 340–353.

Persico, L., and Meyer, G., 2012, Natural and historical variability in fluvial processes, beaver activity, and climate in the Greater Yellowstone Ecosystem: Earth Surface Processes and Landforms, v. 38, p. 728-750.

Polvi, L., and Wohl, E., 2012, The beaver meadow complex revisited—the role of beavers in post-glacial floodplain development: Earth Surface Processes and Landforms, v. 37, p. 332–346.

Ponce, V., Steady vs unsteady flow with HEC-RAS, access February 17, 2020, at URL http://ponce.sdsu.edu/unsteady_flow_with_hec_ras.html.s

Ripple, W., and Beschta, R., 2012, Trophic cascades in Yellowstone: The first 15 years after wolf reintroduction: Biological Conservation, v. 145, p. 205–213.

Ripple, W., and Beschta, R., 2003, Wolf reintroduction, predation risk, and cottonwood recovery in Yellowstone National Park: Forest Ecology and Management, v. 184, p. 299–313.

U.S. Geological Survey, 2020a, National Water Information System data available on the World Wide Web (USGS Water Data for the Nation), accessed April 27, 2020, at URL https://waterdata.usgs.gov/nwis/dv/?referred_module=sw&site_no=06188500

U.S. Geological Survey, 2020b, National Water Information System data available on the World Wide Web (USGS Water Data for the Nation), accessed April 27, 2020, at URL https://waterdata.usgs.gov/nwis/inventory/?site_no=06189000.

U.S. Geological Survey, 2020c, National Water Information System data available on the World Wide Web (USGS Water Data for the Nation), accessed April 27, 2020, at URL https://waterdata.usgs.gov/nwis/uv?site_no=06191500.

Williams, G., 1978, Bank-full discharge of rivers: Water Resources, v. 14(6), 1141-1154.

What is the Greater Yellowstone Ecosystem?, n.d., Yellowstone Wildlife Sanctuary, accessed March 25, 2020, at https://www.yellowstonewildlifesanctuary.org/the-ecosystem.

Wolf, E., Cooper, D., and Hobbs, N., 2007, Hydrologic regime and herbivory stabilize an alternative state in Yellowstone National Park: Ecological Applications, v. 17, p. 1572–1587.

KECK Geology Consortium
Learning Science Through Research
Published by the Keck Geology Consortium
Short Contributions
Keck Geology Consortium
Volume 33
May 2020
doi: 10.18277/AKRSG.2020.33.22

EVERY PEBBLE COUNTS: RECONSTRUCTING THE FLUVIAL HISTORY OF BLACKTAIL DEER CREEK IN THE NORTHERN RANGE OF YELLOWSTONE NATIONAL PARK

ELIZA VAN WETTER, Whitman College
Research Advisor: Lyman Persico

INTRODUCTION

In 1872, Yellowstone National Park was established as the first ever National Park in the United States. The park has a long history of management strategies that have affected the ecosystem (Haines 1977). A particularly well-studied area of the park is the Northern Range, a ~1,530 km^2 area of relatively low elevation land that is the wintering range of Yellowstone's northern elk herd (Houston 1982, Clark et al. 1999). The impact of management in this ecosystem is subject of much debate (Yellowstone National Park 1997). Among the most controversial of these management practices is the extirpation and eventual reintroduction of wolves (canis lupus) from the ecosystem. In the early 1900s, the management of the park focused on protecting "good animals", primarily grazing ungulates that could be conserved within the park and hunted when they moved outside of the park boundaries. This brand of conservation was heavily encouraged by the hunting industry that realized without protection, there would be fewer animals to hunt (Yellowstone National Park, 1997). Due to this priority, apex predators were killed inside and outside of the park and by the mid 1920s, wolves had been completely removed from the Yellowstone Ecosystem (Chadde, Kay 1991). Following the removal of wolves, elk (cervis elaphus) populations greatly increased causing overgrazing of willow (Salix spp.), aspen (populus tremuloides) and other plant populations (Kay 1997).

Some research suggests that the removal of apex predators has affected stream processes and morphology as part of a widespread trophic cascade initiated by the removal of wolves. The decrease in willows in riparian areas has been suggested to cause destabilization of stream banks causing both channel incision and widening (Beschta, Ripple 2011). Due to this change in channel dimensions, the normal stream flows are less likely to flood the channel in a high frequency flood event, resulting in historic floodplains that are now abandoned (Ripple, Beschta 2018).

There are other factors that influence channel morphology and dynamics besides interactions between willow and streambanks. For example, the size of sediment that makes up the bed material determines channel morphology (Meyer 200) and what size floods are needed to cause channel incision. The size of sediment is an important variable in the dynamics of the stream channel. Sediment size will govern what size flood discharges are required to mobilize the bed material and therefore change the channel shape (Knighton 1998). Larger sediment size requires a greater discharge, which makes streams of this size with large diameter materials generally more stable and unmoving while streams of this size with smaller sediment can be expected to shift shape and location along the floodplain. Less research has focused on the fluvial geomorphic history of the streams and the factors that directly affect channel shape.

Our study is focused on creating a detailed characterization of the bed material of Blacktail Deer Creek by comparing the shear stress generated in various sized, historical floods to the shear stress of the bed material to understand the extent and potential for sediment transport. We aim to reconstruct a more complete understanding of the history of the stream by comparing historical images from the last 80 years.

Figure 1. Researchers in the East Fork of Blacktail Deer Creek measure the diameter of pebbles using a gravelometer. Each person would walk in a zig-zag pattern across the width of the stream until at least 100 pebbles were measured for each section.

We predict that the large clasts in the glacial sediment are too large to be transported by the modern Blacktail Deer Creek. Thus, this creates bed armor that that the stream cannot mobilize. This bed armor prevents net vertical cutting and minimal lateral movement of the channel.

Blacktail Deer Creek is located near the geographic center of the Northern Range where it drains the northern flank of the Washburn Range before eventually flowing into the Yellowstone River. The west and east forks of Blacktail Deer Creek have drainage areas of ~35 km^2 and ~27 km^2, respectively. Blacktail Deer Plateau was glaciated multiple times most recently with the Pinedale glaciation which occurred 30,000-12,000 years ago (Fritz, Thomas 2011, Pierce K.L 1979, Licciardi J.M and Pierce K.L 2008). The Blacktail Deer creek network flows through a series of remnant glacial outwash channels that preserve kame, gravel, till, and Holocene alluvium (Pierce 1979, Fritz, Thomas 2011).

METHODS

Field

On the West Fork of Blacktail Deer Creek (WBT), we focused on classifying the bed material from the confluence to approximately 1.5 km upstream of the confluence (Fig. 1). WBT has very distinct pool and riffle morphology and we divided the reaches of pebble counts by the transition between these characteristic sections. For each pool and riffle we recorded a GPS location from the middle of the section and measured the B-axis diameter of 100 pebbles at each location. The East Fork (EBT) does not possess distinct pool and riffle morphology so instead we divided our reaches by visually assessing when the size of material noticeably changed size or approximately every 10m. On EBT we did not count an entirely continuous section but instead focused on three sections. While doing pebble counts, we focused on randomness of pebble selected and tried to avoid any accidental human bias towards selecting certain rocks over others. All pebbles were measured using a gravelometer as either 2, 2.8,4, 5.6, 8, 11, 16, 22.6, 32, 45, 64, 90, 128, 180 mm. Any pebbles that were larger than 180 mm in diameter, were measured with a ruler.

In addition to pebble counts, we also measured detailed cross sections along both forks of Blacktail Deer Creek in the same locations as the pebble counts. Surveys were performed using RTK GPS with cm-scale accuracy. We captured the cross-sectional profile of the channel approximately every 10m from the confluence upstream—on both forks. We also recorded a longitudinal profile of both forks that thoroughly captured any change in elevation between the upper reaches of each fork and the confluence.

Lab analysis

Pebble measurements were analyzed in Microsoft Excel where we calculated the D50 and D90 value for each reach on both forks. We calculated the critical shear stress needed to mobilize the sediment using the critical shear stress equation (Komar 1988):

$$\tau_t=\theta_t\,(\rho_s-\rho)gD$$

Where: τ_t=threshold flow stress, ρ_s=grain density, ρ=fluid density, g=acceleration of gravity, D=grain diameter.

To understand if Blacktail Deer Creek was able to generate enough shear stress to overcome the values we calculated for the D50, and D90—we calculated the bed shear stresses associated with a 2-year, 10-year and 100-year recurrence interval floods:

$\tau=\gamma DSw$

Where: τ=Bed Shear Stress (N/m^2), γ=Weight Density of Water (N/m^2), D= Average water depth, Sw= Water Surface slope (m/m).

We used GIS to analyze the size variability of bed material. We created a shapefile of the distinct sections where we performed counts. We than joined the pebble count data points to this shape file and color coded each section based on the D50 and D90 values so we could interpret stream wide trends in the distribution and size of bed material. A high-resolution (< 1m) DEM and orthophotograph were also used in the spatial analyses. The maps of the color-coded east and west fork will show if the sediment changes size upstream or downstream.

With the values generated from the previous equations, we compared them to shear values generated from HEC-RAS. In HEC-RAS we used the cross sections we took to model a 300cfs (8.5 cubic meters/sec) which would be approximately a 100-year flood for this stream. This model calculated the shear power in N/m^2 which we compared to the amount of shear stress that would be required to transport the sediment and therefore understand if this size flood would be capable of transporting sediment. HEC-RAS makes these calculations based on specific cross sections, so we matched these cross sections to the location of our pebble counts (Table 1).

Additionally, we analyzed the channel patterns using historic aerial photographs from the USGS in 1954 and 1969. In ArcGIS, we traced the shape of both the East and West fork on these historic images and compared them to an orthophoto from 2018. We compared the historic channel shape to the modern-day channel to better understand if and what type of transformations the stream had undergone since 1950.

RESULTS

The West fork of Blacktail Deer creek has larger average-sized sediment than the East fork with D50 values ranging from 2-180 cm and averaging at 27 cm (Fig. 2). The West fork ranges from 22.6–90 cm and averages at 62 cm. The D90 values of East Fork and West Fork are similar: 111 cm and 153 cm, respectively. Both the East Fork and West Fork show trends of increasing D50 values downstream, however, the D90 values do not show any trends on either fork.

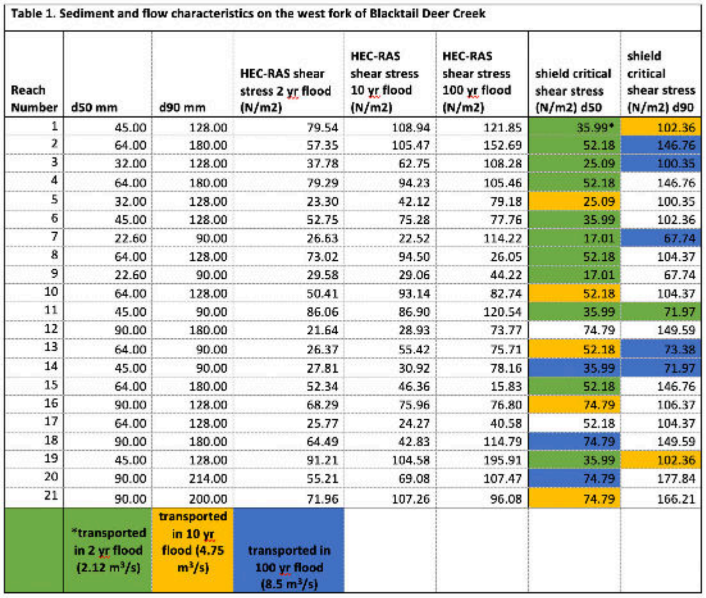

Table 1. Sediment and flow characteristics on the west fork of Blacktail Deer Creek

Reach Number	d50 mm	d90 mm	HEC-RAS shear stress 2 yr flood (N/m2)	HEC-RAS shear stress 10 yr flood (N/m2)	HEC-RAS shear stress 100 yr flood (N/m2)	shield critical shear stress (N/m2) d50	shield critical shear stress (N/m2) d90
1	45.00	128.00	79.54	108.94	121.85	🟩 35.99*	🟨 102.36
2	64.00	180.00	57.35	105.47	152.69	🟩 52.18	🟦 146.76
3	32.00	128.00	37.78	62.75	108.28	🟩 25.09	🟦 100.35
4	64.00	180.00	79.29	94.23	105.46	🟩 52.18	146.76
5	32.00	128.00	23.30	42.12	79.18	🟨 25.09	100.35
6	45.00	128.00	52.75	75.28	77.76	🟩 35.99	102.36
7	22.60	90.00	26.63	22.52	114.22	🟩 17.01	🟦 67.74
8	64.00	128.00	73.02	94.50	26.05	🟩 52.18	104.37
9	22.60	90.00	29.58	29.06	44.22	🟩 17.01	67.74
10	64.00	128.00	50.41	93.14	82.74	🟨 52.18	104.37
11	45.00	90.00	86.06	86.90	120.54	🟩 35.99	🟩 71.97
12	90.00	180.00	21.64	28.93	73.77	74.79	149.59
13	64.00	90.00	26.37	55.42	75.71	🟨 52.18	🟦 73.38
14	45.00	90.00	27.81	30.92	78.16	🟦 35.99	🟦 71.97
15	64.00	180.00	52.34	46.36	15.83	🟩 52.18	146.76
16	90.00	128.00	68.29	75.96	76.80	🟨 74.79	106.37
17	64.00	128.00	25.77	24.27	40.58	52.18	104.37
18	90.00	180.00	64.49	42.83	114.79	🟦 74.79	149.59
19	45.00	128.00	91.21	104.58	195.91	🟩 35.99	🟨 102.36
20	90.00	214.00	55.21	69.08	107.47	🟦 74.79	177.84
21	90.00	200.00	71.96	107.26	96.08	🟨 74.79	166.21
🟩	🟩 *transported in 2 yr flood (2.12 m³/s)	🟨 transported in 10 yr flood (4.75 m³/s)	🟦 transported in 100 yr flood (8.5 m³/s)				

For the West Fork of Blacktail Deer Creek, the shields critical shear stress ranged from 17.65 N/m^2 to 70.30 N/m^2. The East Fork shields critical shear stress ranged from 1.56 N/m^2 to 99.97 N/m^2. The HEC-RAS values from the West Fork ranged from 28.56 N/m^2 to 295.10 N/m^2. After comparing the HEC-RAS modeled flood sizes of the West Fork we found that 52% of the reaches had their D50 pebbles transported in the 2-year flood, an additional 24% of reaches had D50s transported by a 10-year flood, 14% more of the reaches by the 100-year flood and 10% of the reaches had no D50s transported. For the D90 sediment, 5% of the reaches had sediment that was transported by the 2-year flood, an additional 14% of reaches had sediment transported in the 10-year flood, 19% of reaches had sediment that only became transported in a 100-year flood while 62% of all the reaches had D90 sediment that wasn't transported by any size flood (Table 1).

Analysis of the aerial photographs from 1954, 1969 and 2018 showed a relatively consistent channel shape. There was no noticeable change in channels shape between 1954 and 1969. Sometime between 1969 to 2018, the West Fork had four documented avulsions when the stream jumped its channels and

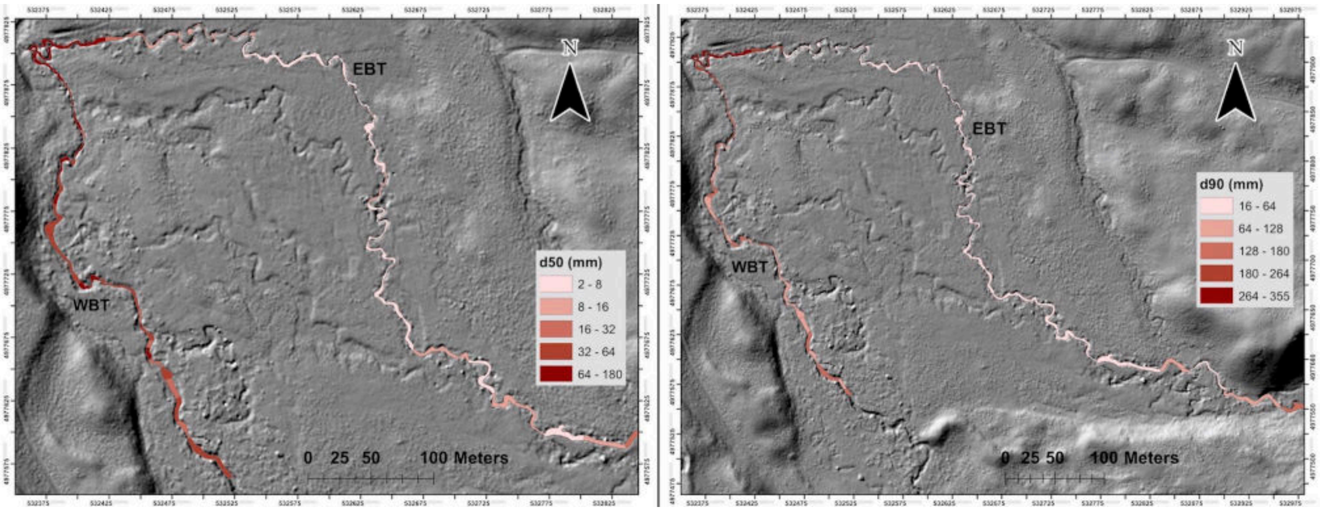

Figure 2. A) D50 values of the confluence and upstream on both WBT and EBT. The lighter color connotes smaller grain size which can be seen concentrated upstream on the East Fork. B) D90 values of the same area. The grain size in both forks becomes coarser near the confluence and the East Fork is finer overall.

cut off a meander while the East Fork had three of these same sized movements. From these photos, the channels have remained consistently the same shape with the exception of the few meter-long sections where avulsions have occurred. There have been channel avulsions in both forks since the 1950s (Figure 3).

DISCUSSION AND CONCLUSION

Bed shear stresses compared with the critical shear stress of the D50 and D90-sized pebbles in the West fork are used to determine if channel bed sediment is mobilized during different size floods. A 2-year flood is the typical bankfull flood that is associated with channel form (Wolman, Leopold 1957). Even in this regular size flood, less than 50% of the reaches had D50 pebbles transported. This suggests that this stream is not capable of transporting significant amount of the bed sediment and thus has limited ability to shape the channel during high frequency floods. Even in a very large, 100-year flood, 20% of the D50 sized pebbles would remain in place. Sediment downstream takes larger floods to transport than the sediment found upstream suggesting that the smaller floods have been incrementally transporting larger sediment downstream where it sits until a larger flood comes.

The geomorphic history of the stream system is an important control on modern channel form and process. Blacktail Deer Creek is superimposed on glacial till, outwash, and kame deposits from the Pinedale glaciation (Pierce 1979). Following the retreat of this glacier approximately 12,000 years ago (Licciardi, Pierce 2008) there was an extensive period of sedimentation as a result of the over steepened, glaciated slopes that were prone to mass movements. An extensive terrace on both the east and west forks likely formed due to the increased rates of sedimentation. In the field, we identified an ash layer from the Glacier Peak volcanic eruption approximately 11,000 years ago in this terrace indicating aggradation in the early and middle Holocene. Subsequently and there was a decrease in the sediment load of Blacktail Deer creek which likely lead to a period of incision. Eventually, much of the sediment was eroded away leaving distinct terrace and the channels of Blacktail Deer creek. As the stream incises into the Holocene fill its limit for incision is controlled by the local base level of the underlying glacial till. This is all supported by the trend in increasing D50 values moving downstream which leads to increased shear stresses which are more difficult to overcome in flooding events. These over steepened slopes referred to earlier were located upstream in the Washburn Range and was eroded more quickly further from the source.

The analysis of air photos from 1954, 1969, and 2018 indicate that the channel is relatively stable except where there were seven channel avulsions sometime between 1969 and 2018 (Figure 4). As shear stresses

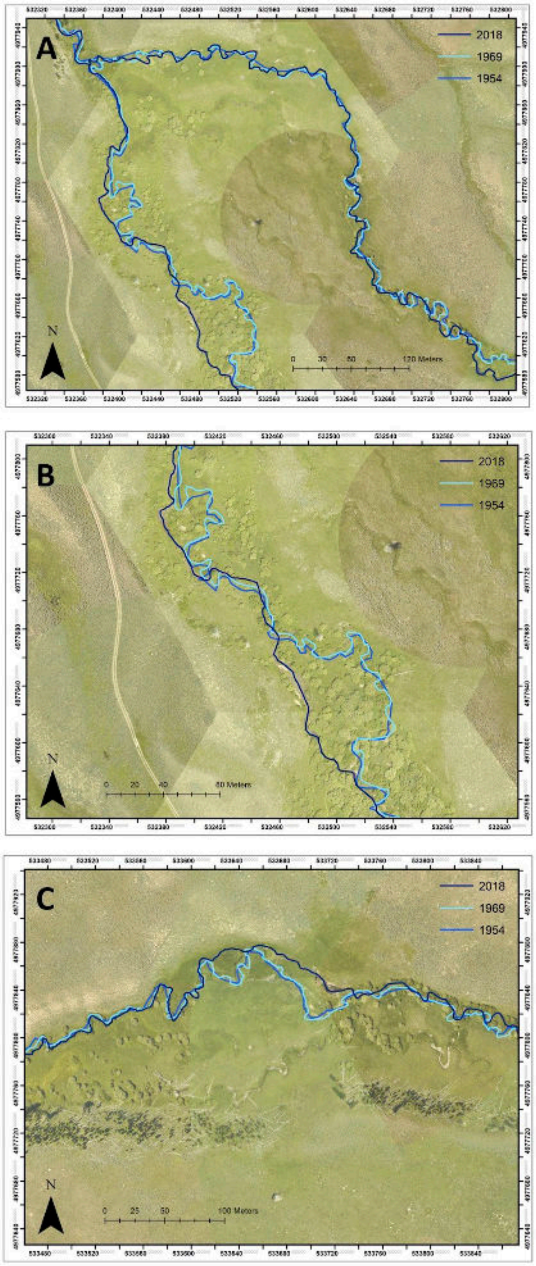

Figure 3. A) Confluence and upstream, shows a relatively stable and consistent channel shape from 1954 to 2018. B) zoomed in view of an avulsion since 1969 on WBT. C) zoomed in view of a slight avulsion since 1969 on EBT, also shows paleo channels that seem to have been abandoned since at least 1954.

Figure 4. Photographs of the west and east forks of Blacktail Deer creek from the 2019 field season. Circled in red are the examples of large diameter relict till and kame gravels. The sediment is in the channel and is too large to be transported by modern flood discharge and instead has been in place since the formation of the creek and provides armor for the channel that limits net channel incision.

are relatively low during large floods, it is unlikely that these avulsions are a product of incision of the channel bed but more likely the product of channel filling and cutting into fine-grained floodplain deposits. Blacktail Deer Creek has experienced a period of aggrading since during the early and middle Holocene. During this time, Blacktail Deer Creek aggraded mostly with smaller diameter sediment that mantles coarse remnant glacial outwash and till. The historical aerial images show the stream to be generally contained within its channel and does not seem to be incising new meanders.

By our detailed documentation of the sediment character in Blacktail Deer Creek, we are able to have a better understanding of the fluvial dynamics of the stream. From extensive pebble counts, we have a thorough characterization of the bed material and we have determined that the shear stresses associated with flooding events are not sufficient to mobilize the channel bed and trigger relatively quick incision in the second half of the 20th century. Due to the large diameter sediment present in both forks, this stream has been relatively stable in the historical period. While the willows have been affected by the over grazing of large ungulates in the Northern Range it is unlikely that abundance of riparian vegetation has played a significant rule in the evolution of this stream given that it is heavily controlled by large diameter relict till. The geomorphic controls are a significant control on the morphology and channel history of Blacktail Deer Creek.

ACKNOWLEDGMENTS

This material is based upon work supported by the Keck Geology Consortium and the National Science Foundation under Grant No. 1659322.

REFERENCES

Beschta, R. L., & Ripple, W. J. (2011) Trophic cascades in Yellowstone: The first 15 years after wolf reintroduction. Oregon State University, Corvallis, Oregon

Bierman, P. R., Montgomery, D. R., University of Vermont., & University of Washington. (2014). Key Concepts in Geomorphology.

Chadde, S. W. and C. E. Kay (1991). Tall-willow communities on Yellowstone's Northern Range: A test of the "natural-regulation" paradigm. The Greater Yellowstone Ecosystem. R. B.

Fritz, William J., Thomas, Robert C., 2011. Roadside Geology of Yellowstone Country. Mountain Press Publishing Company, Missoula, Montana.

Haines, A. L. (1977). The Yellowstone Story. USA, Yellowstone library and Museum Association.

Houston, Douglas B., Meagher, Mary. 1998. Yellowstone and The Biology of Time. University of Oklahoma Press, Norman, Oklahoma.

Knighton, D. (1998). Fluvial Forms and Processes A New Perspective. New York, Oxford University Press.

Komar, Paul D. 1988. Sediment Transport by Floods. Oregon State University, Corvallis, Oregon.

Licciardi, J. M. and K. L. Pierce (2008). "Cosmogenic exposure-age chronologies of Pinedale and Bull Lake glaciations in greater Yellowstone and the Teton Range, USA." Quaternary Science Reviews 27(7-8): 814-831.

Meyer, G. A. (2001). "Recent large-magnitude floods and their impact on valley-floor environments of northeastern Yellowstone." Geomorphology 40(3-4): 271-290.

Pierce, K. L. (1979). History and dynamics of glaciation in the northern Yellowstone National Park area. Professional Paper.

Sutherland JP. (1974). Multiple stable points in natural communities. The American Naturalist 108: 859-873.

Yellowstone National Park (1997). Yellowstone's Northern Range: Complexity and Change in a Wildland Ecosystem. Mammoth Hot Springs, National Park Service.

Wolf, E. C., et al. (2007). "Hydrologic regime and herbivory stabilize an alternative state in Yellowstone National Park." Ecological Applications 17(6): 1572-1587.

Wolman, M. Gordon, Leopold, Luna B. (1957) "River Flood Plains: Some observations on their Formation" Physiographic and Hydraulic Studies of Rivers, Geologic Survey Professional Paper